Physics Design and Prototype Development of Drift Tube Linac Cavity for High Current Applications

By

Shweta Roy

PHYS 01200804005

Bhabha Atomic Research Centre, Mumbai

A thesis submitted to the

Board of Studies in

Physical Sciences

In partial fulfillment of requirements

for the Degree of

DOCTOR OF PHILOSOPHY

of

HOMI BHABHA NATIONAL INSTITUTE

January, 2015

STATEMENT BY AUTHOR

This dissertation has been submitted in partial fulfillment of requirements for an advanced degree at Homi Bhabha National Institute (HBNI) and is deposited in the Library to be made available to borrowers under rules of the HBNI.

Brief quotations from this dissertation are allowable without special permission, provided that accurate acknowledgement of source is made. Requests for permission for extended quotation from or reproduction of this manuscript in whole or in part may be granted by the Competent Authority of HBNI when in his or her judgment the proposed use of the material is in the interests of scholarship. In all other instances, however, permission must be obtained from the author.

Shweta Roy

DECLARATION

I, hereby declare that the investigation presented in the thesis has been carried out by me. The work is original and has not been submitted earlier as a whole or in part for a degree / diploma at this or any other Institution / University.

Shweta Roy

List of Publications

Journal

1. Electromagnetic and Beam Dynamics studies of a high current linac for LEHIPA, **S. Roy**, S.V.L.S. Rao, R. Pande, S. Krishnagopal and P.Singh, Journal of Instrumentation **9**, 06007 (2014).
2. Physics design of a CW high-power proton LINAC for ADS, Rajni Pande, **Shweta Roy**, S.V.L.S Rao, P. Singh and S. Kailas, Pramana-J Phys., **78**, 247 (2012).
3. Design, development, and acceleration trials of radio-frequency quadrupole, S. V. L. S. Rao, Piyush Jain, Rajni Pande, **Shweta Roy**, Jose V. Mathew, Rajesh Kumar, Manjiri Pande, S. Krishnagopal, S. K. Gupta, and P. Singh, Review of Scientific Instruments **85**, 043304 (2014).

Conferences

4. Frequency analysis and field-stabilization for the LEHIPA DTL prototype, **Shweta Roy**, S.C.L. Srivastava, Rajni Pande, V.L.S. Rao Sista, S. Krishnagopal and P. Singh, Ind. Particle Accelerator Conf. (InPAC-2009), 10-14 February, 2009, RRCAT, Indore.
5. RF Characterization of DTL Prototype, **Shweta Roy**, S V L S Rao, Rajni Pande, Piyush Jain, Sumit Garg, Gireesh Singh, S. Krishnagopal and P. Singh, Ind. Particle Accelerator Conf. (InPAC-2011), 15-18 February, 2011, IUAC, New Delhi.
6. Design Studies of a 650 MeV Proton Linac for MPRR, Rajni Pande, **Shweta Roy**, V.L.S Rao Sista, P. Singh, P.K. Nema and R.K. Choudhury, Ind. Particle Accelerator Conf. (InPAC-2009), 10-14 February, 2009, RRCAT, Indore.

7. Fabrication of a Physics prototype DTL and Laser welding trials for Copper Drift tubes, Piyush Jain, **Shweta Roy**, S. Krishnagopal, N.K. Prasad, P.K. Nema, P.Singh, Ind. Particle Accelerator Conf. (InPAC-2011), 15-18 February, 2011, IUAC, New Delhi.
8. High intensity accelerator development for ADS, P. Singh, Rajni Pande, **Shweta Roy** and S.V.L.S Rao, Indian Nuclear Society News, Vol. 6, No. 2 April-June 2009, p 21-29.
9. Design and Development of LEBT for LEHIPA Project, Rajni Pande, **Shweta Roy**, S.V.L.S. Rao, Manas Ranjan Mishra & P Singh, Ind. Particle Accelerator Conf. (InPAC-2011), 15-18 February, 2011, IUAC, New Delhi.
10. Dipole stabilizer rods for 400 keV deuteron RFQ, V.L.S Rao Sista, S.C.L. Srivastava, Rajni Pande, **Shweta Roy**, P. Singh, Ind. Particle Accelerator Conf. (InPAC-2009), 10-14 February, 2009, RRCAT, Indore.
11. Developmental Studies of High Current Proton Linac for ADS Program, P. Singh, S.V.L.S. Rao, Rajni Pande, **Shweta Roy**, Rajesh Kumar, Piyush Jain, P.K. Nema, S. Krishnagopal, R. K. Choudhury, S. Kailas, V.C. Sahni, International Topical Meeting on Nuclear Research Applications and Utilization of Accelerators, May 4-8, '09, Vienna, Austria.
12. Electromagnetic design and mechanical development of permanent magnet focusing quadrupoles for drift tube linac, S. Malhotra, U. Mahapatra, **Shweta Roy**, P.Singh, R.K. Choudhury, Ind. Particle Accelerator Conf. (InPAC-2009), 10-14 February, 2009, RRCAT, Indore.
13. Low energy proton linac development at BARC for ADS program, S.V.L.S.Rao, Rajni Pande, **Shweta Roy**, Piyush Jain, Rajesh Kumar, S. Krishnagopal, P. Singh, P.K. Nema,

R.K. Choudhury, S. Kailas & V.C. Sahni, International Conference on Peaceful Uses of Atomic Energy-2009, Sept 29-Oct 1, 2009, New Delhi, Page 498.

14. A LEBT for the 400 keV RFQ based neutron generator at BARC, Rajni Pande, S V LS Rao, **Shweta Roy**, Manas Mishra, L.D Tayade, P.R Parate, Sapna P, Shailaja Ware, S.K Singh, A Agarwal, S.K Gupta, P Singh, Ind. Particle Accelerator Conf. (InPAC-2011), 15-18 February, 2011, IUAC, New Delhi.
15. Beam Dynamics Studies of Radio Frequency Quadrupole Accelerator for Project X, S.V.L.S Rao, Nikolay Solyak, C.S. Mishra, Rajni Pande, **Shweta Roy**, P. Singh, Ind. Particle Accelerator Conf. (InPAC-2011), 15-18 February, 2011, IUAC, New Delhi.
16. Development & Characterisation of Prototype RFQ at BARC, S.V.L.S. Rao, Piyush Jain, Rajesh Kumar, Rajni Pande, **Shweta Roy**, Manas Ranjan Mishra, Gireesh Singh, L.D. Tayade, Praveen Parate, Sumit Garg, S. Krishnagopal, P. Singh, S. Kailas, P.K. Nema, Ind. Particle Accelerator Conf. (InPAC-2011), 15-18 February, 2011, IUAC, New Delhi.
17. Focussing Magnets for Drift Tube Linacs, Vikas Teotia, Sanjay Malhotra, Kumud Singh, U.Mahapatra, S.Bhattacharya, G.P.Srivastava, **Shweta Roy**, Piyush Jain, P. Singh and S. Kailas, Indian Particle Accelerator Conference (InPAC-2011), 15-18 February, 2011, IUAC, New Delhi.
18. Design of RF structures for a superconducting proton linac, Rajni Pande, **Shweta Roy**, S.V.L.S. Rao, S. Krishnagopal, P.Singh, Indian Particle Accelerator Conference (InPAC-2013), 19-22 November, 2013, VECC, Kolkata.
19. Design, Development and acceleration experiments of a four-vane RFQ at BARC, S.V.L.S. Rao, Piyush Jain, Jose V. Mathew, Rajni Pande, **Shweta Roy**, S. Shrotriya, N. Patel, Shiju, M.R. Mishra, Gireesh Singh, L. Tayade, Praveen P., B.M. Kukreti, Rajesh

Kumar, Manjiri Pande, S. Krishnagopal, S. K. Gupta, P.Singh,Indian Particle Accelerator Conference (InPAC-2013), 19-22 November, 2013, VECC, Kolkata.

20. Physics Design of 650 MeV Proton Linac and Transport Line for HFRR at Vizag, Rajni Pande, **Shweta Roy**, S.V.L.S Rao & P Singh, BARC/2010/015.

Shweta Roy

To my Dear Parents

for their unconditional love and overwhelming support

ACKNOWLEDGEMENTS

I wish to thank, first and foremost, my guide Dr. Pitamber Singh for his benevolent guidance and persistent help through the course of my thesis work. His invaluable advices have always motivated me and provided me with directions to progress in my work. I am deeply indebted to him for his support and encouragement.

I am grateful to the members of my doctoral committee, Dr. V.M. Datar, Dr. R.G. Pillay, Dr. K.C. Mittal and Dr. Alok Chakrabarti for critically evaluating the progress in my work from time to time and giving me useful suggestions that benefited me a lot. I am sincerely obliged to Dr. S. Krishnagopal for his illuminating advices and useful discussions that helped me to improve my work. I take this opportunity to express my gratitude to all the colleagues of IADD for always being forthcoming and co-operative.

It gives me pleasure in acknowledging the ever willing help and support of my friends and colleagues, Rajni Pande, S.V.L.S. Rao, Tushima Basak and S.C.L. Srivastava. Special thanks are due to Piyush Jain, Jose Matthew, Sumit Garg and Roshan Abhishek for their help and co-operation. I also thank Manas Mishra, Praveen Parate, Laksman Tayade, Gireesh Singh, Prashant Gorule, N. J Koli, H. K Sane and Dalvi for their technical assistance.

Words are never enough to acknowledge the support of a loving family, yet I take this opportunity to express my gratitude to them all. My mother for her love, immense patience, her firm faith in me; my father for being affectionate and supportive always, for teaching me the basics of Physics and Mathematics, and getting me interested in these subjects. I thank my loving sisters for always having tremendous confidence in me. I am grateful to my husband for being supportive. Finally, and with all my heart I thank the two little angels; my daughters, Sharanya and Eshanika who always brighten up my life with their boundless love and admiration and their inquisitive nature that helps me learn afresh each day.

CONTENTS

SYNOPSIS

The Accelerator Driven Systems (ADS) have evoked interest worldwide because of their application in incineration of minor actinides and long lived fission products and utilization of Thorium as nuclear fuel. The ADS systems require a high intensity (~30 mA) CW linac. One of the most challenging parts of this high current accelerator is the low energy end where space charge forces are greatest. In view of this, a low energy high intensity proton accelerator (LEHIPA) project was taken up at BARC. This will consist of an ECR ion source, a 3 MeV Radio Frequency Quadrupole (RFQ) and a 20 MeV Drift Tube Linac (DTL). The 20 MeV linac will be completely indigenously developed at BARC.

A DTL, proposed by Alvarez, is a pillbox cavity modified by installing hollow conducting drift tubes along the axis in order to achieve successive acceleration in the same cavity and hence achieving high energy beams. The RF electric field decays to zero inside the drift tubes, thus creating field free regions that shield the particles when the polarity of the axial electric field is opposite to the beam direction. The drift tubes divide the cavity into cells of length $\beta\lambda$. As the particle velocities increase, the cell lengths also increase. The fields in all cells have the same phase so the multi-cell structure can be said to operate in zero mode. The drift tubes are supported mechanically by stems attached to the outer walls and on the drift tubes and are everywhere in phase. The net charge on the drift tubes and the net current on the stems at any instant of time are both zero. However, the time varying magnetic fields at the surface of the stems induce eddy currents that produce power dissipation. The hollow drift tubes also serve as housing for quadrupoles

which are provided for transverse focusing of the beam. The DTLs are exclusively used for protons and heavy ions in the velocity range near $0.05 < \beta < 0.4$. The DTL is an open structure without cell end walls and is therefore one of the most efficient accelerating structure at low energies. Further the presence of quadrupoles inside the drift tubes provides strong focusing, hence permitting higher beam-current limits.

This thesis is based on the results of the design of the DTL and measurements on a DTL prototype. The thesis comprises of six chapters. Chapter 1 gives an introduction on the DTL. Basic theory and working principle of a DTL has been outlined in this chapter. A review of other high intensity DTLs over the world has also been discussed.

Chapter 2 brings out the details of the electromagnetic design of the DTL. The accelerating mode field pattern has been described in this Chapter. The operating frequency of the DTL is 352.21 MHz. The DTL cavity has been designed with the following design criteria:

- To have good shunt impedance
- To have a constant tank diameter, bore radius and drift tube diameter along the structure for ease of fabrication.
- To have space for quadrupoles inside the drift tubes.
- To avoid voltage breakdown by keeping peak surface field below $0.9E_k$.

The structure parameters of the DTL have been optimised in order to achieve the above-mentioned design criteria. With these parameters, the gap between the drift tubes is optimised so that the structure resonates at the desired operating frequency of 352.21 MHz. The dissipated power distribution on the tank, drift tubes and stems has been calculated. The DTL will comprise of 4 tanks. Each tank will be provided with slug

tuners for tuning the frequency of the cavity. These tuners are pushed inside the cavity walls. They intercept the magnetic volume, and cause increase in the resonant frequency. In order to have both positive as well as negative frequency tuning, the DTL is designed with tuners half-way inserted inside the cavity. The maximum tuning range of the tuners has been calculated from the simulations. Based on the simulations, the dimensions of the tuner and the number of tuners per tank have been worked out.

The operating pressure for the DTL will be in the range of 10^{-7} Torr. In order to achieve this vacuum, pumping ports are provided on the tank walls. The apertures of the vacuum pumping ports are slotted in order to attenuate the RF power leaking out of the port and also to reduce the surface currents at the port corners, thus reducing the heat dissipation at these locations. Two vacuum ports will be provided in each tank. The vacuum ports are openings on the wall which cause an increase in the effective magnetic volume. Similarly RF ports, provided for feeding RF power to the cavity, cause an increase in the magnetic volume of the cavity. The frequency shift due to vacuum and RF ports have been estimated from the simulations.

The DTL operates in zero mode where the electric field distribution is very sensitive to small frequency perturbations. This is because the slope of the dispersion curve for this mode is zero, resulting in a zero group velocity. In order to make the operating mode more stable, postcouplers are inserted in the horizontal plane at the drift tube centers. The postcoupler gives rise to a TE mode band. Maximum stabilization is achieved when the highest frequency of the TE mode becomes equal to the TM_{010} mode frequency. At this point of confluence the dispersion curve has a non-zero slope, and hence a non-zero group velocity. The postcoupler stem represents an inductance while

the gap between the post and the drift tube creates a capacitance. Both elements form a resonant circuit whose frequency depends on the length and radius of the postcoupler. The capacitance also provides a coupling between the postcoupler mode and the acceleration mode. Thus, by changing the length and radius of the postcoupler, the TM_{010} mode frequency also changes. By changing the length of the post couplers the point where modes merge (confluence) is obtained and by means of 3D field simulations the conditions for field stabilization has been studied. The field stabilization with optimal postcoupler dimensions is then studied using the tilt sensitivity technique.

The beam dynamics studies of the DTL have been discussed in Chapter 3 of the thesis. The beam dynamics design is mainly focused on meeting the technical performance requirements of linac such as output current, final beam energy, emittance, and avoiding known beam instabilities and resonances. Some important design considerations are:

- Minimize the emittance growth.
- The zero current phase advance is kept below 90º, so as to avoid space charge induced beam instabilities.
- An aperture to rms beam size ratio of 8 is maintained in the DTL in order to avoid beam losses. This is very important for a high current DTL where space charge forces are significant.

Detailed beam dynamics simulation studies were performed to evolve an optimized DTL design. Quadrupoles are used for transverse focusing of the beam in the DTL. FD, FFDD and FFODDO lattices were studied for focussing. While the FD lattice provides smaller beam sizes, the quadrupole gradient required is 83 T/m. With the space

for quadrupoles limited by the drift tube geometry, such high gradients are difficult to achieve. In FFDD, while the beam size is higher than FD, the quadrupole gradients required are almost half of the FD lattice. The FFODDO lattice has the advantage that it offers space for diagnostics and beam steering elements in every third drift tube. However, the beam size and emittance growth in this lattice is the highest. Therefore, as a best compromise on all factors, the FFDD lattice has been chosen for LEHIPA DTL.

Permanent magnet quadrupoles (PMQs) will be used for the transverse focusing of the beam. The Electromagnetic quadrupoles (EMQs) can provide adjustable focusing, but require larger space inside the drift tubes. The diameter of the drift tube is limited by the requirement for high effective shunt impedance. Further, beam dynamics constrains the initial drift tubes to very small lengths (~ 5 cm). Housing EMQs in such a limited space would be very difficult. Therefore, we decide to use PMQs for focusing. Beam dynamics details have been worked out with FFDD lattice.

The effect of space charge on the beam dynamics has also been studied and reported in Chapter 3. In high current linacs for non-relativistic beams at low velocities, the Coulomb interactions are very important. To describe the space-charge field, we need to understand the properties of an evolving particle distribution, which requires a self-consistent solution for the particles and the associated fields. The significance of the space-charge fields is not only that they reduce the effective focusing strength, but also the nonlinear terms, a consequence of the deviations from charge-density uniformity, cause growth of the rms emittances, which degrades the intrinsic beam quality. In order to estimate the effect of space charge on the beam dynamics of 30 mA proton beam through the DTL, simulations were carried out (a) without space charge, (b) with linear

space charge (uniform beam at the DTL input) and (c) with Non-linear space charge (Gaussian distribution at the DTL input). For a beam without space charge, no emittance growth was observed in simulations. Even with linear space charge forces, the emittance growth was not very significant. In the case of non-linear space charge, emittance growth is observed. In the presence of beam mismatch errors or linac fabrication errors, this may lead to more serious emittance growth and beam losses.

In the design of DTL, it is very important to study the effect of errors on the various input parameters. The errors cause degradation of beam dynamics, and lead to reduced transmission and emittance blow-up. These studies are necessary to put limits on design tolerances that are needed in the fabrication of the DTL. A detailed error analysis was therefore done to study the effect of beam misalignment and tilt, quadrupole misalignment and gradient errors and errors due to variation in RF field amplitude and phase. For our study, the acceptance criteria was 100% transmission through the DTL and less than 5% increase in the normalized rms emittance for individual errors. Further, the effect of combined errors was also studied. Based on the error studies, the tolerances on various parameters were determined. These studies also form a part of Chapter 3.

The existence of beam halo is an important characteristic of a high intensity linac, and requires a careful study at the simulation stage. Halo is a small fraction of particles surrounding the dense beam core. Halo, like rms emittance, is an intrinsic property of the beam. Allen and Wangler defined the phase space halo parameter for the 2D phase space distribution for particle motion uncoupled in both planes in terms of second and fourth moments of the particle distributions. The halo parameter contains additional information as to the beam state, a figure of merit in high intensity accelerators. As with emittance,

the halo parameter is invariant under linear forces. Thus, halo growth is necessarily the result of nonlinearities. Another halo definition suggested by P. A. P. Nghiem, et. al. is based on the visual observation of the beam where the core part and the halo part can be clearly identified and only a clear border between the two remains to be determined. This definition is model independent and is capable to treat any definition type. This definition divides the beam into core and halo and then defines two terms (1) percentage of halo size (PHS) and percentage of number of particles (PHP) in the halo. Both PHS and PHP together describes the halo and its evolution along the linac structure. The evolution of beam halo in the DTL has been studied for different input beam currents and the results are presented in Chapter 4. The longitudinal halo form first as the longitudinal tune depression is more severe than the transverse one. These halos are generated even with perfectly matched beams. Beam halo studies have been done for different beam currents and with different degrees of input beam mismatch. It is found that up to a current of 10 mA there is no significant halo formation even with a 30% mismatch in the input beam parameters. At higher currents, beam halos are excited even with a perfectly matched beam, while with beam mismatch the beam halos tend to exacerbate. These studies show that the beam ellipse mismatch has to be carefully controlled in order to avoid the excitation of beam halo and that good matching can indeed substantially control formation and growth of beam halos. Within the DTL, even with these halos, there is no beam loss as the DTL has been designed with large enough apertures (8 times rms beam size in the perfectly matched case).

To validate the electromagnetic simulations a 1.2 m long prototype of the DTL containing the first 16 cells of the first DTL tank was fabricated and RF measurements

were done. The DTL prototype has one vacuum port and two RF ports. The prototype consists of an MS tank electroplated with copper, 17 drift tubes made of aluminium, and 3 tuners also of aluminium.

RF measurements were done on the DTL prototype using the Vector Network Analyzer (VNA). These measurements are discussed in Chapter 5 of the thesis. The measured frequency in air with all tuners flush with tank surface was 348 MHz. The resonant frequency with all the 3 tuners inserted at 10.5 cm was found to be 350.75 MHz. In order to understand the difference between the designed frequency and measured frequency in the DTL prototype more simulations were done to study the effect of various DTL dimensions which could have been different in the fabricated DTL prototype. Simulations were also done to take into account the change in frequency due to the medium being air instead of vacuum which was assumed in the original simulations. The frequency with half-way inserted tuners corrected for the actual dimensions and with air as the medium is calculated to be 349.45 MHz. The measured frequency with this tuner position is 349.49 MHz. In order to measure the electric field on the axis, bead pull measurements were done on the DTL prototype. A dielectric bead was passed along the axis of the DTL and phase measurements were done using a VNA. The field in each gap was then calculated using the Slater Perturbation theorem. The field flatness was studied by changing the depth of the tuners. The tuner positions were adjusted to obtain a flat field in all the gaps. A field flatness of within ± 2 % was achieved by the help of the tuners. The fabricated prototype closely met the physics specification and based on these measurements the fabrication of drift tube linac has been initiated.

Chapter 6 gives a brief summary of the thesis work. It also points out scope of future developments and studies in the design of high current DTLs.

List of Figures

List of Tables

CHAPTER 1

Introduction

The development of charged particle accelerators and its underlying principles builds on the theoretical and experimental progress in fundamental physical phenomena. Research leading to the discovery of elementary particles also led to the ideas for accelerating charged particles. The advent of particle accelerators opened the door to several new researches and today the particle accelerators find application in many basic researches pertaining to high energy physics, cosmology, nuclear physics condensed matter physics, etc. The particle accelerators are also widely used for medical and industrial applications.

Particle accelerators came in many forms applying a variety of technical principles [1]. All are based on interaction of electric charge with static and dynamic electromagnetic fields and it is the technical realisation of this interaction that leads to different types of particle accelerators. Electromagnetic fields are used over most of the available frequency range from static electric fields to ac magnetic fields in betatrons oscillating at 50 to 60 Hz, to radio frequency fields in the MHz to GHz range and to laser beams for generating high field for particle acceleration.

The development of charged-particle accelerators has progressed along double paths [2] which by the appearance of trajectories are distinguished as linear accelerators and circular accelerators. Particle travel in linear accelerator only once through the accelerator structure while in circular accelerator they follow a closed orbit periodically for many

revolutions accumulating energy at every traversal of the accelerating gap. The choice of one or the other class of accelerator depends mostly on the specific application and sometimes the available technology. For applications demanding high-energy, high intensity and high duty factor beams of high quality, the choice is generally the linear accelerator. Some attractive characteristic of linear accelerators are (1) Strong focusing can easily be provided to confine a high intensity beam. (2) The beam traverses the structrure in a single pass, thus avoiding repetitive error conditions causing destructive beam resonances. (3) Injection and extraction are simpler than in circular accelerators (4) A linac can operate at any duty factor, all the way to a continuous wave which results in acceleration of beams with high average current.

Electrostatic accelerators [3-5] are limited to low energies due to voltage breakdown which imposes a technical limit on the maximum achievable voltage and hence the maximum achievable acceleration. The solution to this limitation is to have time varying voltages, typically at rf frequencies. Very high accelerating voltages can be achieved in resonant rf cavities far exceeding those obtainable in electrostatic accelerator of similar dimensions.

In an rf linac, either an electromagnetic travelling wave is launched or a standing wave is produced in a long cavity consisting of several electromagnetically coupled cells. The travelling wave linacs are generally used for the acceleration of electrons while the standing wave linacs are used for protons and heavy ions. One type of standing wave structure very commonly used for the acceleration of protons and heavy ions in the low to medium energy range is the Alvarez drift tube linac [6].

1.1 Alvarez Drift Tube Linac (DTL)

The Drift Tube Linac (DTL), also called the Alvarez structure after its proposer, is basically a long cylindrical cavity excited in TM_{010} mode and loaded along its axis with cylindrical drift tubes as in Fig 1.1.

The Drift Tube Linac (DTL), proposed by Alvarez et al. [6,7] is a pillbox cavity modified for successive acceleration, by adding hollow conducting drift tubes along the axis. The RF electric field decays to zero inside the drift tube. This creates field-free regions that shield the particles when the polarity of the axial electric field is opposite to the beam direction. The drift tubes divide the cavity into cells of nominal length $\beta\lambda$ [8]. As the particle velocity increases, the cell lengths also increase. At any instant of time the field in all the cells have the same phase. Thus the multi-cell linac operates in zero mode.

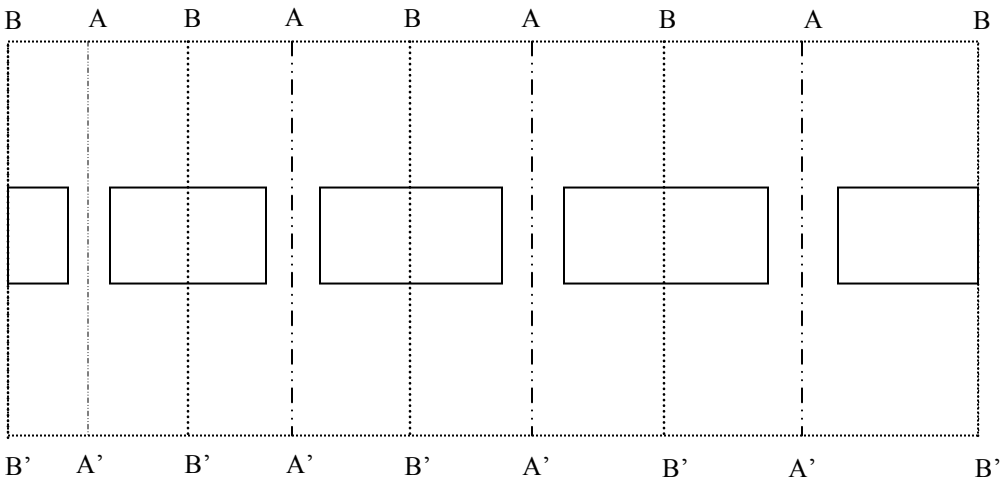

Fig.1.1.The Alvarez structure. Division into unit cells (planes AA').

It can be seen that the structure has approximate planes of symmetry at mid-gap (planes AA') and mid drift tube (planes BB'). Thus as with all periodic structures, the tank may be regarded as a system of collinear unit cells, each oscillating at the same

phase and frequency in the fundamental TM_{010} (perturbed) mode, the zero mode. The distance between gap centres, l_r is the distance travelled by a reference particle in n rf cycles (the n2π mode of acceleration), i.e, $l_r = n\beta_r\lambda$ (n is usually unity, but can be greater than unity for special reasons), and the length of the cell, that is the distance between successive mid drift tube planes is $Lr \approx ½\ n\ (\beta_{r-1} + \beta_r)\ \lambda$, where β_r is the output β of cell r, and λ is the free space wavelength. Lengths defined in this way ensure that a reference particle arrives at the gap centres at constant phase, since the gaps themselves are at the same phase. Since successive cells increase in length, other dimensions of the unit cell must vary to maintain resonance.

The drift tubes are supported mechanically by stems attached to the outer wall. The currents flow longitudinally on the outer walls and on the drift tubes and are in phase everywhere [9]. At any time, the net charge on the drift tube and the net current on the stems are both zero. However, eddy currents produced by time varying magnetic fields cause power dissipation at the surface of the stems.

Transverse focusing is provided by installing magnetic quadrupole lenses inside the drift tubes. At low velocities it becomes more difficult to provide focusing because the drift tubes are smaller and less space is available for installing quadrupole magnets.

The DTL is used exclusively for protons and heavier ions in the velocity region near $0.05 < \beta < 0.4$, where the space charge forces are considerable. The schematic of DTL is shown in Fig.1.2. The advantages of DTL are:

1. It is an open structure without cell end walls, generally resulting in high effective shunt impedance.

2. Focusing quadrupoles within the drift tubes provide strong focusing and permit high beam current limits.

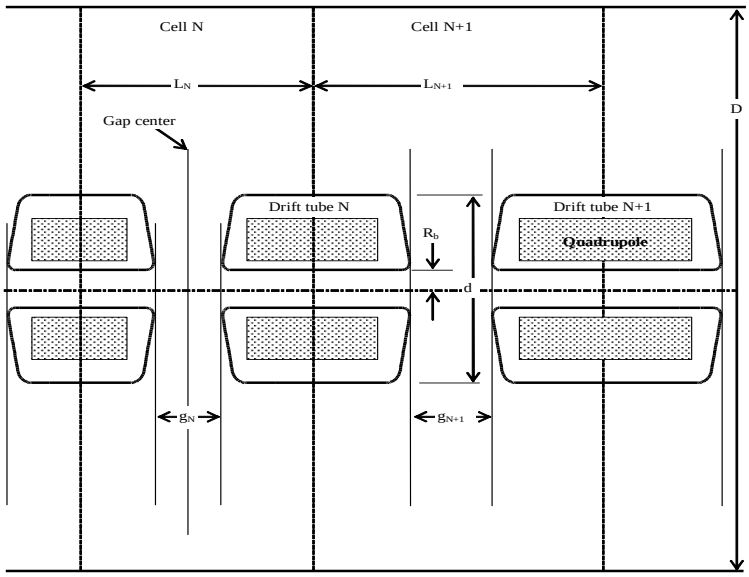

Fig. 1.2.Schematic of the drift tubes in the DTL.

1.2 Design of Drift Tube Linacs

For the purpose of design of a DTL, it is sufficient to study the characteristics of the unit cell, except for discussion of length and tolerances of the whole tank. The tank and drift tube diameters, the drift tube corner and nose radii, the ratio of gap to cell length and the total tank length must be chosen as a compromise between maximal shunt impedance, freedom from voltage breakdown, good beam dynamics, ability of the drift tubes to contain focusing devices, ease of manufacture, and tolerances. These criteria are all related, and therefore it is important to consider the correct order of importance, which depends to a large extent on the final application of the linac. The unit cell parameters are thus also related, but above all they must satisfy the condition of resonance.

As discussed earlier, in order to maintain phase synchronism, lengths of each cell increases as the particle velocity increases. The required cell length profile depends on the synchronous velocity β_s, which increases because of energy gain in each cell. The energy gain in a cell, in turn depends on the electric field and on the length of the cell. Since, the cell length and energy gain are interdependent, the cell design is usually done by a method of successive approximations. First, the cell geometry at each β_s is chosen, generally based on the criterion of high effective shunt impedance, providing space inside the drift tubes for quadrupoles and keeping the peak surface fields within technological limits, while maintaining the resonance condition. The fields, power, transit time factor and shunt impedance are calculated using an electromagnetic field solver code [10] such as SUPERFISH. Thus one obtains an optimised cell geometry in which gap length, drift tube shape and tank diameter are determined.

Because of the energy gain in the accelerating gap, the gap centre is always displaced towards the low energy end of the cell. The positions of the gaps need to be determined to study the beam dynamics through the DTL. This procedure requires calculations that allow for the change of β_s in the cell, which depends on the magnitude of the average accelerating field E_0 and on the synchronous phase φ_s. The choice of E_0 is important because it affects the accelerator length, the power dissipation, the probability of electric breakdown, and the longitudinal focusing. The choice of φ_s affects both the accelerator length and the longitudinal focusing. A numerical integration needs to be done to determine the positions of the electrical centre of the successive gaps and the successive cell lengths. A simple algorithm for integrating through the gaps that gets fairly accurate results is called the drift-kick-drift method. In this approximation, the

particle is assumed to drift at constant velocity β_{s1} from the centre of the drift tube to the center of the gap, where it receives full acceleration as an impulse at the gap center, after which it drifts at the new constant velocity β_{s2} to the center of the next drift tube. The drift distances are $x_1 = \beta_{s1}\lambda/2$ and $x_2 = \beta_{s2}\lambda/2$, and the total cell length is $L = x_1+x_2$. The energy gain at the center of the gap is then calculated knowing the value of E_0 and using this value of L. This calculation is done from cell to cell until the final energy is reached. Similar methods are used in DTL design code PARMILA to lay out the gap location and cell lengths. The DTL is usually configured as a sequence of independent multi-cell tanks, each with its own RF drive. The tank lengths are determined mainly by the power available from the RF generator, by mechanical constraints, and by ability to control the field distribution along the tank to a sufficient precision.

1.3. DTL for Low Energy High Intensity Proton Accelerator (LEHIPA)

The Accelerator Driven Systems (ADS) [11,12] have evoked interest worldwide because of their application in incineration of minor actinides and long lived fission products and utilization of Thorium as nuclear fuel. In ADS, a high-energy proton beam from an accelerator strikes a heavy element target which yields copious neutrons by (p, xn) spallation reaction. The ADS mainly consists of a high intensity proton accelerator, an spallation target, and a sub-critical reactor. The schematic of an ADS is shown in Fig. 1.3. An ADS requires a high power proton accelerators with typical energy of 1 GeV and beam current of 20-30 mA. The accelerator should operate in CW mode to avoid thermal shocks to the fuel elements, the accelerator should be robust and reliable with 100 %

availability. The beam loss in the accelerator should be limited to <1 nA/m. The conversion efficiency from mains to beam power should be > 40 %.

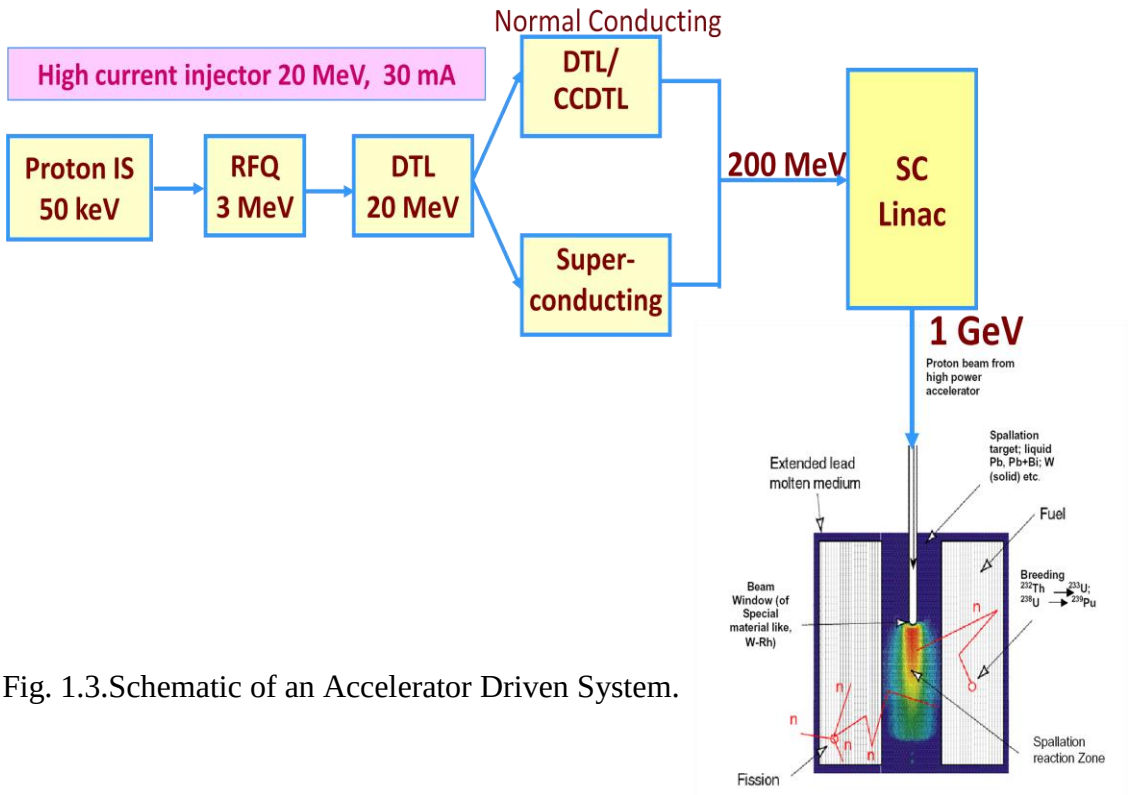

Fig. 1.3.Schematic of an Accelerator Driven System.

The ADS require a high intensity (~30 mA) CW linac [13]. One of the most challenging parts of this high current accelerator is the low energy end where space charge forces are greatest. The intense space charge forces at low energies, lead to increase in beam size and initiation of halo generation which manifests itself at higher energies, causing beam loss and radio-activation of the linac components. In view of this, a low energy high intensity proton accelerator (LEHIPA) [14] project was taken up at BARC. This will consist of an ECR ion source, a 3 MeV Radio Frequency Quadrupole (RFQ) [15, 16] and a 20 MeV Drift Tube Linac (DTL) [17]. The schematic of the 20

MeV linac is shown in Fig. 1.4. The DTL for LEHIPA will be used to accelerate proton beam from 3-20 MeV. The DTL will operate in CW mode with a beam current of 30 mA.

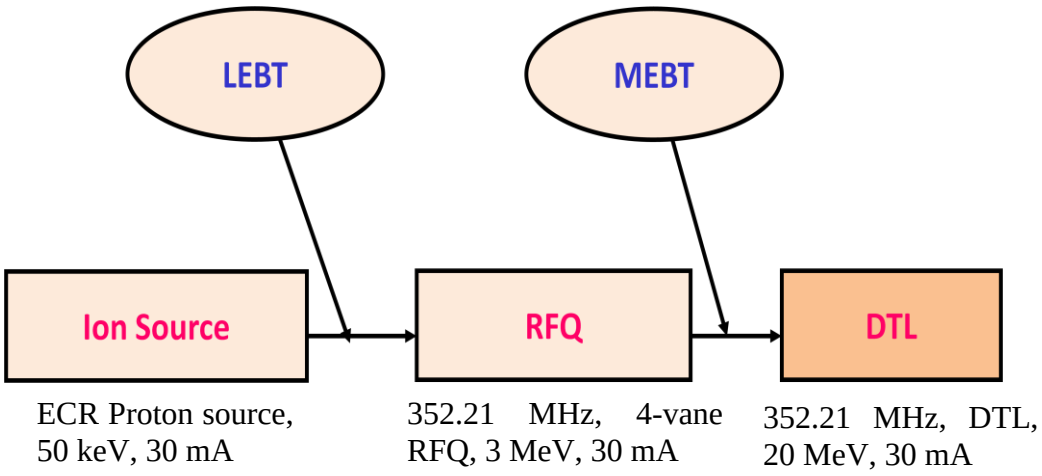

Fig. 1.4.Schematic of a Low Energy High Intensity Proton Accelerator.

1.4. DTLs over the world

The DTL is commonly used for accelerating ion beams in the low to medium energy range. There are various DTL projects around the world, but all of these are pulsed and mostly low duty cycle machines. The LANSCE DTL, operating at 201.25 MHz, accelerates H^+ and H^- beams from 0.75 MeV to 100 MeV. The beam current is 11 mA for H^- and 17 mA for H^+. The ramped gradient DTL of ATS accelerates H^- beam from 2.07 MeV to 6.67 MeV and is rated at 100 mA beam current with a duty factor of 5 %. The pulse width is 825 μs and repetition rate is 120 Hz. The SNS, at Oakridge uses an Alvarez DTL to accelerate H^- beam from 2.5 to 20 MeV [18] operating at 402.5 MHz with a peak current of ~50 mA. The JPARC linac [19] has a 50 MeV, 30 mA (peak) DTL and operating at 324 MHz. The maximum pulse width is 500 msec and

the maximum repetition rate of 25 Hz. The Linac 2 [20] at CERN consists of a 50 MeV, 202.56 MHz DTL and has a peak current of 150 mA. The Linac 4 [21] has a 160 MeV, 352.21 MHz DTL with a 40 mA average current and duty cycle of 10 %. The SPES at LNL, Italy [22] has a 352 MHz DTL project. The peak current is 50 mA and the energy is 43 MeV with possible future upgrade to 100 MeV. A 350 MHz, 100 MeV DTL is being built at Korea for the PEFP project [23]. The European Spallation Source (ESS) is a 5 MW, 2.5 MeV, pulsed proton machine with a design frequency of 352.2 MHz. The ESS uses the DTL [24] to accelerate proton beam from 3 MeV to 79 MeV. The pulse width is 2.86 ms at a repetition rate of 14 Hz and the peak current is 20 mA. The 324 MHz CSNS [25] at China is proposed to have a DTL with a peak current of 15 mA. The output beam of the DTL linac is 80 MeV in the first phase and 132 MeV for upgrade. The International Fusion Materials Irradiation Facility (IFMIF) [26] originally envisaged a DTL to accelerate CW D^+ beam from 5 MeV to 40 MeV. The beam current was 125 mA. However, the DTL was later replaced by a superconducting half wave resonator. The IPHI project at France [27], in its original version intended to use DTL to accelerate 100 mA CW proton beam from 5 MeV to 11 MeV. But, the project was later abandoned. In India, a 10 MeV, 352.2 MHz DTL is being fabricated at RRCAT, Indore [28] for the Indian SNS programme. The peak current is 30 mA and the duty factor is 1.25 %.

1.5. Outline of the Thesis

This thesis is based on the design and prototyping of a 20 MeV proton DTL for LEHIPA. The beam current is 30 mA and it will operate in CW mode. Chapter 2 brings out the details of the electromagnetic design of the DTL. The accelerating mode field pattern has been described in this Chapter. The operating frequency of the DTL is

352.21 MHz. Frequency analysis of the DTL has been done for tuners, vacuum and RF ports. The tuning range of the tuners has been calculated, based on which the number of tuners in a DTL tank has been determined. In order to make the operating field insensitive to perturbative frequency errors, postcouplers will be provided in the DTL. Frequency and field analysis with postcouplers has been studied and the results have been outlined in chapter 2.

The beam dynamics studies of the DTL have been discussed in Chapter 3 of the thesis. The beam dynamics design is mainly focused on meeting the technical performance requirements of linac such as output current, final beam energy, emittance, and avoiding known beam instabilities and resonances. The beam dynamics design criteria is to minimize the emittance growth, to keep the zero current phase advance below 90º, and to maintain an aperture to rms beam size ratio of 8 in order to avoid beam loss. Beam dynamics has been done with FD, FFDD and FFODDO lattices and a comparative study for the three lattices has been presented in this chapter. Effect of linear and non-linear space charge on beam dynamics has been studied and the results are given in this chapter. The effect of errors on the various input parameters has also been studied. These studies are necessary to put limits on design tolerances that are needed in the fabrication of the DTL. A detailed error analysis was therefore done to study the effect of beam misalignment and tilt, quadrupole misalignment and gradient errors and errors due to variation in RF field amplitude and phase. These studies also form a part of chapter 3.

Beam halos are an important characteristic of beams with high space charge. The halos lead to particle loss and activation at high energies, but the formation of halos is

initiated at low energies where the space charge forces are highest. The particle core model is used to describe the mechanism of halo formation. The mismatches for the excitation of quadrupole mode, fast mode and slow mode are calculated from this model. The beam evolution with these mismatches is studied and the results are discussed in Chapter 4. The growth of beam halos in the DTL has also been studied and the results are discussed in this chapter. Halo dynamics have been done for different degrees of space charge.

To validate the electromagnetic simulations a 1.2 m long prototype of the DTL containing the first 16 cells of the first DTL tank was fabricated and RF measurements were done. The DTL prototype has one vacuum port and two RF ports. The prototype consists of an MS tank electroplated with copper, 17 drift tubes made of aluminium, and 3 tuners also of aluminium. RF measurements were done on the DTL prototype. These measurements are discussed in Chapter 5 of the thesis. The field flatness was studied by changing the depth of the tuners. The tuner positions were adjusted to obtain a flat field in all the gaps. The fabricated prototype closely met the physics specification and based on these measurements the fabrication of drift tube linac has been initiated.

Chapter 6 gives a brief summary of the thesis work. It also points out scope of future developments and studies in the design of high current DTLs.

CHAPTER 2

Electromagnetic Design

2.1. Fields in a Drift Tube Linac

An Alvarez Drift Tube Linac is operated in the TM_{010} mode having electric field component in the axial direction, which is the direction of beam propagation. The magnetic field is in the azimuthal direction. Typical fields in a TM_{010} DTL cavity are shown by arrow plots in Fig 2.1.

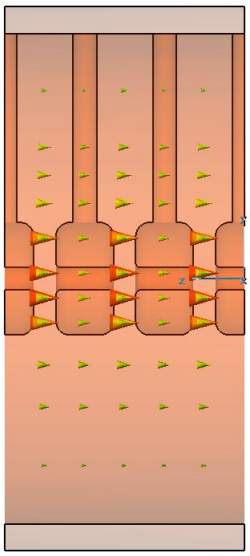

Fig 2.1 (a). Electric Field in a DTL.

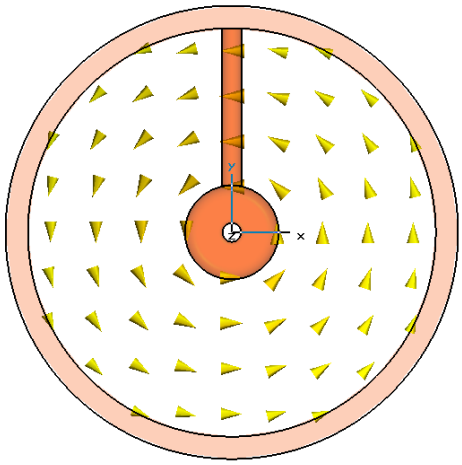

Fig 2.1 (b). Magnetic Field in a DTL.

The DTL is a modified pillbox cavity [29] with drift tubes provided for shielding of the fields when the polarity of axial field is opposite to beam direction. A pillbox cavity in TM_{010} mode has an axial electric field and an azimuthal magnetic field. The electric field is a zeroth order Bessel function in r and the magnetic field is a first order Bessel function in r. Thus, the electric field is maximum at the axis and falls as one

moves away from the axis and the magnetic field rises from zero at the axis and increases to a maximum value close to the wall, after which it decreases marginally as one approaches the cavity wall.

The drift tubes are metallic tubes, which when subjected to axial field of a pillbox cavity, push opposite charges on the two parallel faces, so as to create an equal and opposite field inside the metal. This field cancels out the axial field of the pillbox cavity, thus creating a field free region inside the drift tubes. There are small gaps between the drift tubes, which along with the faces of two adjacent drift tubes forms a capacitor. Due to the charging of the drift tube faces the electric fields get concentrated in the region between two drift tubes, and falls as one moves away from the drift tubes. The electric field in the radial direction is shown in Fig. 2.2. As the electric field changes polarity, the charges on the faces of the drift tubes also alter their polarity. Thus there is movement of electric charges from one face to the other in each half cycle of the applied RF field. This produces a surface current on the drift tubes, which flow through the stem support onto the tank surface. Each drift tube therefore acts as a surface current element, producing an azimuthal magnetic field, which falls as 1/r as one moves out from the drift tube walls towards the tank walls. This magnetic field superimposes on the pillbox magnetic field which is a first order Bessel function of r and increases as r increases. The net result is a field of the form shown in Fig 2.3. The variation of electric and magnetic field along the axial direction are shown in Figs. 2.4 and 2.5 in 3 cells of the DTL. The axial electric field is maximum at the centre of the gap and falls gradually down to zero at the drift tubes. There is some penetration of the electric field inside the drift tubes, due to the presence of bore for the transport of beam across the drift tubes.

Unlike the pillbox cavity, there exists no simple analytic expressions for the fields in a DTL and an electromagnetic field solver code is generally used to calculate the exact fields. Figs. 2.2 to 2.5 have been generated using CST Microwave Studio [30] for the LEHIPA DTL, for which the drift tube radius is 6 cm and the tank radius is 26 cm.

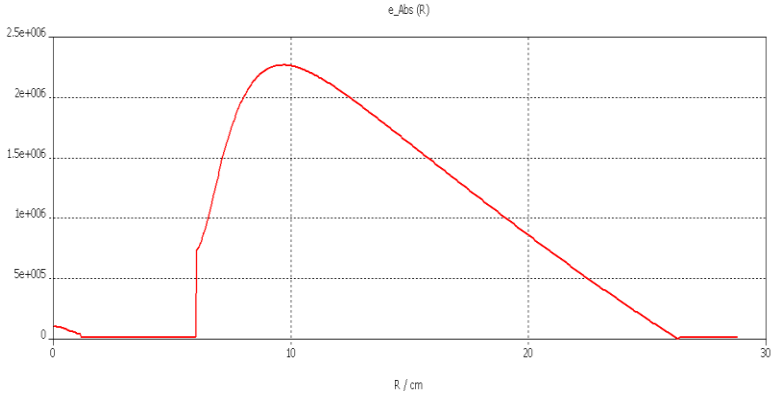

Fig. 2.2. Variation of electric field along the radial direction in a DTL.

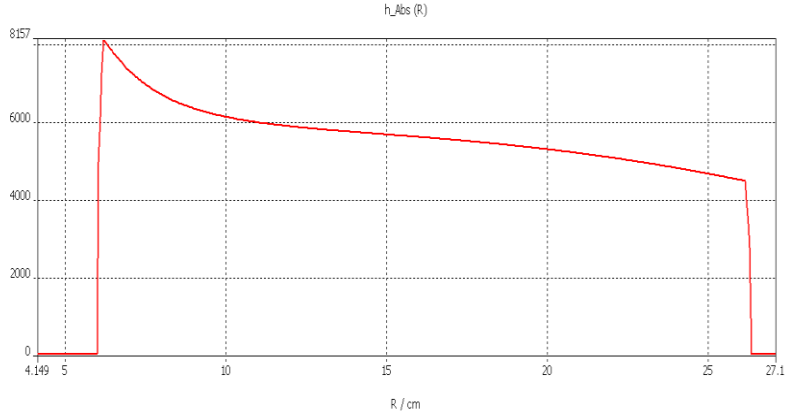

Fig. 2.3. Variation of Magnetic field along the radial direction in a DTL.

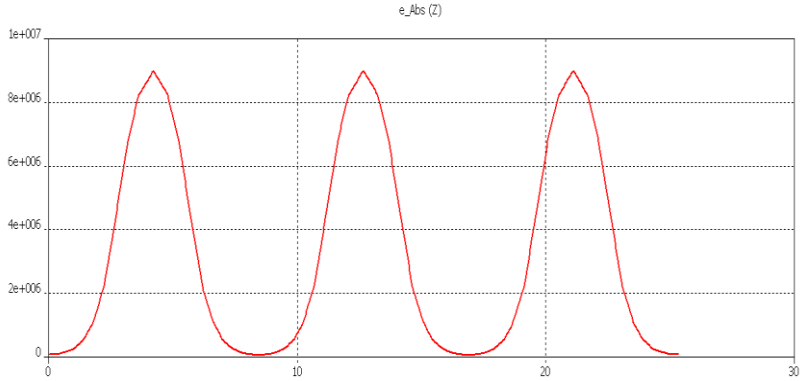

Fig. 2.4.Variation of electric field along the axial direction in a DTL.

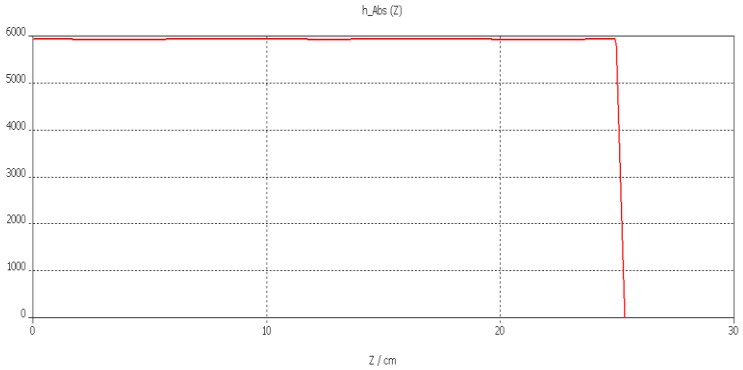

Fig. 2.5.Variation of Magnetic field along the axial direction in a DTL.

2.2. Cavity Design

2.2.1 2D Cavity Design

The program DTLFISH in the Poisson SUPERFISH [31] code distribution is used to design the cavity shape and compute fields, rf power losses, transit time factor and shunt impedance. DTLFISH sets up the geometry for drift-tube linac (DTL) cells. Fig.2.6(a) shows the basic outline of DTL cavity generated by DTLFISH and Fig. 2.6(b) shows the detailed geometry of the drift tube. The DTL cell is a figure of revolution about the beam axis. DTLFISH assumes a symmetric cell, and therefore sets up SUPERFISH runs for only half the cell. The symmetry plane is in the gap center between the two drift-tube noses. DTLFISH tunes the cell by adjusting the cavity diameter(D), drift-tube diameter(d), gap(g), or face angle(α_f).

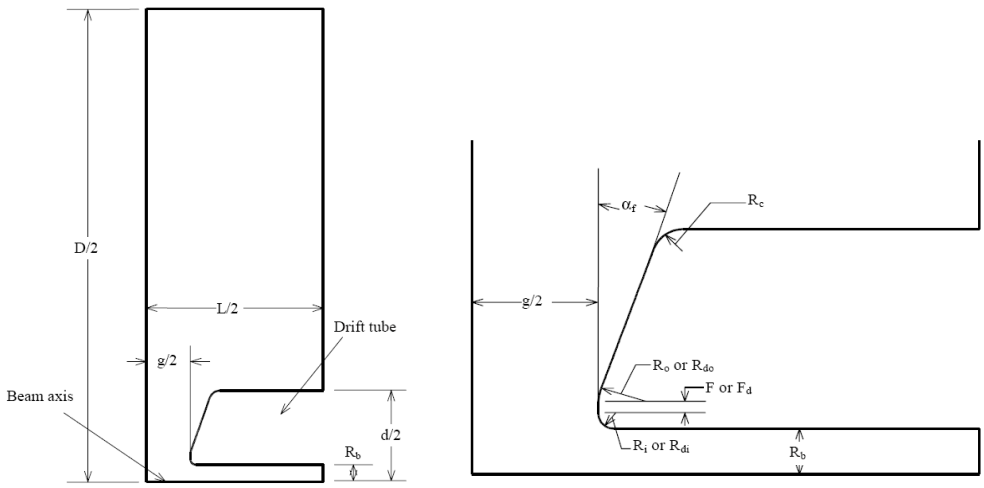

Fig.2.6.(a) The DTL half cell set up by the code DTLFISH. (b). Detail near the drift-tube nose.

The cell geometry at each velocity is chosen based on the following design criteria:

- To obtain the correct resonant frequency.
- To have maximum effective shunt impedance.
- To have space for quadrupoles inside the drift tubes.
- To avoid voltage breakdown by keeping peak surface field below $0.9E_k$. Higher limits ~1.2 E_k have been reported for pulsed DTLs over the world [32, 33], but since there is no experience on CW DTLs worldwide, a lower limit has been chosen.
- To have a constant tank diameter, bore radius and drift tube diameter along the structure for ease of fabrication.

The design procedure results in an optimum cell geometry in which the gap length, drift tube shape, and tank diameter are determined. Because of the energy gain in the accelerating gap, the gap is always displaced towards the low energy end of the cell. However, the field calculations relative to the gap are nearly independent of the precise

location of the gap within the cell. Therefore, the SUPERFISH calculation is done for an equivalent symmetric cell, which has the same length and geometry as the real cell but has the gap in the geometric center of the cell.

2.2.1.1 Tank Diameter

To design the DTL cavity first the cavity diameter was optimized. The idea was to use the same tank diameter for all the DTL tanks that is, in the entire energy range from 3-20 MeV for the ease of fabrication. The effect of varying tank diameter on the effective shunt impedance is shown in Fig. 2.7. It is found that the optimum diameter is 52 cm for the entire energy range.

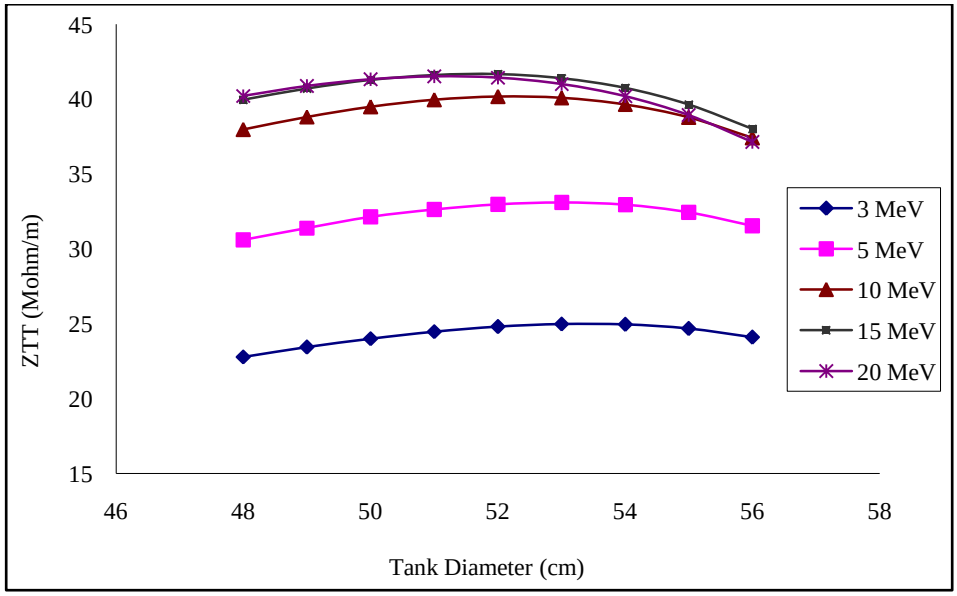

Fig. 2.7. Effective Shunt Impedance vs. Cavity Diameter.

2.2.1.2 Drift Tube Diameter

The drift tubes must be large enough to accommodate quadrupole magnets for focusing and to provide space for cooling of drift tubes which is essential in CW operation. As can be seen from Fig. 2.8, the effective shunt impedance decreases with

increase in the drift tube diameter. As a compromise between the two, the drift tube diameter was chosen to be 12 cm.

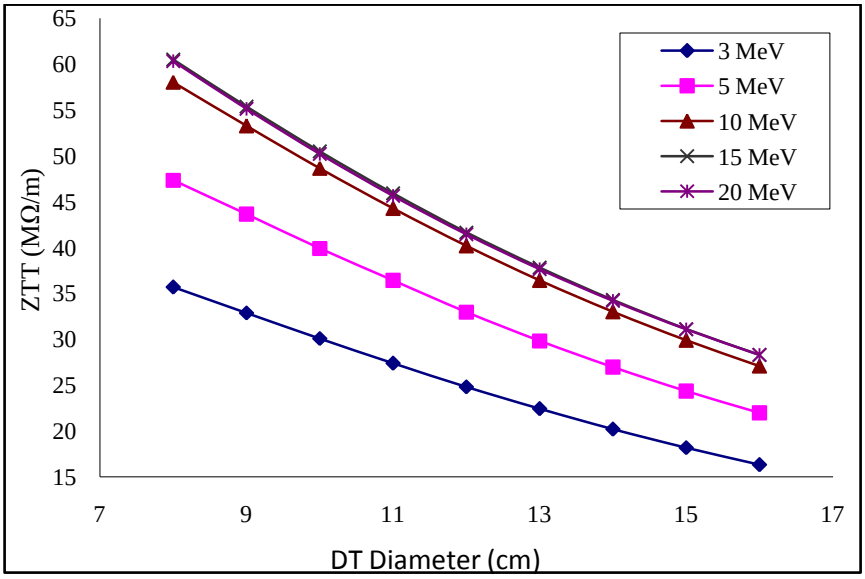

Fig.2.8. Variation of effective shunt impedance in the DTL with Drift tube diameter at different energies.

2.2.1.3 Bore Radius

Field penetration inside the axial bore holes of the drift tubes reduces the transit time factor, because it reduces the concentration of field near the centre of the gap. As a result, the effective shunt impedance decreases with increase in bore radius as can be seen from Fig. 2.9. Hence a smaller bore radius is preferred. But in order to ensure low beam losses the aperture must be much larger than the rms beam size. So the aperture radius is chosen to be 1.2 cm.

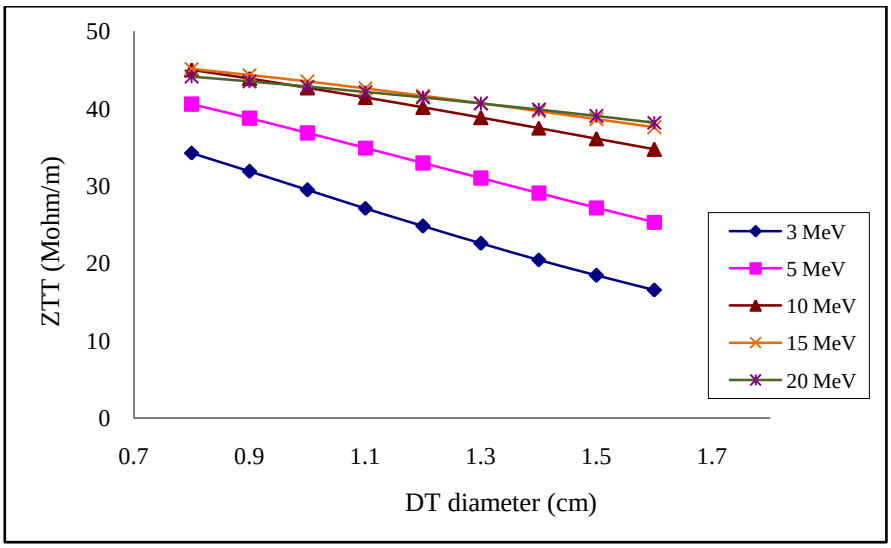

Fig.2.9. Variation of effective shunt impedance in the DTL with bore radius at different energies.

2.2.1.4 Corner and Nose Radii

Existence of sharp corners in high power linacs lead to field intensification and hence breakdown at these points. The corner and nose radii are provided to round off the sharp edges of the drift tube surfaces. Simulations show high power density at the corner edges of the drift tube radius. This is because the magnetic field is highest at these radial points. The drift tube bore edges are less dissipative because the magnetic field is very less at these points close to the axis. The drift tube power dissipation is plotted as a function of corner radius and nose radius in Fig. 2.10. Increasing the corner radius reduces the power dissipation, but larger radius will leave lesser flat portion on the drift tube surface for the welding of the stem onto the drift tube, especially in low energy drift tubes with shorter lengths. It is preferred to have a flat drift tube surface where the stem joins the drift tube. Since the stem radius is 2.5 cm, a requirement that arises from the

mechanical point of view, one needs a flat portion of 2.5 cm on the drift tubes before the rounding of the corners begin. The design aims to provide the same corner radius for all the drift tubes and hence it is kept to be 1.0 cm, which is the maximum possible value for the shortest drift tube. The power dissipation at the nose does not vary much by changing its radius and its value has been kept as 0.5 cm.

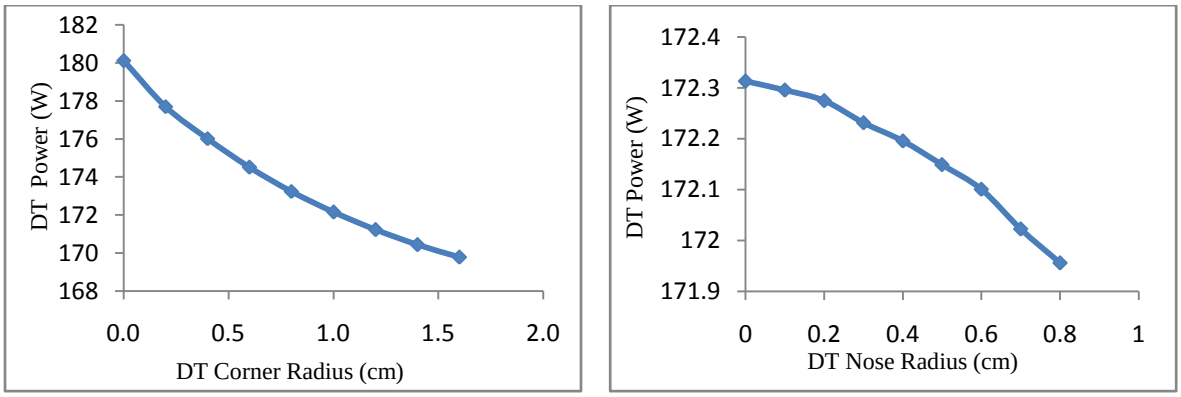

a b

Fig. 2.10. Drift Tube Power as a function of (a) corner radius (b) nose radius.

2.2.1.5 Face angle

Angles are provided on the drift tube faces to increase the concentration of axial electric field in the gap. This increases the transit time factor, and hence the effective shunt impedances. The variation of effective shunt impedance with face angle is shown in Fig. 2.11. However, increased face angle restricts the available space inside the drift tube for focusing magnets and cooling water. The face angle is chosen to be constant in a tank, and is limited by the space requirement for quadrupole magnet and cooling water channel in the first drift tube of that tank. The face angle is the smallest in the first tank where the drift tube lengths are smallest and is highest in the fourth tank which has larger drift tubes and hence more space for magnet and cooling water.

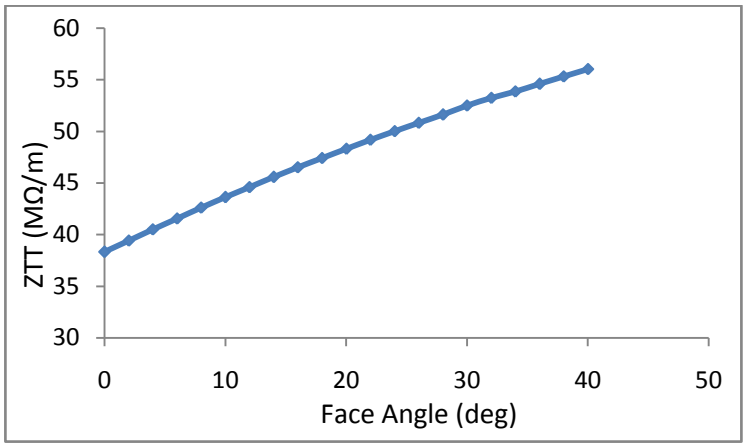

Fig. 2.11.Variation of Effective Shunt impedance with Face Angle.

The structure parameters of the DTL based on the design are listed in Table 2.1. The total length of the DTL is 11.92 m and it is planned to make it in four tanks. The total power dissipation is 988 kW. The effective shunt impedance along the DTL for the optimized cavity geometry is plotted in Fig. 2.12. The SUPERFISH model of the first cells of all the four tanks with face angles are shown in Fig. 2.13. The electric field lines are also shown in the Fig. 2.13.

Table 2.1. Cavity parameters of DTL.

PARAMETER	**VALUE**
Frequency (MHz)	352.21
Tank Diameter (cm)	52
Drift Tube Diameter (cm)	12
Bore Radius (cm)	1.2
Flat Length (cm)	0.4
Corner Radius (cm)	1.0
Inner Nose Radius (cm)	0.5
Outer Nose Radius (cm)	0.5

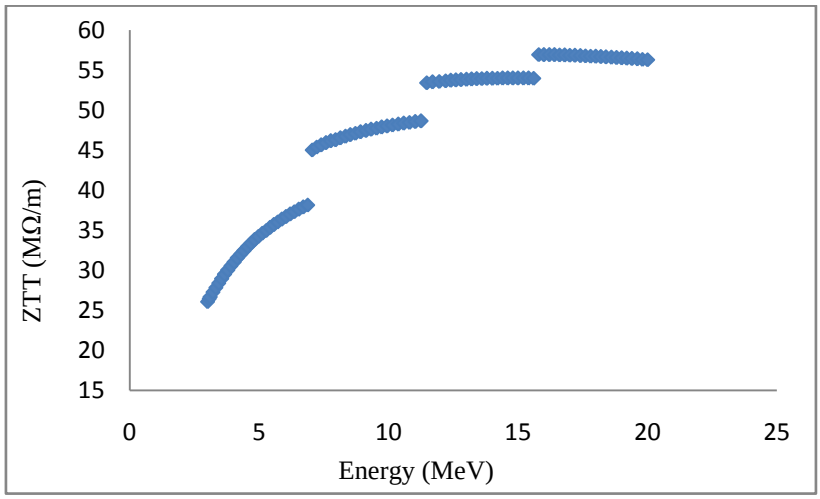

Fig. 2.12. Effective shunt impedance along the DTL.

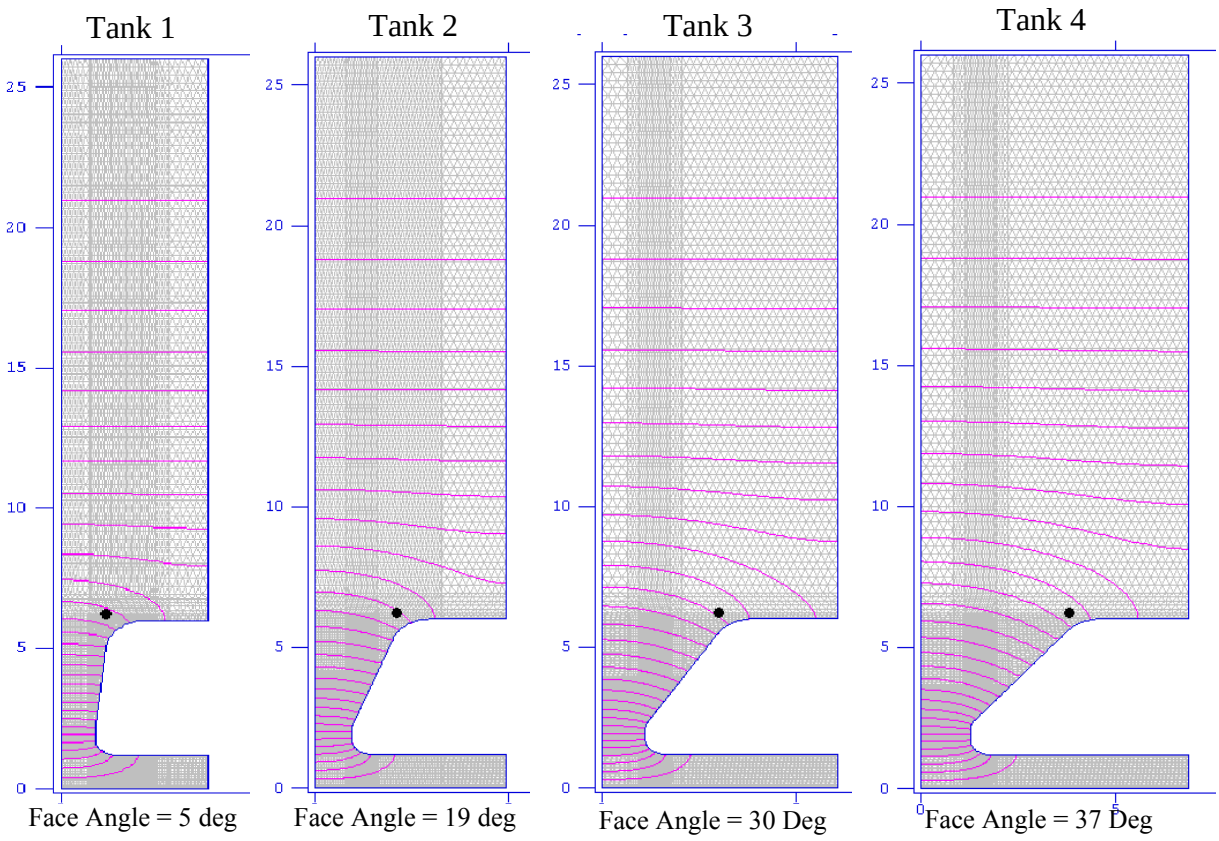

Fig. 2.13. First cell of each tank of the DTL showing electric field lines.

2.2.2 3-D Cavity Design

In order to include features that break the 2D symmetry (viz., stems, tuners, vacuum and RF ports and post couplers) a 3D design of the DTL tank was done using CST Microwave Studio [34]. The frequency shift due to various non-axisymmetric components has been studied and a correction in the tank diameter has been suggested in order to compensate for the frequency shifts. The first DTL tank consists of 35 cells and accelerates the beam from 3 MeV to 6.92 MeV. In order to simplify the simulation model, the geometry of the centre cell together with drift tube no. 18 was used. Three cells of this geometry have been modelled in CST Microwave Studio as shown in Fig. 2.14 and the frequency of the accelerating mode (TM_{010}) is 352.19 MHz.

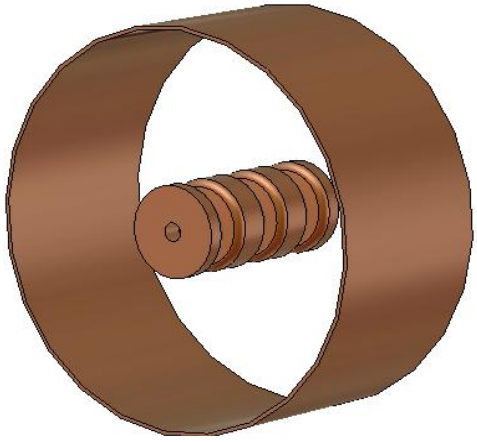

Fig. 2.14.A three-cell model of a DTL.

2.2.2.1 Stems

The drift tubes are supported mechanically by stems attached to the tank surface. The inclusion of stems to a DTL cavity causes a shift in resonant frequency. Each new device inserted into the cavity gives rise to a new frequency band containing number of modes

equal to the number of such insertions. Stems of diameter 2.5 cm were added to the CST MWS model of the three cell DTL. By including the stems the resonant frequency of TM_{010} mode shifted to 353.48 MHz. The resonant frequency shift can be corrected by increasing the tank diameter. The correction in tank diameter required to resonate the DTL at 352.21 MHz has been calculated to be 52.29 cm. Stem modes were observed at frequencies below 200 MHz. These modes are characterized by magnetic field lines that go round the stems and electric field between the stems as shown in Fig. 2.15.

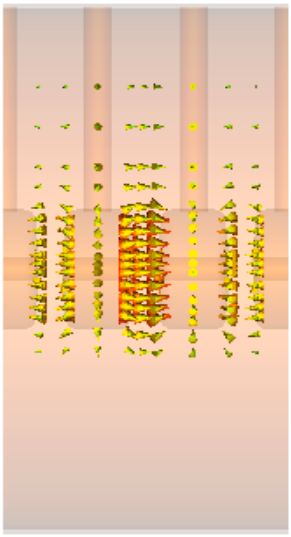

Fig. 2.15 a. Electric Field for the Stem mode.

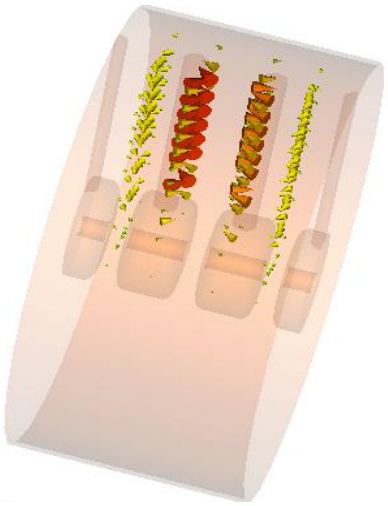

Fig. 2.15 b. Magnetic Field for the Stem mode.

A seven cell model with varying cell lengths was also used for the simulations. The frequency of DTL with stems using this model was 353.24 MHz which is similar to three cell model with constant drift tubes. The frequency shift for each cell is directly proportional to the cell volume removed due to stems and inversely proportional to the total cell volume. In the varying length model, the removed volume is same in each cell, while the total cell volume increases as the cell length increases. Therefore the increase in frequency due to the stem is lesser for higher energy cells. The field is proportional to the

frequency shift and so it decreases along the length of the DTL. The local frequency of each cell is also different but the global frequency of the cavity for both fixed-length model and the varying- length model are similar. This is because the length of the cell in fixed length model is that of the centre cell while in the varying length model half the cells have greater lengths than this and the other half cells have smaller lengths. Therefore the global change in frequency using both the models is same. Thus for a frequency analysis of the DTL, the constant length model is a good approximation, but when fields in individual cells have to be studied, the varying cell model is more appropriate.

2.2.2.2 Tuners

Slug tuners will be used to provide frequency adjustment to the RF cavity. The tuners are cylindrical rods which when pushed inside the DTL cavity decreases the magnetic volume of the cavity. This leads to a decrease in the inductance and hence an increase in the resonant frequency. According to the Slater's perturbation theorem [35] the frequency shift is given by,

$$\frac{\Delta f}{f} = \frac{\mu_0 \iint_{\Delta V} \left|\vec{H}\right|^2 dV - \varepsilon_0 \iint_{\Delta V} \left|\vec{E}\right|^2 dV}{\mu_0 \iint_{V} \left|\vec{H}\right|^2 dV + \varepsilon_0 \iint_{V} \left|\vec{E}\right|^2 dV}$$

where, dV is the change in cavity volume, V is the volume of the cavity without perturbation, $\vec{E}$ and $\vec{H}$ are the unperturbed electric and magnetic field amplitudes.

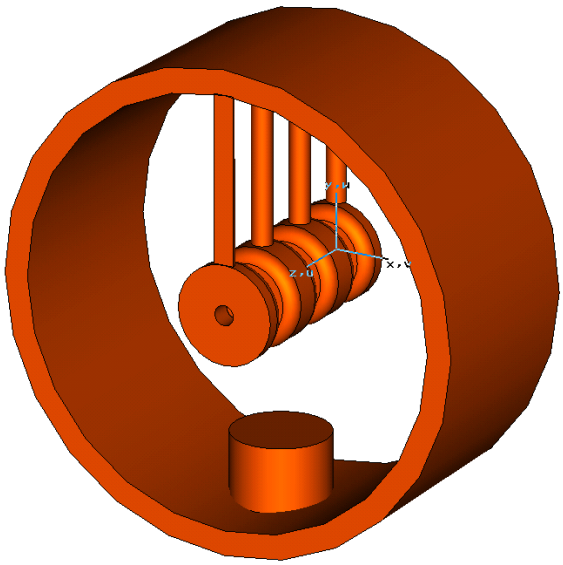

Fig. 2.16. A 3-cell model of a DTL cavity with Tuner.

The CST MWS model of a tuner is shown in Fig. 2.16. In the simulation, the frequency shift of one tuner is calculated. The variation of resonant frequency with tuner depth is shown in Fig. 2.17 and with tuner radius is shown in Fig. 2.18. As the tuner penetrates deeper into the cavity, the resonant frequency rises linearly until the tuner starts intercepting the electric volume. If the tuner is pushed further, the electric field starts dominating over the magnetic field, hence causing a decrease in resonant frequency. It can be seen from Fig. 2.17 that beyond a depth of 11 cm, the frequency does not increase much with any further tuner penetration. This will be the maximum depth to which the tuner will be penetrated inside the cavity and the frequency tunability for a single tuner is calculated to be 380.7 kHz.

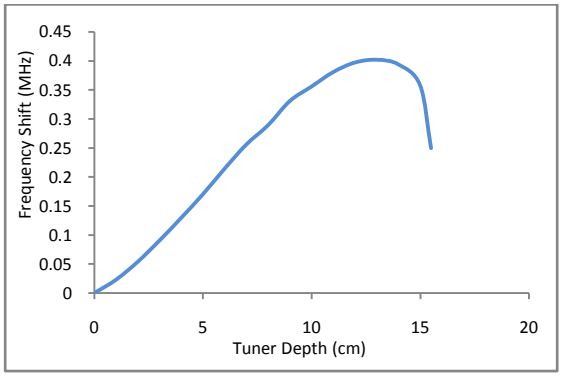

Figure 2.17.Variation of frequency with tuner depth.

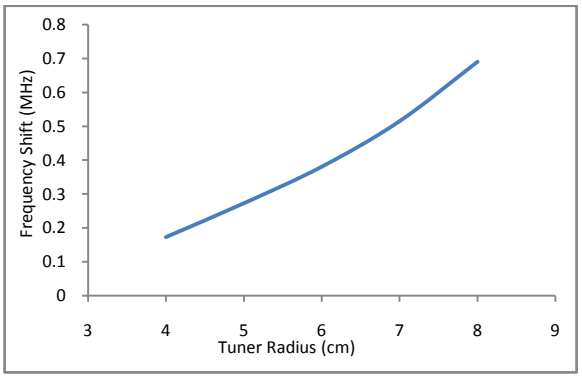

Figure 2.18.Variation of frequency with tuner radius.

Based on the simulations, it is planned to use 6 tuners per tank of length ~ 3 m. The tuning range using all the 6 tuners is estimated to be 2.28 MHz for a tuner diameter of 12 cm and a depth of 11 cm.

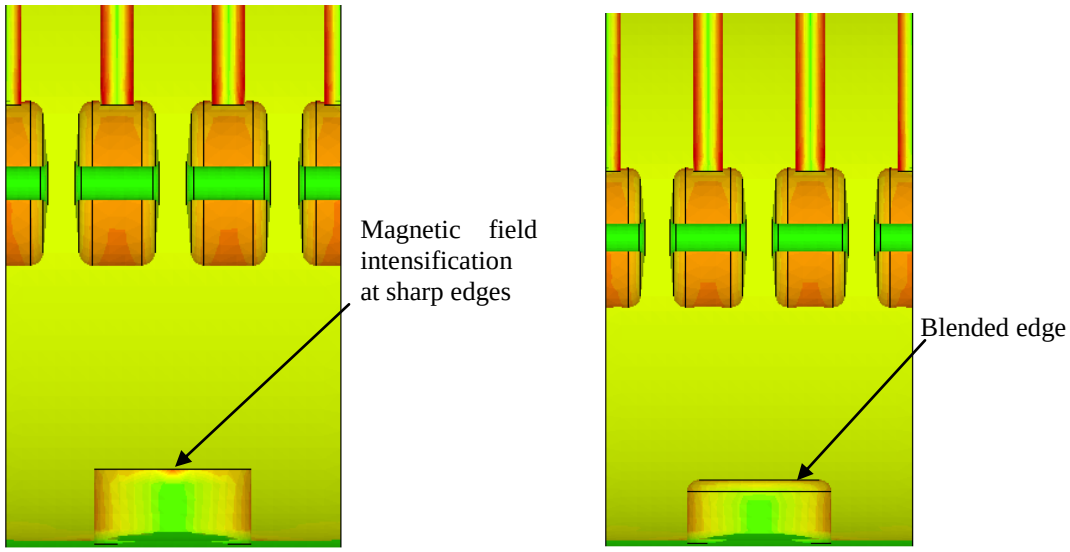

Fig. 2.19. Blending of tuner edges to reduce power dissipation.

By inserting the tuners inside the cavity, the concentration of the magnetic field at the edge of the tuner increases. Presence of sharp tuner edge leads to further increase in field, and hence increase in dissipated power at these locations. Therefore, the tuner

edges have been blended providing a blend radius of 5 mm (Fig. 2.19) in order to avoid sharp corners.

2.2.2.3 Vacuum Ports

The operating pressure for the DTL will be in the range of 10^{-7} Torr [36]. The primary requirement of DTL vacuum systems is to provide sufficient pumping to overcome the surface outgassing and maintain the operating pressure. In order to achieve this vacuum, pumping ports are provided on the tank walls. The apertures of the vacuum pumping ports are slotted in order to attenuate the RF power leaking out of the port and also to reduce the surface currents at the port corners, thus reducing the heat dissipation at these locations. The slot orientation is in the same direction as the RF currents. Two pumping ports will be provided in each DTL tank. A 5 slot configuration will be used for each port with a slot dimension of 14 cm x 1.8 cm and the spacing between two slots will be 1 cm. The conductance of each port is about 1400 l/s. A vacuum port modelled in CST Microwave Studio is shown in Fig. 2.20. The frequency shift due to the port openings is found to be 23.39 kHz, which is negligible. This is expected because the ports provide very small openings on the tank as compared to the tank volume.

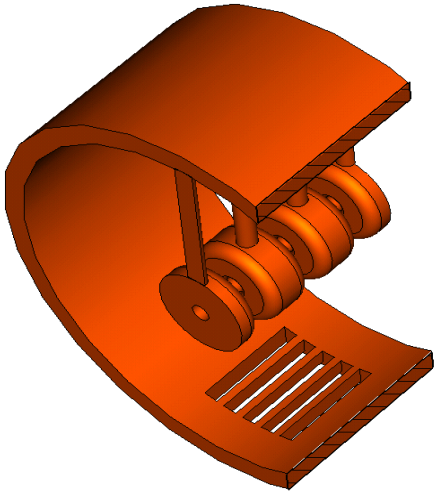

Fig. 2.20. DTL model with vacuum port.

2.2.2.4. RF Ports

Each tank of DTL will consists of two RF ports each. The slot dimension will be 12 x 1.5 cm per tank. The resonant frequency shift due to these ports has been calculated to be 11 kHz.

2.2.2.5. Postcouplers

The DTL operates in zero mode with same direction of accelerating field in each gap. For the zero mode, the group velocity $v_g = d\omega / dk_z$, which is the slope of the dispersion curve (ω-k curve) is zero (Fig. 2.21 a). There is therefore no energy propagation from one gap to the next and the electric field distribution becomes very sensitive to small frequency perturbations. For the π/2 mode, on the other hand, the group velocity is maximum. But this mode is inefficient for acceleration.

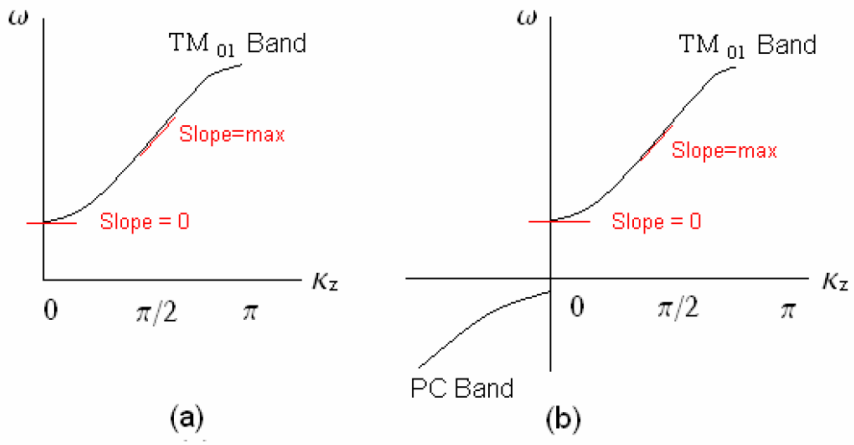

Fig.2.21. Dispersion curve for (a) TM_{01} band (b) TM_{01} and postcoupler (PC) band with a band gap in between (c) TM_{01} and PC mode at confluence.

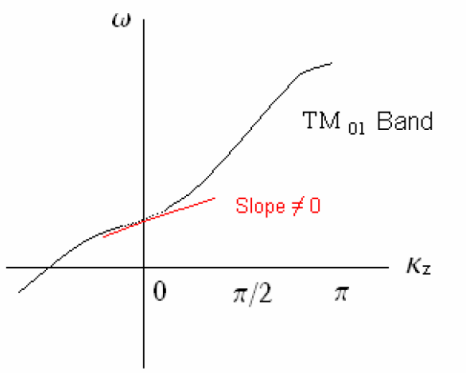

The slope of the dispersion curve at the zero mode is increased by introducing another resonator band and then coupling it to the TM_{01} mode band. This is done by inserting postcouplers in the horizontal plane at the drift tube centers. The postcoupler gives rise to a TE mode band as shown in Fig. 2.21 b. Maximum stabilization is achieved when the highest frequency of the TE mode becomes equal to the TM_{010} mode frequency (Fig. 2.21 c), resulting in a non-zero group velocity.

A nine-cell model of the DTL was used for simulations (Fig.2.22). The post couplers are located at the centre of every third drift tube in the first tank. In the second, third and fourth tank the post couplers will be placed at every alternate drift tube locations.

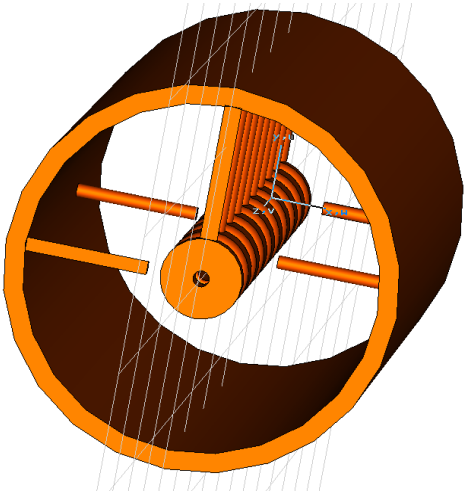

Fig. 2.22. Nine-cell model of the DTL with postcouplers.

The postcoupler stem represents an inductance while the gap between the post and the drift tube creates a capacitance [37]. Both elements form a resonant circuit whose frequency depends on the length and radius of the postcoupler. The capacitance also provides a coupling between the postcoupler mode and the acceleration mode. Thus, by changing the length and radius of the postcoupler, the TM_{010} mode frequency also changes. The effect of varying postcoupler length on the TM_{010} mode frequency is shown in Fig.2.23. It can be seen from this graph that as one reaches closer and closer to the point of confluence, the acceleration frequency becomes quite insensitive to the postcoupler length.

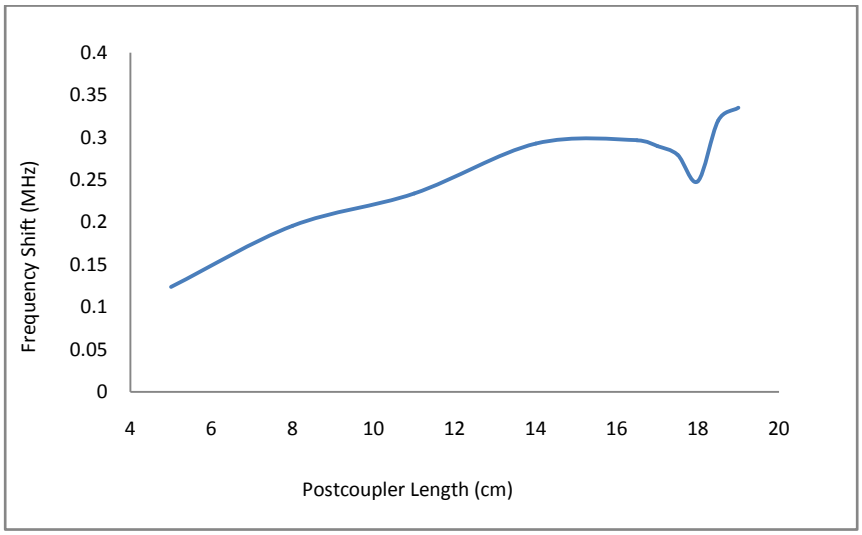

Fig. 2.23.Variation of frequency of the acceleration mode vs postcoupler length.

In order to find the postcoupler mode, the boundary conditions on both the end walls were set to ideal magnetic. The highest and the lowest mode which define the upper and lower boundary are shown in Fig.2.24. The highest mode has no electric field in the gaps between the drift tubes, while the lowest mode has finite electric field in the gaps.

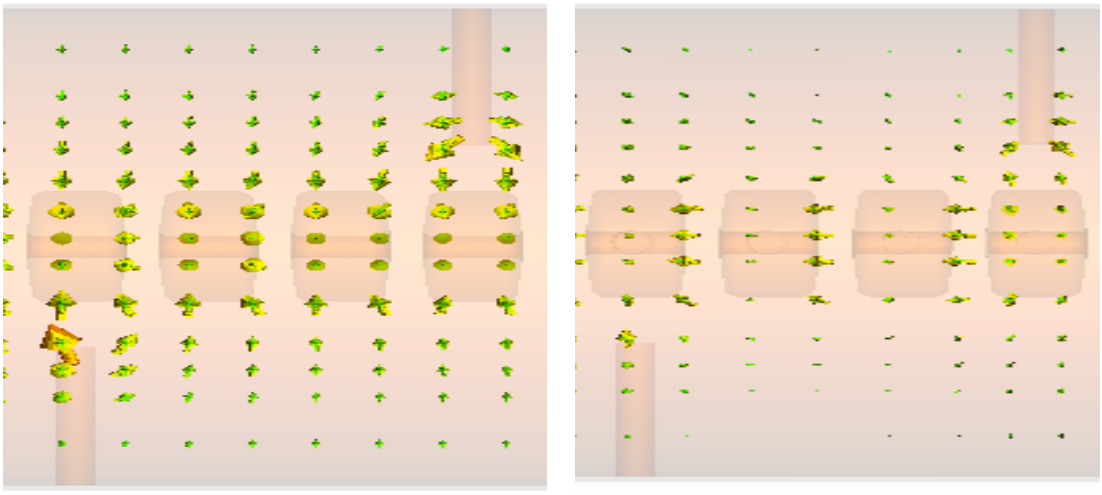

Fig. 2.24. Electric field of (a) highest and (b) lowest post coupler mode.

Fig. 2.25 shows the dispersion curves for the TM_{01} band, the post coupler band and the band of drift tube stems. Reducing the mode spacing between the highest post coupler mode and TM_{01} mode increases the stabilization. In a real tank, the highest post coupler mode cannot be excited because of the electric boundary conditions at both the end walls. However, these modes are excited when there is error leading to field difference between the cells. These modes then increase the group velocity of the dispersion curve to a non-zero value and allow the flow of energy between the cells.

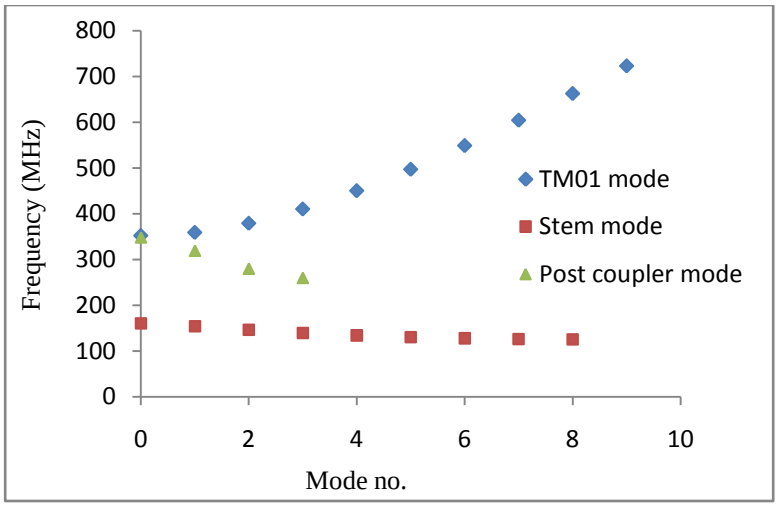

Fig. 2.25. Dispersion curve for nine-cell DTL TM_{010} mode, stem mode and post coupler mode.

The postcoupler mode frequency as a function of postcoupler length and radius is shown in Fig. 2.26. It can be seen from this graph that the postcoupler mode frequency is quite sensitive to the changes in postcoupler length. From this figure we can interpolate the postcoupler length for different radii as summarized in Table 2.2.

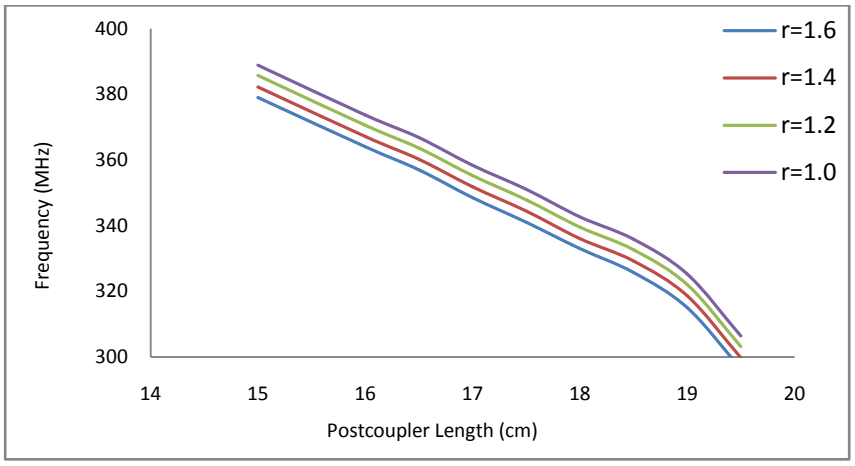

Fig. 2.26. Postcoupler mode frequency vs. postcoupler length.

Table 2.2. Optimum Postcoupler radii and lengths for maximum stabilization.

PC radius (cm)	PC length (cm)
1.0	17.35
1.2	17.1
1.4	16.95
1.6	16.8

Tilt Sensitivity

The field stabilization [38] with postcouplers is studied using the tilt sensitivity technique. In order to calculate the tilt sensitivity, first the electric field distribution is determined along the axis for all cells in the simulation model. Then an error is created by changing the drift tube lengths in the end cells giving rise to opposite frequency shifts

and the electric field distribution is again determined. The tilt sensitivity [39] can be calculated from the difference in electric fields as

$$TS_i = \frac{|E_e|_i - |E_b|_i}{|E_b|_i} \times \frac{1}{\delta f_i} \times 100\%$$

where $|E_e|_i$ is the electric field with error for cell i, $|E_b|_i$ is the electric field without error for cell i and δf_i is the frequency shift caused by the error.

For the nine-cell model of constant drift tube length, the field pattern is as shown in Fig. 2.27. As can be seen from this graph, the electric field amplitudes in all the gaps are nearly equal. After introduction of error the electric field pattern is as shown in Fig. 2.28.

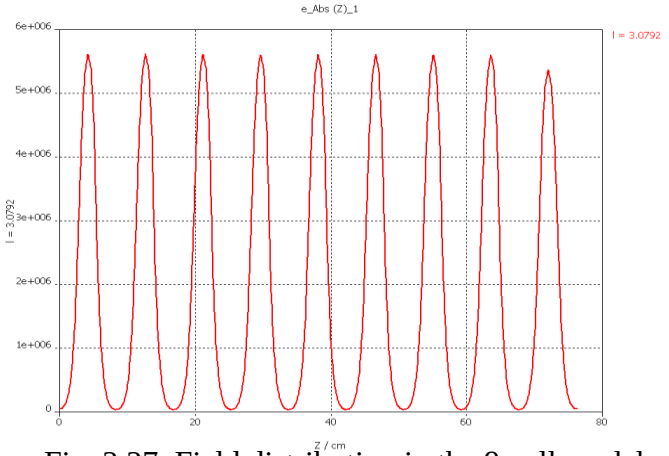

Fig. 2.27. Field distribution in the 9-cell model.

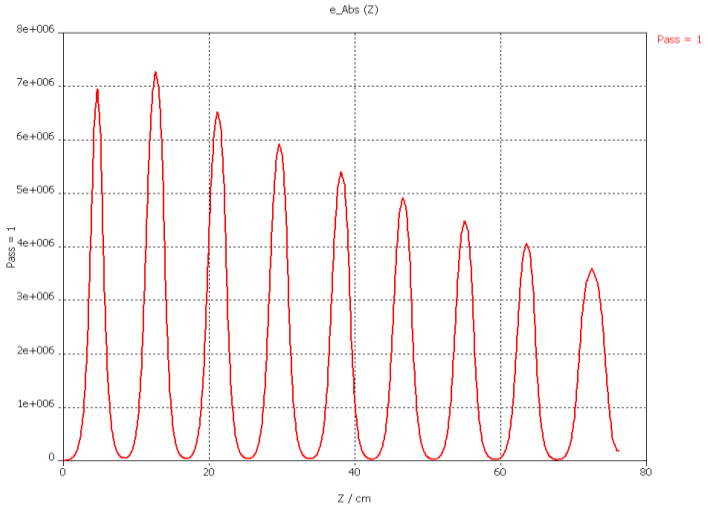

Fig. 2.28. Field distribution with end cell errors.

The postcoupler is then introduced into the model with error in the end cells. The effect on field distribution of the postcoupler whose length and radius has been optimized for maximum stabilization is shown in Fig. 2.29.

The tilt sensitivity has been calculated for each cell before and after inserting the postcouplers (Fig.2.30). As can be clearly seen, there is a considerable reduction in the tilt sensitivity slope after inserting the postcouplers.

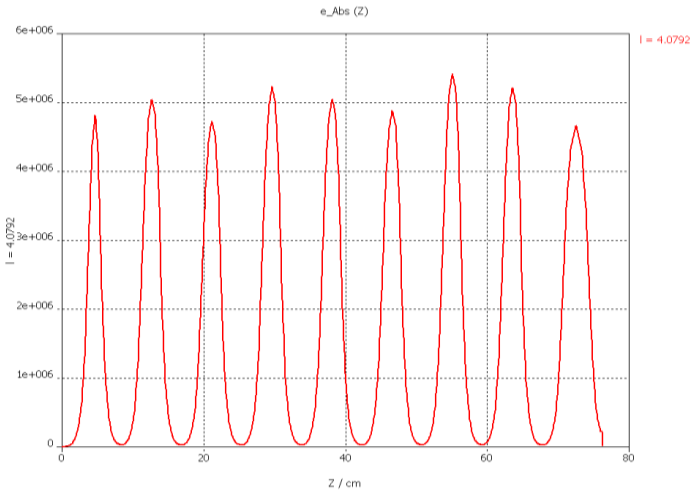

Fig. 2.29. Field distribution after inserting optimized postcouplers.

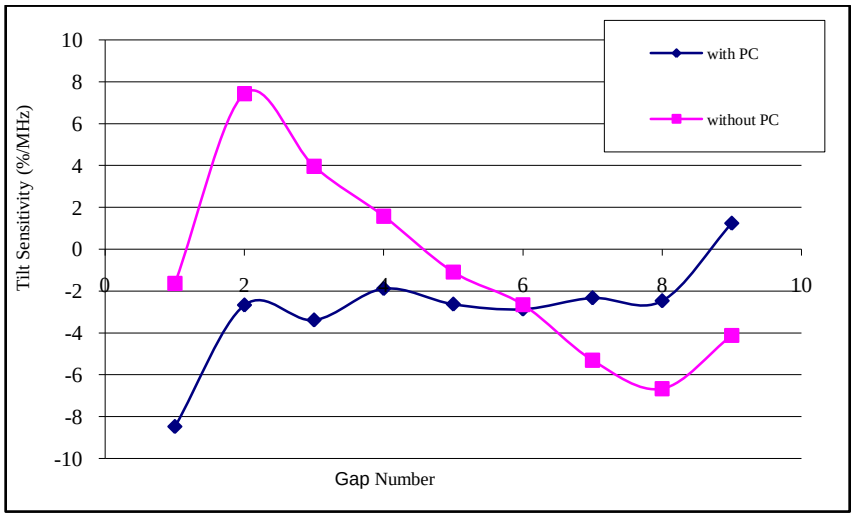

Fig. 2.30. Field Tilt sensitivity with end cell errors.

From the tilt sensitivity analysis, it is concluded that it is sufficient to have one postcoupler at every third drift tube for tank 1. In tank 2, 3 and 4, since the cell lengths are longer, we need to put a postcoupler at every alternate drift tube. Simulations show that the error-induced tilt sensitivity slope increases if there are lesser number of postcouplers. Therefore, it is planned to have one postcoupler at every third drift tube for tank 1 and at every alternate drift tube for tanks 2, 3, and 4.

CHAPTER 3

Beam Dynamics Studies

3.1 Energy gain in a standing-wave cavity

In an accelerating gap the electric field on the axis experienced by a particle with velocity v can be expressed as

$$E_z(\mathrm{r} = 0, \mathrm{z}, \mathrm{t}) = \mathrm{E}\ (0, \mathrm{z})\ \cos\ (\omega \mathrm{t}(\mathrm{z}) + \phi) \tag{3.1}$$

where $t(z) = \int_0^z dz/v(z)$, is the time the particle is at position z. The time t =0 is chosen when the particle is at origin. At t = 0, the phase of the field relative to the crest of the field is ϕ. Supposing the field is confined within an axial distance L containing the gap, the energy gained by a charged particle on-axis in the cavity is

$$\Delta W = \int_{-L/2}^{L/2} q\ E(0,z) \cos(\omega t(z) + \phi)\ .\ dz \tag{3.2}$$

where q is the particle charge.

Using trigonometric identity, the energy gain can be written as,

$$\Delta W = q \int_{-L/2}^{L/2} E(0,z).\ (\cos \omega \mathrm{t} \cos \phi - \sin \omega \mathrm{t} \sin \phi)\ \ dz \tag{3.3}$$

Defining an axial RF voltage as,

$$V_0 = \int_{-L/2}^{L/2} E(0,z) dz \tag{3.4}$$

and transit-time factor as,

$$T = \frac{\int_{-L/2}^{L/2} E\ (0,z) \cos\ \omega t\ (z)\ dz}{\int_{-L/2}^{L/2} E\ (0,z) dz} - \tan \phi\ \frac{\int_{-L/2}^{L/2} E(0,z) \sin\ \omega t\ (z) dz}{\int_{-L/2}^{L/2} E\ (0,z) dz} \tag{3.5}$$

The energy gain can be written in the form

$$\Delta W = q\ V_0 T \cos \phi \tag{3.6}$$

Maximum energy gain occurs when ϕ = 0, that is when the particle is at the crest. V_0 , the axial RF voltage is the voltage gain experienced by a particle passing through a constant dc field equal to the field in the gap at time t = 0. $E_0 = V_0/L$ is defined as an average axial electric field over the length L. The quantity E_0 depends on the choice of L. the energy gain can be expressed in terms of E_0 as

$$\Delta W = q\, E_0 T \cos\phi\, L \tag{3.7}$$

Regardless of the phase ϕ, the energy gain of a particle in a harmonically time-varying field is always less than the energy gain in a constant dc field equal to that seen by the particle at the centre of the gap. This is known as the transit time effect. The transit time factor, which is the ratio of energy gained in time varying RF field to that in a dc field of voltage $V_0 \cos\phi$, is a measure of the reduction in energy gain caused by the sinusoidal time variation of the field in the gap.

3.2 Longitudinal Beam Dynamics

A linac design is done for a single particle, which remains in synchronism with the accelerating field and is called synchronous particle. For a good beam transmission, there needs to be a restoring force in longitudinal as well as transverse direction, so that particles near the synchronous particles have stable trajectories.

A longitudinal restoring force exists when the synchronous phase is chosen corresponding to an electric field that is rising in time. The longitudinal particle motion is described by the coupled differential equations:

$$\gamma_s^3 \beta_s^3 \frac{d\,(\varphi-\varphi_s)}{ds} = -2\pi \frac{W-W_s}{mc^2\lambda} \tag{3.8}$$

$$\frac{d\,(W-W_s)}{ds} = qE_0T(\cos\varphi - \cos\varphi_s) \tag{3.9}$$

where W_s and φ_s are the energy and phase of synchronous particle and W and φ are the energy and phase of any other particle. E_0 is the average accelerating field and T is the transit time factor. These equations lead to the following trajectory equation in the energy-phase plane.

$$\frac{Aw^2}{2} + B\,(\sin\varphi - \varphi\cos\varphi_s) = H_\varphi \qquad (3.10)$$

where $A = \frac{2\pi}{\beta_s^3\gamma_s^3\lambda}$, $B = \frac{qE_0T}{mc^2}$ and $w = \frac{W-W_s}{mc^2}$

the quantity H_φ is a constant of integration. The first term in (3.10) is kinetic energy term and the second term is the potential energy term. A potential well exists when $-\pi < \varphi_s < 0$. Acceleration takes place when $-\pi/2 < \varphi_s < \pi/2$. Therefore, for simultaneous acceleration and potential well, $-\pi/2 < \varphi_s < 0$. There is a potential maxima at $\varphi = -\varphi_s$. Therefore, at $\varphi = -\varphi_s$, $\varphi' = 0$ and therefore w = 0 (from (3.8)). Thus the trajectory equation becomes,

$$\frac{Aw^2}{2} + B(sin\,\varphi - \varphi\cos\varphi_s) = -B\,(\sin\varphi_s - \varphi_s\cos\varphi_s) \qquad (3.11)$$

which represents the separatrix, the area within which the trajectories are stable. The separatrix phase width Ψ can be calculated from the synchronous phase by the equation below:

$$\tan\varphi_s = \frac{\sin\Psi - \Psi}{1-\cos\Psi} \qquad (3.12)$$

At $\varphi_s = -90^0$, the phase acceptance is maximum extending over full 360^0. The maximum energy extent of the separatrix occurs at $\varphi = \varphi_s$ and can be obtained by solving the separatrix equation as

$$w_{max} = \sqrt{\frac{2qE_0T\beta_s^3\gamma_s^3\lambda}{\pi m c^2}\,(\phi_s cos\phi_s - \sin\phi_s)} \qquad (3.13)$$

3.3 Transverse Beam Dynamics

A linac design needs to ensure that a particle that is off-axis, neither drifts away nor is subject to transverse defocusing forces that carries it farther away from the axis.

3.3.1 Transverse RF Defocusing

The RF fringe fields in a gap impart a radial momentum impulse to the off-axis beam particles. Though the radial electric forces at the entry and the exit of the gap are oppositely directed, they do not lead to exact cancellation in the total radial momentum impulse due to the time varying field in the gap. For longitudinal stability ϕ_s must be negative, which means that the field rises in time when the particle is injected. Therefore, the field experienced in the second half of the gap is higher than the field in the first half. Since the field in the first half is focusing and that in the second half is defocusing, the net effect is a defocusing force. The transverse defocusing effect of RF fields is a consequence of Laplace's equation which does not allow for any maxima or minima of the electric potential in free space. A potential minima corresponds to a net focusing in all directions and maxima corresponds to a net defocusing in all directions. Both the conditions are incompatible with Laplace's equation. Therefore, if the longitudinal forces provide focusing at a particular point, both the transverse components cannot be focusing at the same point.

The transverse equation of motion for a particle experiencing a transverse momentum impulse from the RF fields is given by

$$\frac{1}{\gamma_s \beta_s}\frac{d}{ds}\gamma_s \beta_s r' - \frac{k_{l0}^2}{2} r = 0 \qquad (3.14)$$

where $k_{l0} = \frac{2\pi q\, E_0 T sin\ (-\phi)}{m c^2 \lambda (\gamma\beta)^3}$ is defined as the longitudinal wave number.

3.3.2 Quadrupole Focusing in a Linac

Magnetic quadrupoles [40] are used to compensate for the transverse RF defocusing effects in drift tube linacs. The quadrupoles are installed inside the drift tubes of a DTL. For a particle moving along the z direction with velocity v and with transverse coordinates (x,y) the Lorentz force components are

$$F_x = q\ v\ G_x \qquad\qquad F_y = q\ v\ G_y \tag{3.15}$$

If qG is positive, the lens focuses in x and defocuses in y. Although individual quadrupole lenses focus in only one plane, they can be combined with both polarities to give overall strong focusing in both transverse planes. The equation of motion for a particle with charge q moving parallel to the beam axis with velocity β and transverse coordinates x and y, through a perfect quadrupole lens with axial position s as the independent variable are

$$\frac{d^2x}{ds^2} + k^2(s)x = 0 \qquad \text{and} \qquad \frac{d^2y}{ds^2} + k^2(s)y = 0 \tag{3.16}$$

where $k^2(s) = \left|\frac{q\ G\ (s)}{mc\gamma\beta}\right|$

The effect of RF defocusing term can be included in the equation of motion to write

$$\frac{d^2x}{ds^2} + k^2(s)x - \frac{k_{l0}^2}{2}x = 0 \quad \text{and} \quad \frac{d^2y}{ds^2} + k^2(s)y - \frac{k_{l0}^2}{2}y = 0 \tag{3.17}$$

The above equations constitute a restoring force that is linear function of the displacement from the equilibrium trajectory and forms an example of Hill's equation.

A quadrupole transport channel can be described by the Hill's equation

$$\frac{d^2x}{ds^2} + K(s)x = 0 \tag{3.18}$$

When K(s) is a periodic function, the general solution to the Hill's equation can be written as

$$x(s) = \sqrt{\varepsilon\beta(s)}\cos[\phi(s) + \phi_1] \tag{3.19}$$

Where β(s) is the amplitude function and ϕ(s) is the phase advance, and ε and ϕ_1 are constants determined by the initial conditions. The phase advance gives an idea of the focusing in the linac. The amplitude and phase functions are related as

$$\phi(s) = \int \frac{ds}{\beta(s)} \tag{3.20}$$

Two other functions of β_s are defined as

$$\alpha(s) = -\frac{1}{2}\frac{d\beta(s)}{ds} \quad \text{and} \quad \gamma(s) = \frac{1+\alpha(s)^2}{\beta(s)} \tag{3.21}$$

The quantities α(s), β(s) and γ(s) are called the Twiss or Courant-Snyder parameters. These are periodic functions with the same period as K(s). The trajectory of a particle in the x-x' space is given by

$$\gamma(s)x^2 + 2\alpha(s)xx' + \beta(s)x'^2 = \varepsilon \tag{3.22}$$

Equation (3.22) is the general equation of an ellipse centred at the origin of x-x' space, with an area of πε.

In the design of linacs, two more quantities are of importance; the phase advance per focusing period, σ_t and the phase advance per unit length, k_t . The phase advance per focusing period is also known as tune, and physically represents the spatial frequency of transverse oscillation period.

At low energies and high currents, a linac is dominated by space charge. The effect of space charge force is to reduce the net focusing of the beam particles. The transverse equation of motion with space charge is modified as,

$$\frac{d^2x}{ds^2} + k^2(s)x - F_{SC} = 0$$

and $$\frac{d^2y}{ds^2} + k^2(s)y - F_{SC} = 0 \quad (3.19)$$

where F_{SC} is the space charge force. The tune of transverse oscillation suffers a depression due to the defocusing Coulomb force. The depressed tune is the net focussing in the presence of space charge and the tune depression, that is the ratio of tunes with and without space charge represents the intensity of the space charge defocusing. Space charge also leads to defocusing in the longitudinal plane, and the quantities like depressed tune and the tune depression are relevant in this plane too.

3.3.3 Beam Matching

If the injected beam ellipse is not matched to the focusing system, there will be additional oscillations of the RMS beam projections, which produce a larger beam at some locations and a smaller beam at other locations. Beam matching implies that the beam density contours coincide with the ellipses corresponding to the particle trajectories. At every point in the focusing lattice, there exists a matched beam condition, defined by the Courant Snyder ellipse parameters, α_m, β_m, γ_m. In general, the beam will have ellipse parameters that may differ from the matched values of the structure. It is therefore important to match the beam to the structure by using a matching line, comprising focusing elements and RF bunchers, which transitions the beam ellipse to match the structure acceptance. In the beam dynamics design, special care is taken to match the beam to the focusing lattice at each structure transition.

3.4 Beam Dynamics Simulations

3.4.1 Design Approach

The computer codes Parmila [41] and Tracewin [42] were used to study the beam dynamics in the DTL structure. Detailed simulation studies were performed to evolve an optimized design. The main design criteria was

- minimizing the emittance growth.
- the zero current phase advance is kept below 90º [43], so as to avoid space charge induced beam instabilities.
- an aperture to rms beam size ratio of 8 is maintained in the DTL in order to avoid beam losses. This is very important for a high current DTL where space charge forces are significant.

3.4.2 Choice of focusing lattice

Quadrupoles are used for transverse focusing of the beam in the DTL. The most commonly used focusing lattices are FD [44], FFDD [45] and FFODDO [46]. All the three lattice configurations were studied for focusing. The beam in the DTL will be coming from an RFQ. The phase advance per unit length should be constant along the linac for current independent matching[47]. The focusing period in the RFQ is $\beta\lambda$. The focusing periods in FD, FFDD and FFODDO lattices are 2 $\beta\lambda$, 4 $\beta\lambda$ and 6 $\beta\lambda$ respectively and therefore the transverse phase advance for the three lattices are 2, 4 and 6 times the phase advance in the RFQ. In order to match the phase advance per unit length, the quadruople strengths will have to be different for the three lattices.

The matched beam parameters are calculated for each lattice and given at the input of the DTL while running the simulation. The beam dynamics results for the three

lattices are compared in Table 3.1. The RMS beam size for the three lattices is plotted in Fig. 3.1. While the FD lattice provides smaller beam sizes, the quadrupole gradient required is 83 T/m. With the space for quadrupoles limited by the drift tube geometry, such high gradients are difficult to achieve. In FFDD, while the beam size is ~18 % higher than FD, the quadrupole gradients required are almost half of the FD lattice. The FFODDO lattice has the advantage that it offers space for diagnostics and beam steering elements in every third drift tube. However, the beam size and emittance growth (33 %) in this lattice is the highest. Therefore, as a best compromise on all factors, we choose the FFDD lattice for our DTL.

Table 3.1. Comparison of FD, FFDD and FFODDO lattices.

Parameters	FD	FFDD	FFODDO
Quadrupole Gradient (T/m)	83	46.5	32.5
Maximum RMS Beam Radius (cm)	0.12	0.14	0.19
Radius of outermost particle (cm)	0.21	0.29	0.40
Norm. RMS Emittance in x (pi cm mrad	0.0206	0.0217	0.0267
Norm. RMS Emittance in y (pi cm mrad)	0.0207	0.0206	0.0278
Long. Emittance (deg-MeV)	0.114	0.114	0.114

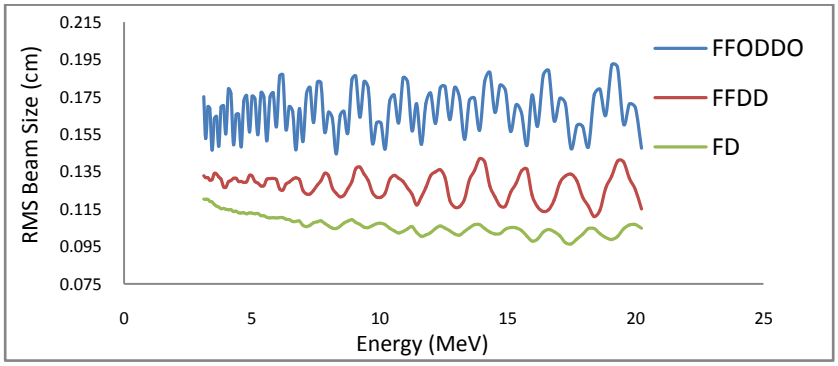

Fig. 3.1. RMS beam size in FD, FFDD and FFODDO lattices.

The beam size variation when there is a 10% mismatch in the input beam parameters, for all three lattices was also studied. These results are shown in Fig. 3.2. It can be seen that with mismatch there is a significant increase in the beam flutter for the FD lattice. For the FFDD lattice the increase is small, and for the FFODDO lattice the increase is negligible. Therefore, the choice of the FFDD lattice is quite stable under beam parameter mismatch.

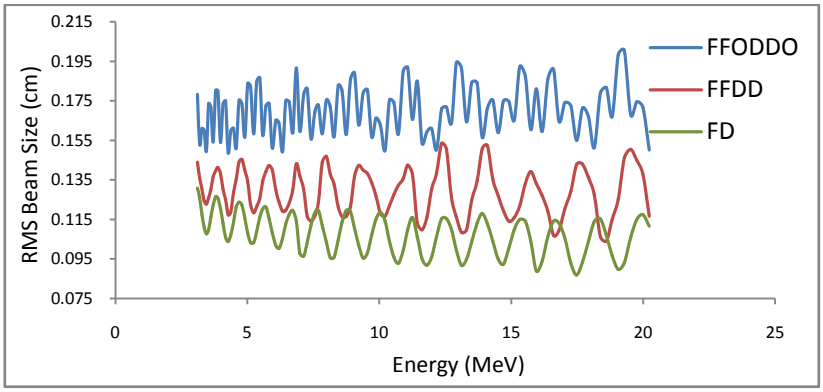

Fig.3.2. RMS beam size in FD, FFDD and FFODDO lattices with 10 % input beam mismatch.

Permanent magnet quadrupoles (PMQs) [48, 49] will be used for the transverse focusing of the beam. The Electromagnetic quadrupoles (EMQs) can provide adjustable focusing, but require larger space inside the drift tubes. The diameter of the drift tube is limited by the requirement for high effective shunt impedance. Further, beam dynamics constrains the initial drift tubes to very small lengths (~ 5 cm). Housing EMQs in such a limited space would be very difficult. Therefore, it is decided to use PMQs for focusing.

Detailed beam dynamics simulations were done with FFDD lattice. In order to match the transverse phase advance per unit length between the RFQ and the DTL the phase advance in the DTL should exceed 90^0. However, in order to avoid space charge induced

envelope instability, the zero current phase advance in the DTL is kept just under 90º [50] thus allowing slight mismatch in the transverse phase advance.

For ease of fabrication, the quadrupoles have been divided into 5 groups, each having different gradients. The quadrupole gradients are ramped down along the DTL so as to keep phase advance between 82º and 89º.

The aperture is kept about 8 times the rms beam size everywhere in the DTL. The beam profile at the DTL output is shown in Fig. 3.3. The final set of output parameters are listed in Table 3.2. The RMS beam size along the length of the linac is shown in Fig. 3.4. The normalised RMS emittance of the beam in all three planes is plotted in Fig. 3.5.

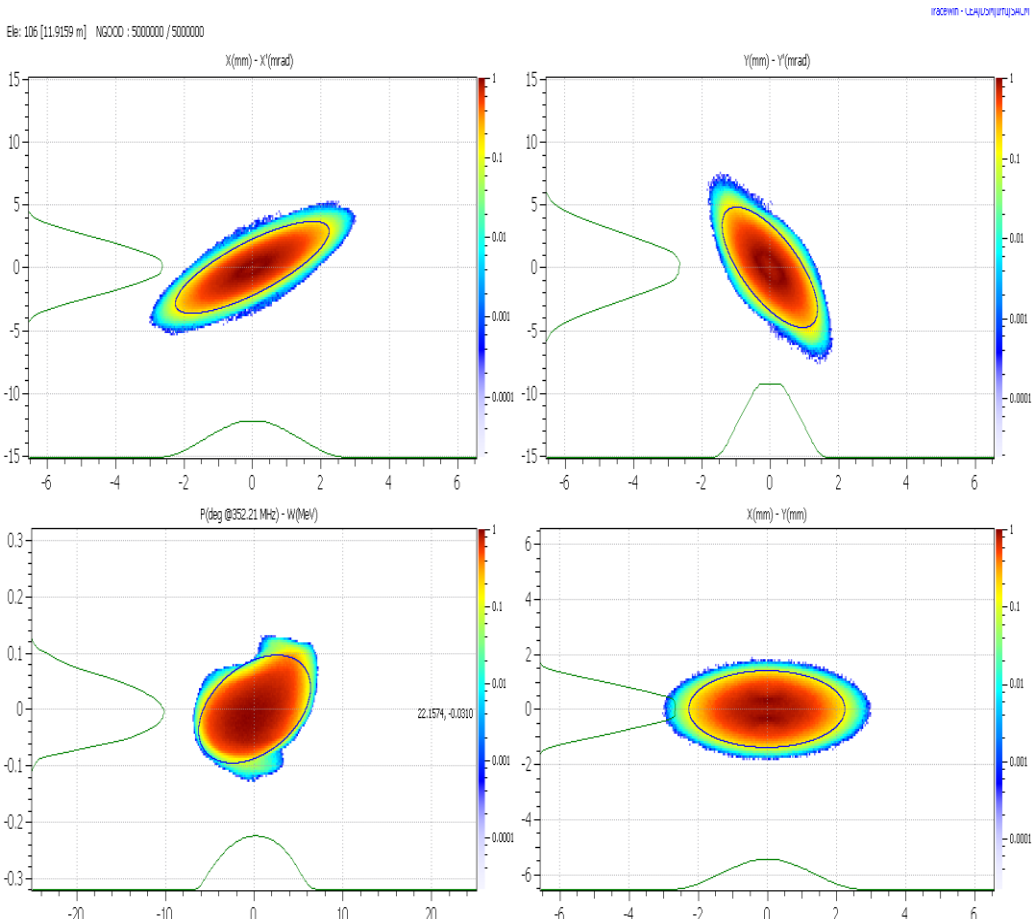

Fig.3.3. Beam profile in x-x', y-y', Δϕ-ΔW and x-y at the DTL output.

Table 3.2: Parameters of the DTL.

Parameters		**Tank 1**	**Tank 2**	**Tank 3**	**Tank 4**
Input Energy (MeV)		3.03	6.92	11.28	15.73
Output Energy (MeV)		6.92	11.28	15.73	20.15
No. of cells		35	25	20	17
Lattice period		4 βλ	4 βλ	4 βλ	4 βλ
Eff. Length of quad (cm)		4.715	4.715	4.715	4.715
No. of quads.		36	26	21	18
Aperture radius (cm)		1.2	1.2	1.2	1.2
Synchronous phase		-30	-30	-30	-30
Acc. Field grad. (MV/m)		2.14	2.14	2.14	2.14
Total Power (kW)		399.90	374.21	368.95	358.35
Tank Length (m)		297.868	291.826	284.715	278.407
Drift Space at the end of tank (cm)		5.518	8.352	10.684	
Norm. RMS Emittance	x(π cm mrad)	0.02086-0.02164	0.0218	0.02193	0.02172
	y(π cm mrad)	0.02102-0.02053	0.02051	0.02025	0.02057
Long. Emittance(deg. MeV)		0.10902-0.11222	0.11044	0.11307	0.11409

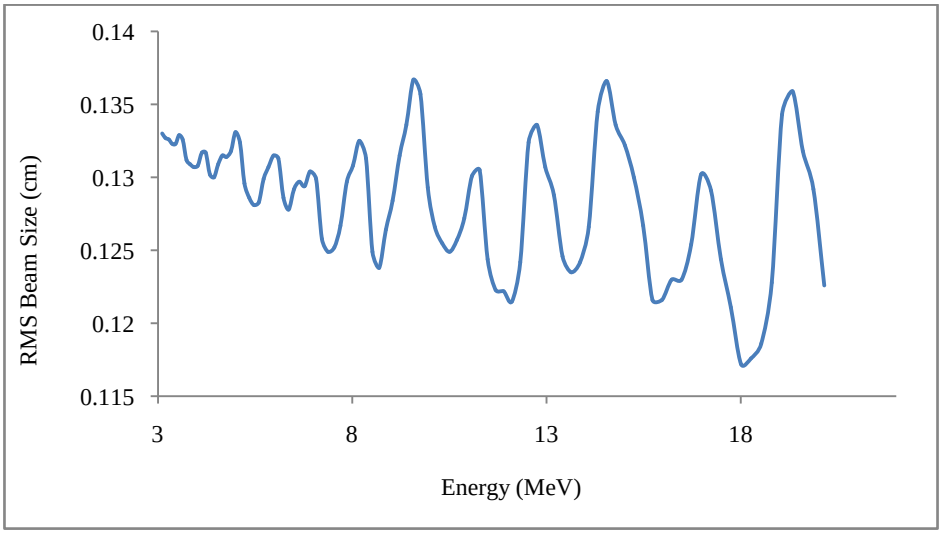

Fig.3.4. RMS Beam size along the linac.

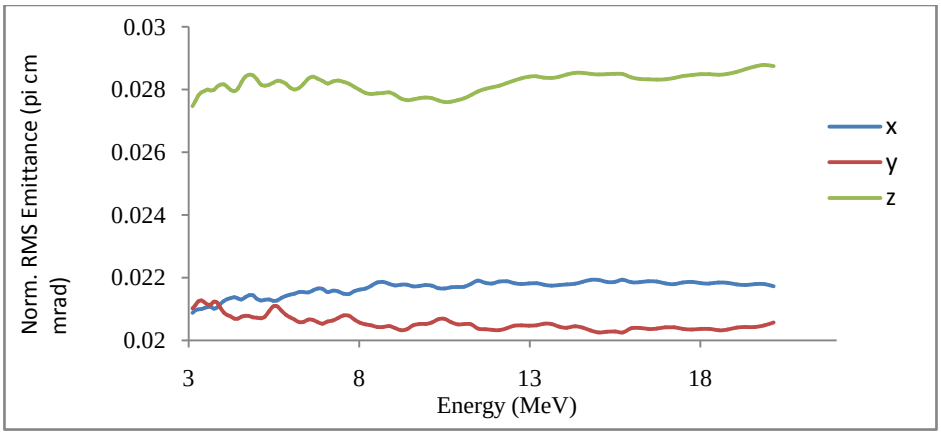

Fig. 3.5.Normalised RMS emittance of the beam along the DTL.

3.4.3 Effect of Space Charge on Beam Dynamics

In high current linacs for non-relativistic beams at low velocities, the Coulomb interactions are very important. To describe the space-charge field, one needs to understand the properties of an evolving particle distribution, which requires a self-consistent solution for the particles and the associated fields. The significance of the space-charge fields is not only that they reduce the effective focusing strength, but also the nonlinear terms, a consequence of the deviations from charge-density uniformity, cause growth of the rms emittances, which degrades the intrinsic beam quality.

For a space-charge dominated beam, the distribution tends to be uniform. On the other extreme, an emittance dominated beam tends to have a Gaussian distribution [51]. The real beam distribution [52, 53] through the linac can be anywhere between the two. A uniform beam is characterized by linear space charge forces and a Gaussian beam, on the other hand, has a highly non-linear space charge. In order to estimate the effect of space charge on the beam dynamics of 30 mA proton beam through the DTL, simulations

were carried out (a) without space charge, (b) with linear space charge (uniform beam at the DTL input) and (c) with Non-linear space charge (Gaussian distribution at the DTL input). For a beam without space charge, no emittance growth was observed in simulations. Even with linear space charge forces, the emittance growth was not very significant. In the case of non-linear space charge, the transverse emittance growth was 3.1 %, which is still tolerable for the 20 MeV DTL. The longitudinal emittance growth is 17.5 % which is quite high. The transverse and longitudinal emittances of the beam along the linac are plotted in Fig. 3.6 for a 30 mA proton beam without space charge and with linear and non-linear space charges.

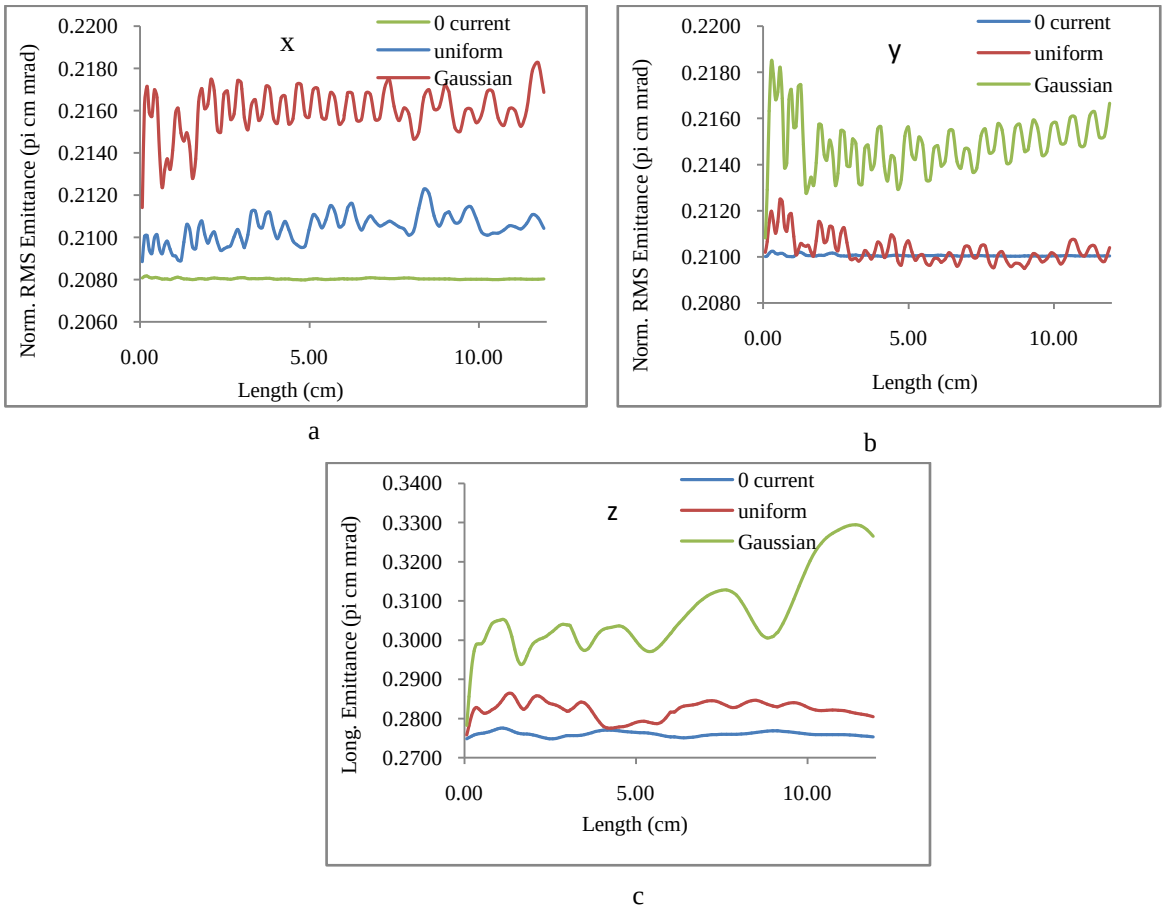

Fig. 3.6. Normalised RMS Emittance in (a) x-x' (b) y-y' and (c) z-z' plane along the DTL length.

Hoffmann chart [54], showing tune footprints (Fig. 3.7), was computed using Tracewin. The coloured regions depict the resonance region, corresponding to various k_z/k_{xy} ratios. If these regions are crossed at a sufficiently slow rate, the collective space harge instabilities tend to cause emittance exchange between longitudinal and transverse planes leading to the "equipartitioning" phenomena [55]. The most serious resonance occurs at $k_z/k_{xy} = 1$. As can be seen from Fig. 3.7, there is no overlap of the tunes with this resonance in our design. For a few periods, the tune ratio is found to be crossing the resonance at tune ratio of 0.3. However, this does not have any serious implication on the beam dynamics as emittance blow up is not observed in the simulations. This is because the fourth order resonances are not important for linacs. Also the growth rate of emittance exchange is very low at the points where the tune ratio crosses the resonance. Thus, the DTL design avoids the space charge instabilities.

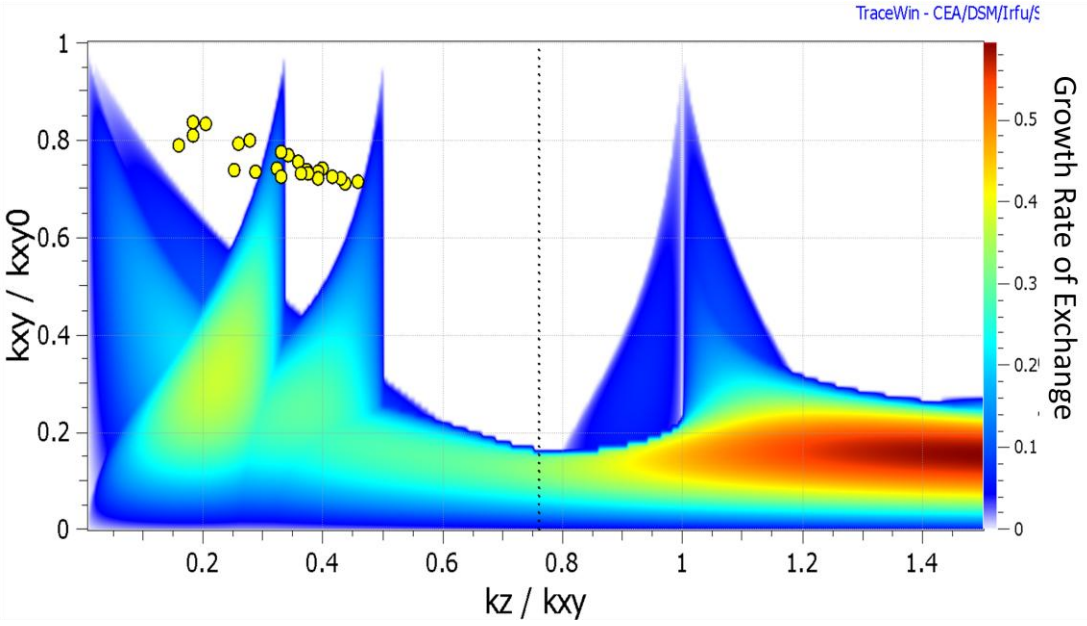

Figure 3.7. Hoffman chart for the DTL.

The effect of space charge forces were studied for different tune depression, by varying the beam current. The tune depression is the ratio of full current phase advance to the zero current phase advance. If the tune depression is close to 0, the beam is highly dominated by space charge and if it is close to 1, the beam is completely devoid of space charge effects. A tune depression below 0.4 implies intense space charge forces, and onset of chaotic behaviour [56]. The tune depressions for different beam currents are plotted in Fig. 3.8. It can be seen from the figure that the transverse tune depression in all the four cases is above 0.6. For 10 mA, it is close to 0.9, implying minimal space charge while for 40 mA, it is close to 0.7, implying moderate space charge. The longitudinal tune depression is however, close to intense space charge limit of 0.4 for all currents above 10 mA. For currents of 30 and 40 mA, the tune depression crosses below 0.4 at few periods.

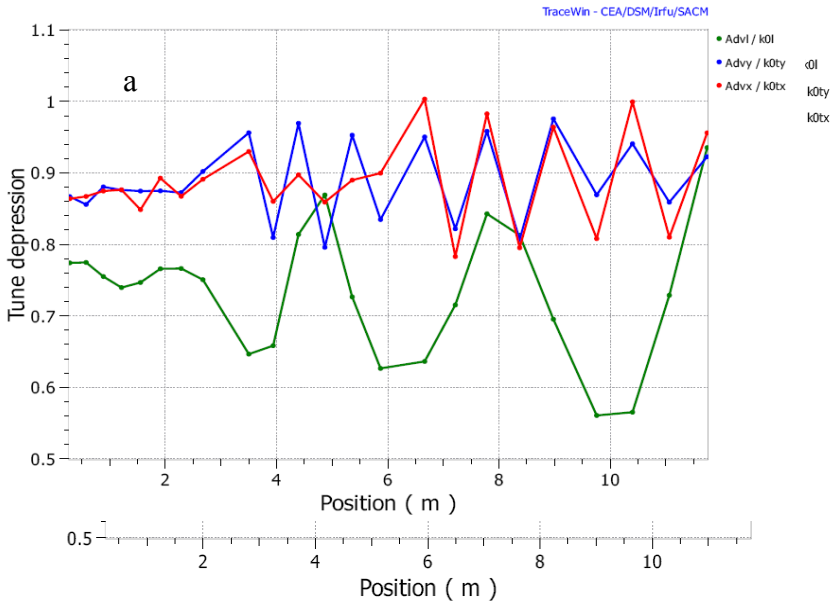

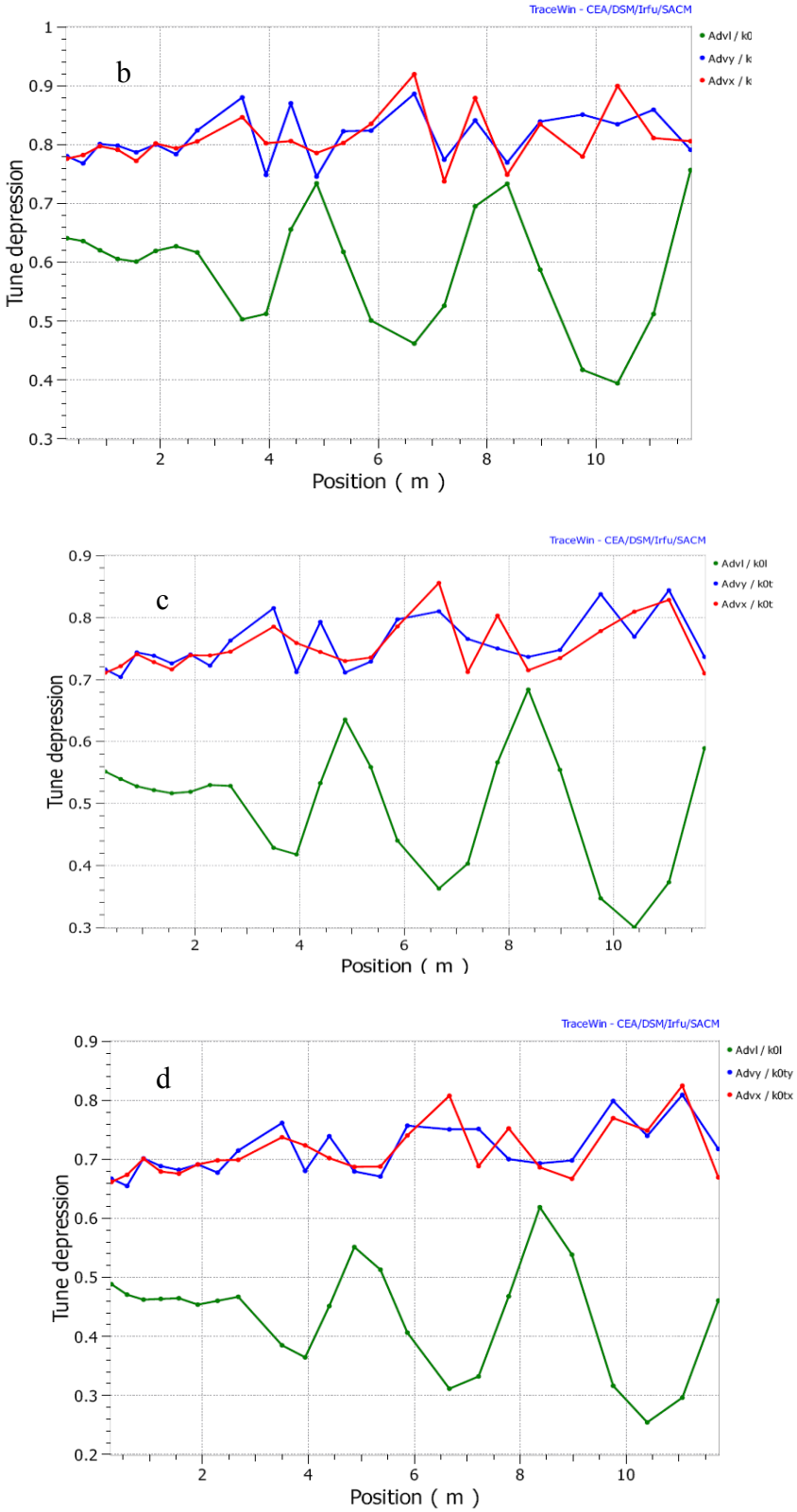

Fig. 3.8.Tune depression for (a) 10 mA (b) 20 mA (c) 30 mA (d) 40 mA.

For a 10 mA beam, there was very little increase in the emittance in all planes because the space charge forces are not strong enough at this current. For 40 mA beam, on the other hand, the emittance growth is very high. The longitudinal emittance increase is significantly large at currents of 20 mA and more. The transverse emittance also increases with increasing beam currents. The beam profile at the end of the linac is shown in Fig. 3.9 for different beam currents. This figure clearly indicates filamentation of the beam profile in the longitudinal plane, which begins at 20 mA and increases significantly for higher currents. The transverse phase space also starts to show slight distortion at 20 mA and higher currents. The transverse beam, with stronger focusing experiences lesser effects of space charge. However, the beam in the longitudinal plane with lower tune depression values experiences serious phase space distortion. The emittance growth and rms beam size in the linac for different currents are listed in Table 3.3 for an input Gaussian beam. From these studies, we conclude that the space charge effects are not significant at around 10 mA. If the tune depression is close to or goes below 0.4 even for a few periods, there is significant distortion in phase space and a consequent increase in emittance. For the designed DTL at 30 mA, space charge effects are observable and lead to emittance growth. In the presence of beam mismatch errors or linac fabrication errors, this may lead to more serious emittance growth and beam losses.

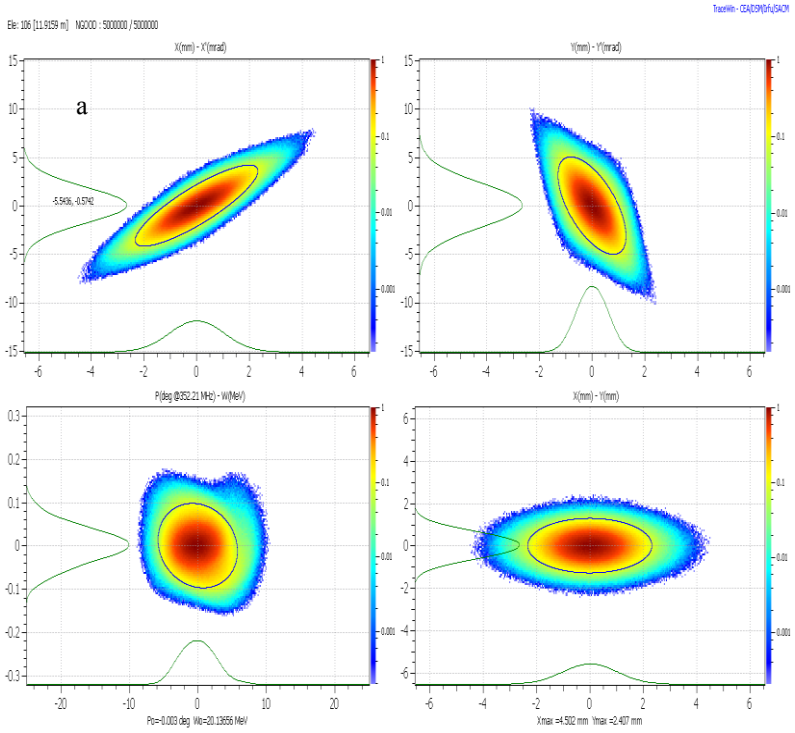
a
X(mm) - X'(mrad)
Y(mm) - Y'(mrad)
P(deg @352.21 MHz) - W(MeV)
X(mm) - Y(mm)
Po=0.003 deg Wo=20.13656 MeV
Xmax =4.502 mm Ymax =2.407 mm

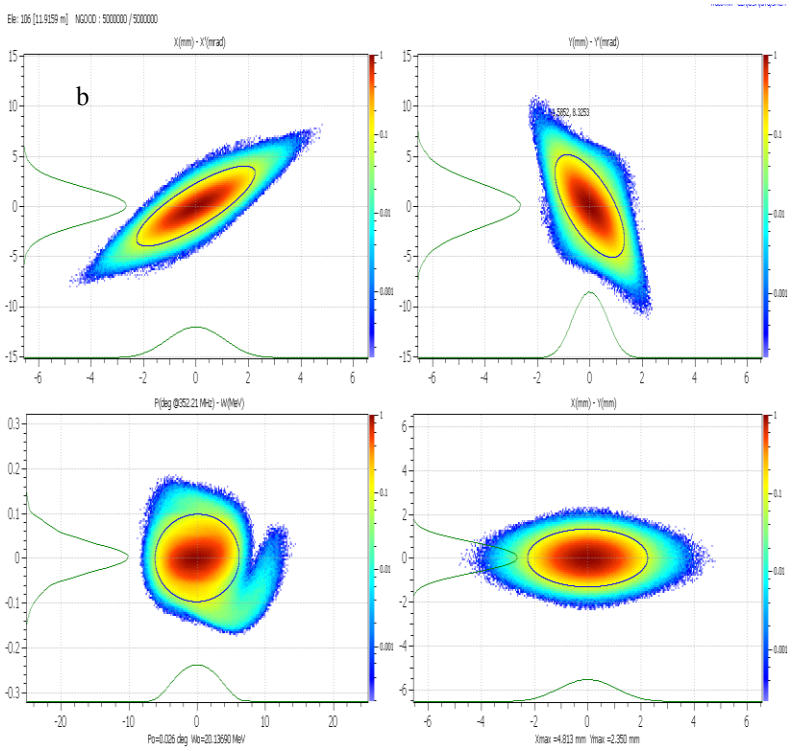
b
X(mm) - X'(mrad)
Y(mm) - Y'(mrad)
P(deg @352.21 MHz) - W(MeV)
X(mm) - Y(mm)
Po=0.026 deg Wo=20.13690 MeV
Xmax =4.813 mm Ymax =2.350 mm

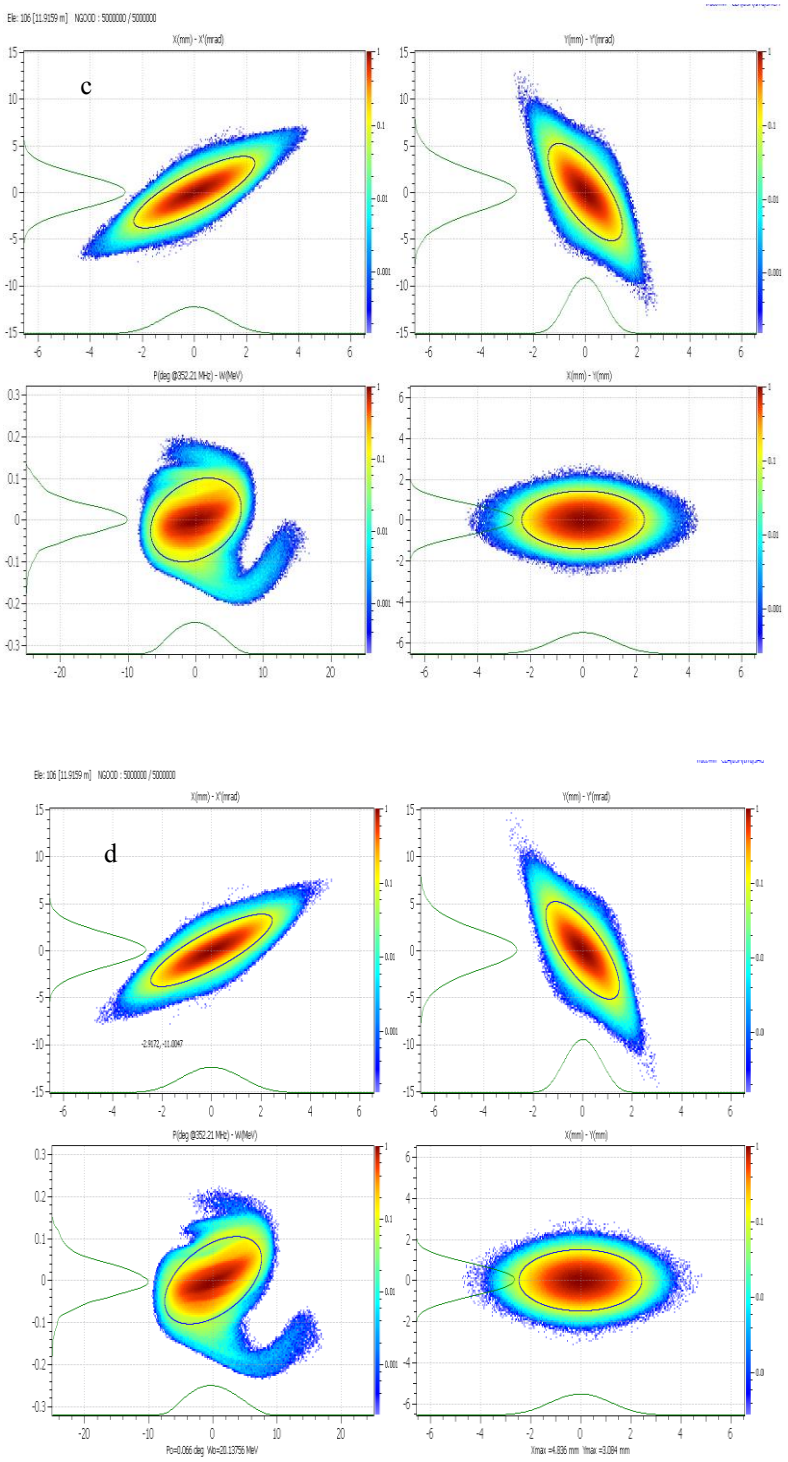

Figure 3.9. Beam distribution in x-x', y-y', ΔE-ΔΦ and x-y plane at the end of the linac (a) for 10 mA (b) 20 mA (c) 30 mA and (d) 40 mA beam.

Table 3.3. Emittance growth and RMS Beam sizes for different currents.

Beam Current (mA)	Transverse Emittance Growth		Longitudinal Emittance Growth		Maximum RMS Beam Size (cm)	
	Parmila	Tracewin	Parmila	Tracewin	Parmila	Tracewin
10	1.4 %	0.96 %	3.8 %	3.0 %	0.131	0.130
20	2.4 %	1.9 %	11.7 %	9.1 %	0.134	0.134
30	3.0 %	3.1 %	18.9 %	17.5 %	0.140	0.137
40	5.1 %	4.1 %	26.0 %	23.0 %	0.145	0.142

3.5 Error studies

In the design of DTL it is very important to study the effects of variation of parameters on the beam dynamics. Errors involved in the alignment of the beam handling components and quadrupole errors leading to beam misalignment and tilt can degrade the beam dynamics through reduced transmission and increased emittance. These studies are essential to get an idea of the errors that can be tolerated, which would in turn place limits on the tolerances needed for the fabrication of DTL, quadrupole magnets, RF components, etc. Further, a study of individual errors is not sufficient as a combination of these errors affect the dynamics of the beam differently. Therefore, a study of combined errors has also been carried out. For our studies, the acceptance criteria are 100 % transmission and less than 5 % increase in the normalized rms emittance for individual errors. The acceptable tolerance limits on each parameter is evaluated with these criteria and then the combined effect of all the errors has been studied.

3.5.1 Off-axis injection

If the beam is injected off-axis, that is, the beam axis is misaligned with respect to the DTL axis; there is a growth in emittance in transverse as well as longitudinal plane. This misalignment could be a result of an error in the transport line from the RFQ to the DTL, or from a misalignment of the DTL itself. The emittance growth due to beam misalignment is plotted in Fig. 3.10. It can be seen from the figure that the acceptance criterion of 5 % increase in emittance is met for misalignments of 0.5 mm or less. This implies that the beam transport line and the DTL should be aligned to better than 0.5 mm, which is not a stringent requirement.

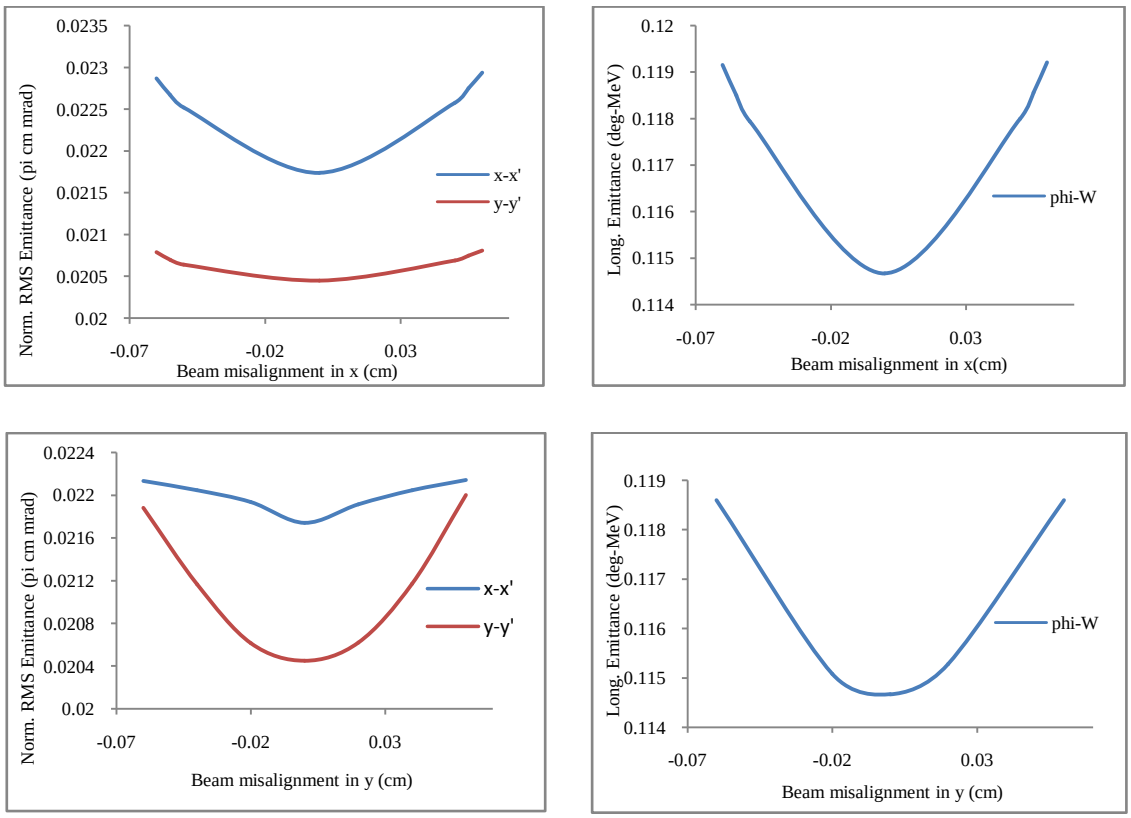

Fig.3.10. Effect of misalignments on the emittance of the beam at the end of DTL.

3.5.2 Beam Tilt

The effect of beam tilt with respect to the design DTL axis on the emittance in all three planes is plotted in Fig. 3.11. Beam tilt may arise due to an error in transport line or due to a tilt in the DTL itself. The acceptance criterion of 5 % emittance growth is met for a tilt of 3 mrad or less.

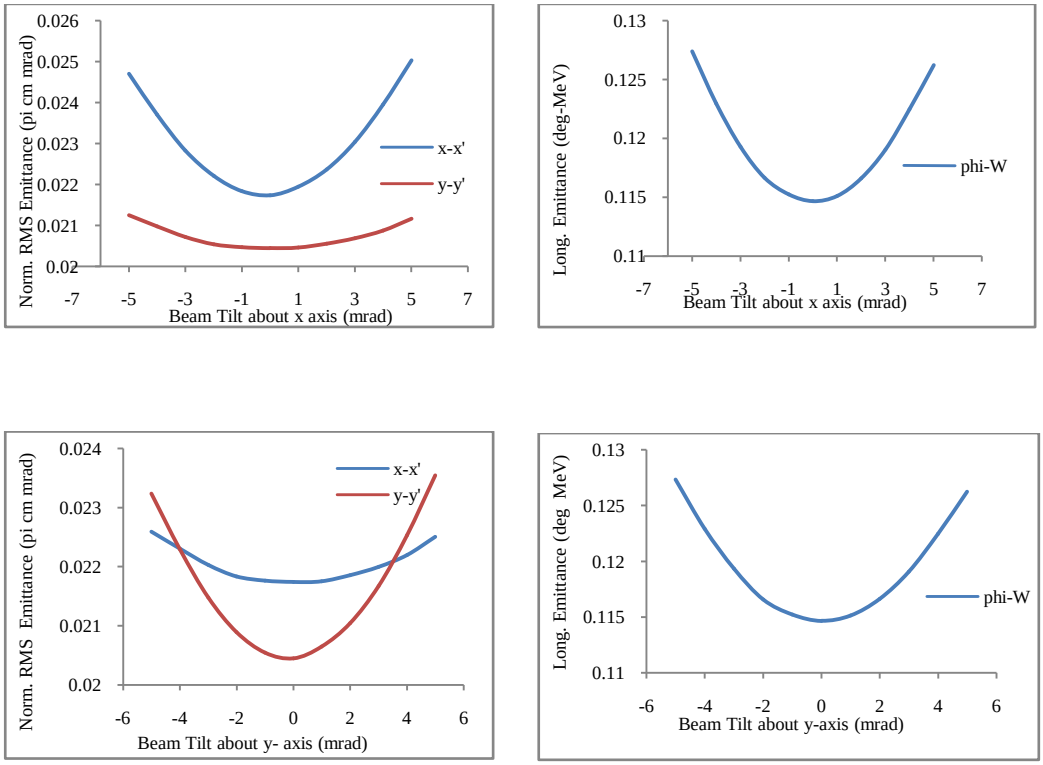

Fig. 3.11.Effect of Beam tilt on emittance at the end of DTL.

3.5.3 Quadrupole displacement

The emittance blow-up due to quadrupole displacement is plotted in Fig. 3.12. Such an error could arise due to an error in mounting the quadrupoles inside the drift tubes. It can be seen that if all the quadrupoles in the DTL are randomly displaced by 70 µm or less, along the x-axis the emittance increase is 5.5 % in x-x' plane, while the corresponding increase in y-y' plane is 1.4 % only. Similarly, a displacement by 55 µm

along the y-axis, leads to a 5.1 % increase in y emittance while the x emittance increase is 0.2 %. The longitudinal emittance grows by 4.6 % and 3.8 % respectively.

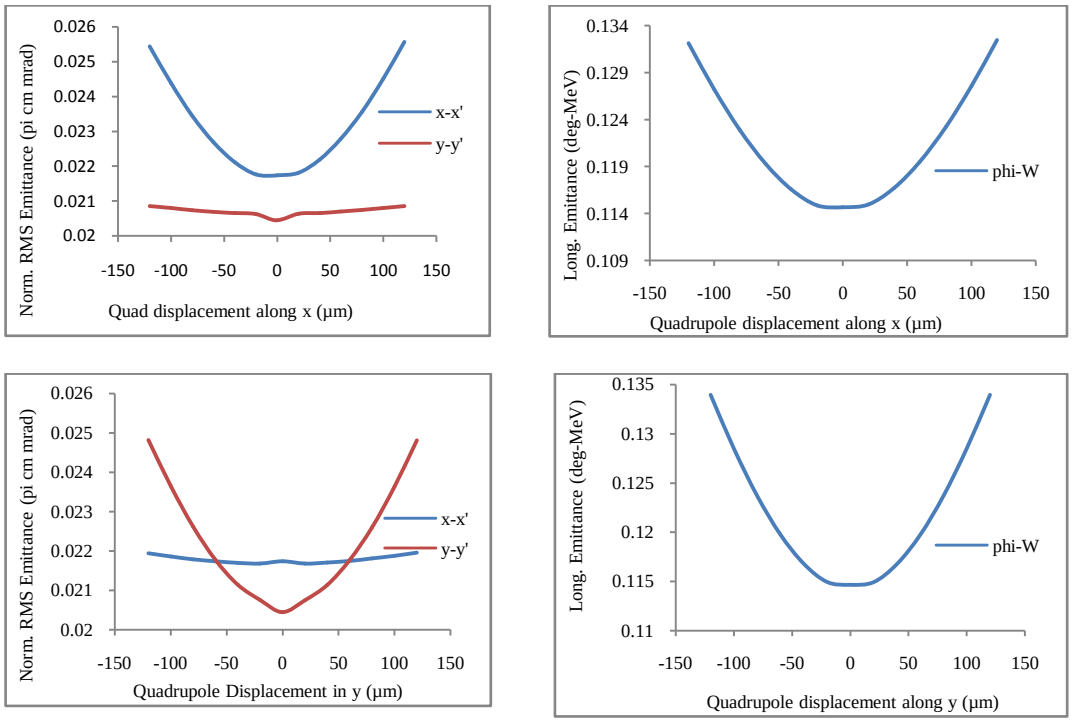

Fig. 3.12 . Effect of quadrupole displacement on emittance at the DTL end.

3.5.4 Quadrupole Tilt

The effect of quadrupole tilt on rms emittance is plotted in Fig. 3.13. A quadrupole tilt could arise due to a tilt in the quadrupole while mounting it inside the drift tube. If the quadrupoles are randomly tilted by 5 degrees or less about the x-axis, the rms emittance increases by 5.1 % in y-y' plane while the increase in emittance in x-x' plane is 0.2% only. A tilt of 3.5 degrees about the y-axis leads to an emittance increase of 4.9 % in x-x' plane and 1.2% in y-y' plane.

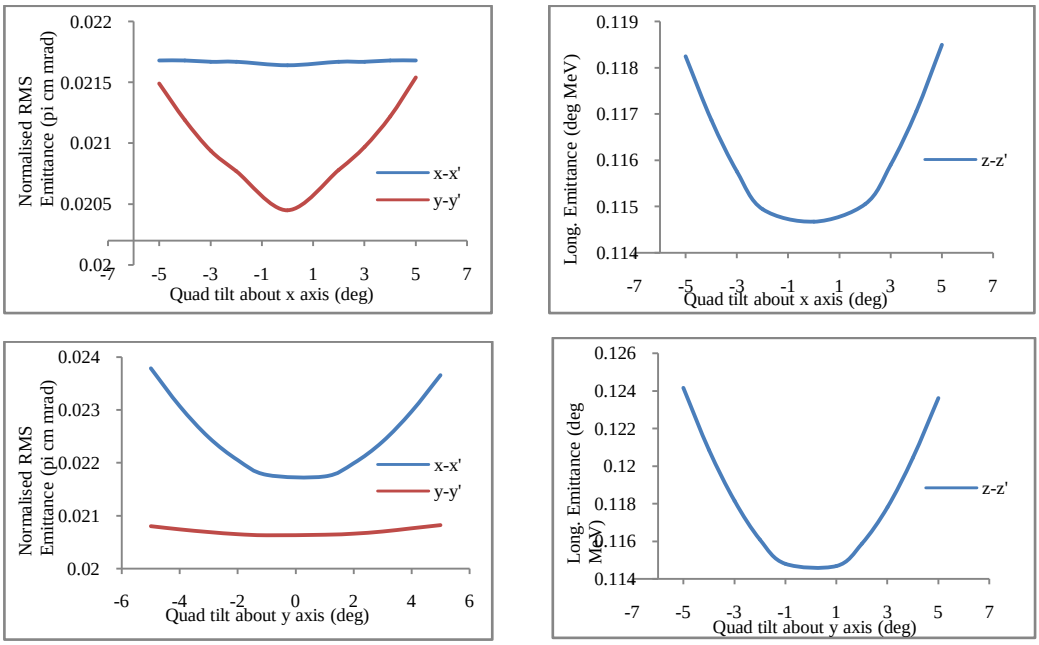

Fig. 3.13. Effect of quadrupole tilt on emittance at the DTL end.

A quadrupole roll error is a quadrupole rotation about z-axis. The effect of this error on the transverse emittance is plotted in Fig. 3.14. If the quadrupoles in the DTL are randomly tilted about z-axis by 0.6 degrees or less, the emittance growth is 4.5% in x-x' and 5.2% in y-y' planes respectively.

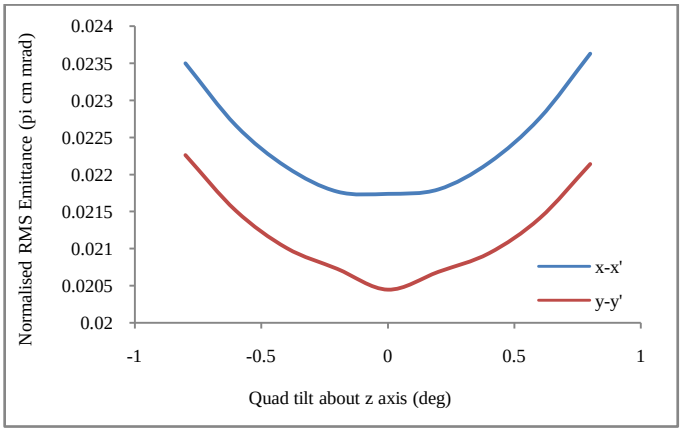

Fig. 3.14. Effect of quadrupole roll error on transverse emittance at the DTL end.

3.5.5 Quadrupole Field error

If the quadrupole field varies from its design value, there is an increase in transverse beam emittance as shown in Fig. 3.15. Such an error may arise due to an error in the quadrupole gradient or due to the inaccuracy in manufactured length of quadrupole. The emittance increases faster in y plane and it can be seen that for an error in quadrupole field of ± 2.5 %, the emittance increase is 4.8 % in y-y' plane while the emittance increases by only 1.1 % in x-x' plane.

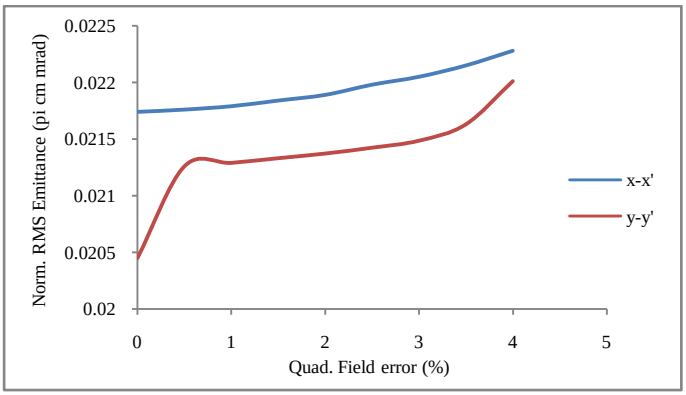

Fig. 3.15. Effect of quadrupole field error on transverse emittance at the DTL end.

3.5.6 RF amplitude error

RF amplitude error may arise due to an error at the RF source or due to reduced quality factor as compared to design value of the DTL cavity. The longitudinal dynamics of the beam is worst affected by this error. The effect of varying RF field amplitude on the beam emittance in the longitudinal plane is shown in Fig. 3.16. The transverse emittance is not affected by this error. An error in RF field amplitude of not more than 1% can be tolerated as this corresponds to an increase of 5 % in the longitudinal emittance.

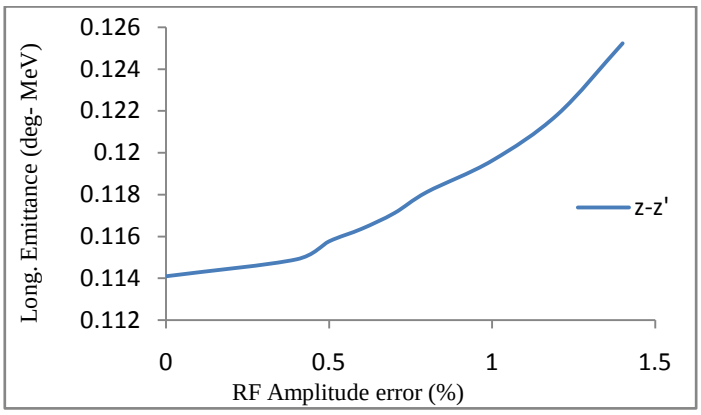

Fig. 3.16. Effect of RF amplitude error on longitudinal emittance at the DTL end.

3.5.7 RF Phase error

The RF phase error also causes a blow up of longitudinal emittance as can be seen in Fig. 3.17. This error may arise due to an error in RF transmission line. A variation of 1 degree in phase causes an emittance increase of 5 % in the longitudinal plane. There is no effect of RF phase error on the transverse emittance.

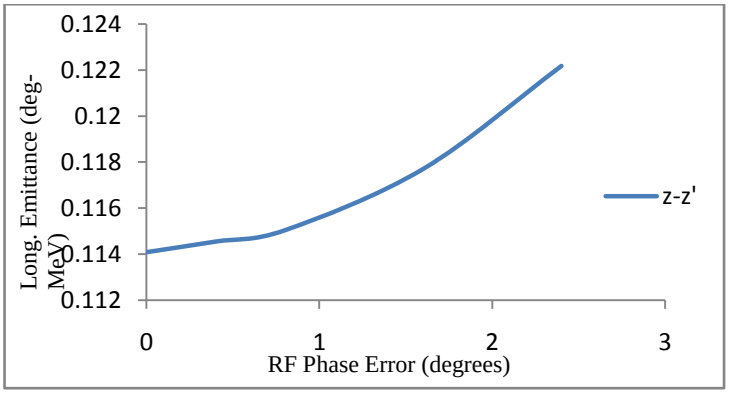

Fig. 3.17. Effect of RF Phase error on longitudinal emittance at the DTL end.

3.5.8 RF Field tilt

The emittance growth in the longitudinal plane as a function of RF field tilt in the DTL tank is plotted in Fig. 3.18. A field tilt refers to an end-to-end slope in the field amplitude. A field tilt may arise if the cell dimensions differ from the design value. A tilt

of ± 2 % leads to an emittance increase of 4.9 % in the longitudinal plane. Therefore, the RF field tilt within a tank of the DTL should not exceed ± 2 %.

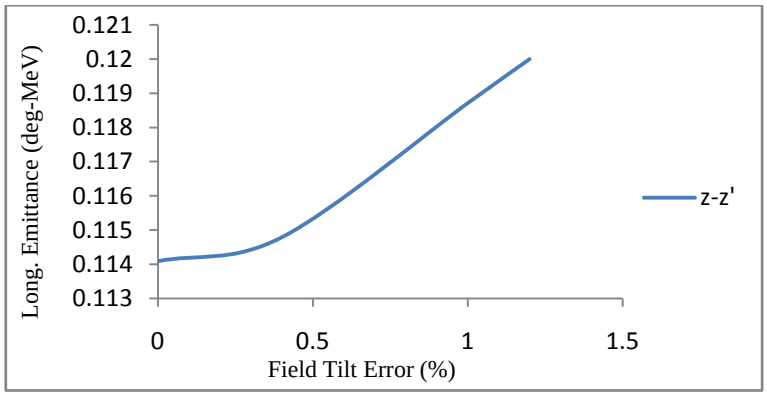

Fig. 3.18. Effect of RF field tilt error on longitudinal emittance at the DTL end.

A combined error study was done by giving all these errors together at their tolerance level. With the combined errors the emittance growth is 18 % in transverse plane and 21 % in longitudinal plane. There is no beam loss even in the combined presence of all the errors.

Chapter 4

Beam Halo Studies

Beam halos are of concern for the operation of proton linacs with intense beams, since they not only cause an increase in emittance, but also lead to beam loss and radio activation. As a rule of thumb, hands on maintenance is possible if the loss is less than 1 W/m [57]. The complete detail of the sources of beam loss and the halo dynamics is still not known.

The beam 'halo' consists of a small number of particles which oscillate around the bunch core. Various mechanisms can contribute to the development of a low-density particle halo which surrounds the core and eventually results in beam loss. The most prominent are: a) parametric 2:1 resonances between the oscillations of a mismatched beam core and the movements of single particles, b) envelope lattice resonances which occur between the beam envelopes and the elements of a periodic focusing structure, c) intra-beam scattering, and d) coherent space-charge coupling resonances. The envelope lattice resonances can yield rapid r.m.s. emittance growth and halo development but are easily avoided by keeping the zero-current phase advance per period in all three planes below 90º. Intra-beam scattering may be of importance in the Low-Energy Beam Transport (LEBT) section, where the ionization of gas in the beam pipe is used to compensate the high space-charge forces at low energy and is not important in high current ion accelerators [58]. The space charge coupling resonances [59] are responsible for emittance exchange between the transverse and the longitudinal plane of the beam but

they do not contribute to the development of beam halo. The parametric resonance has therefore been identified as the major source of halo production.

In order to calculate the beam evolution and the stability properties of beam particles, it is useful to work with the equations describing the rms beam envelopes [60]. For effects that go beyond the regular oscillations of the beam, one often uses the smoothed form of these equations, where one averages over the regular beam oscillations to study superimposed oscillations due to mismatch or other effects.

4.1. The matched beam

Simulations were done using TRACEWIN code to study the beam halo formation in the designed DTL for LEHIPA. The matched beam parameters at the input of the DTL was calculated. This matched beam was given as an input to the DTL. A large number of particles provide a high resolution in the outermost areas of phase space where the halo formation takes place and where the particle loss occurs on the beam pipe. Therefore, simulations were done with 5 million particles.

No particle loss was observed in any of the cases studied. Now, for high current, CW linacs, in order to avoid activation, the particle loss should not be more than 1 nA/m, at high energy. Taking this as a conservative upper limit even at low energy, for our DTL length of 11.92 m, this corresponds to an admissible current loss of 12 nA over the full length of the DTL. Since each macroparticle in our simulations corresponds to 6 nA current, the fact that there was no particle loss shows that the maximum current loss is obviously much below the permissible limit (12 nA).

The beam simulations were done with input 6D uniform and Gaussian beam distributions. For a uniform input beam, there is no significant increase in the beam

emittance. For a Gaussian input beam, the emittance increase is about 3 % in transverse plane and 19 % in longitudinal plane. The emittance increase in the case of Gaussian beam is due to the inherent non-linearity of the distribution and hence an associated free energy which causes the rise in beam temperature as it propagates through the DTL.The lower tune depression values in the longitudinal plane causes larger increase in the longitudinal plane than in the transverse plane. The output beam profile for uniform and Gaussian beams have been shown in Figs. 4.1 and 4.2. The uniform input beam evolves into distribution with rather sharp beam edge. The Gaussian beam, on the other hand already shows signs of halo particles at the periphery of the beam.

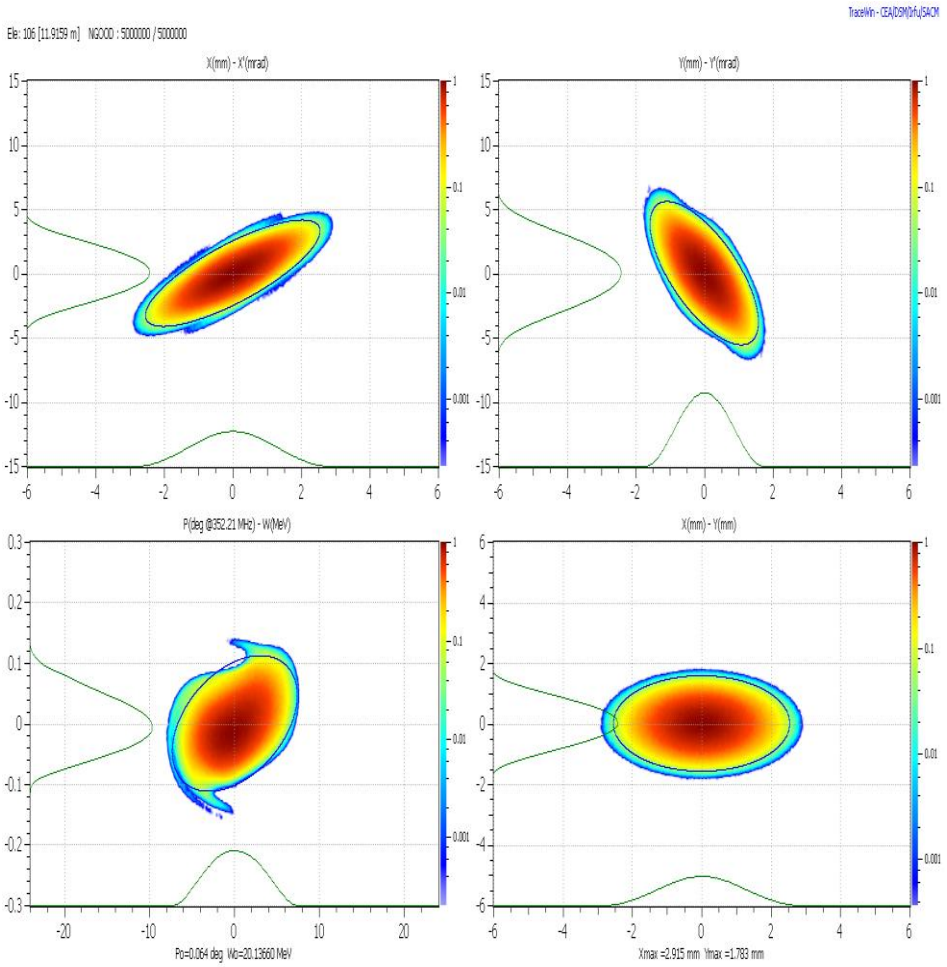

Fig.4.1. Beam at the output of the DTL with uniform distribution at the input to the DTL.

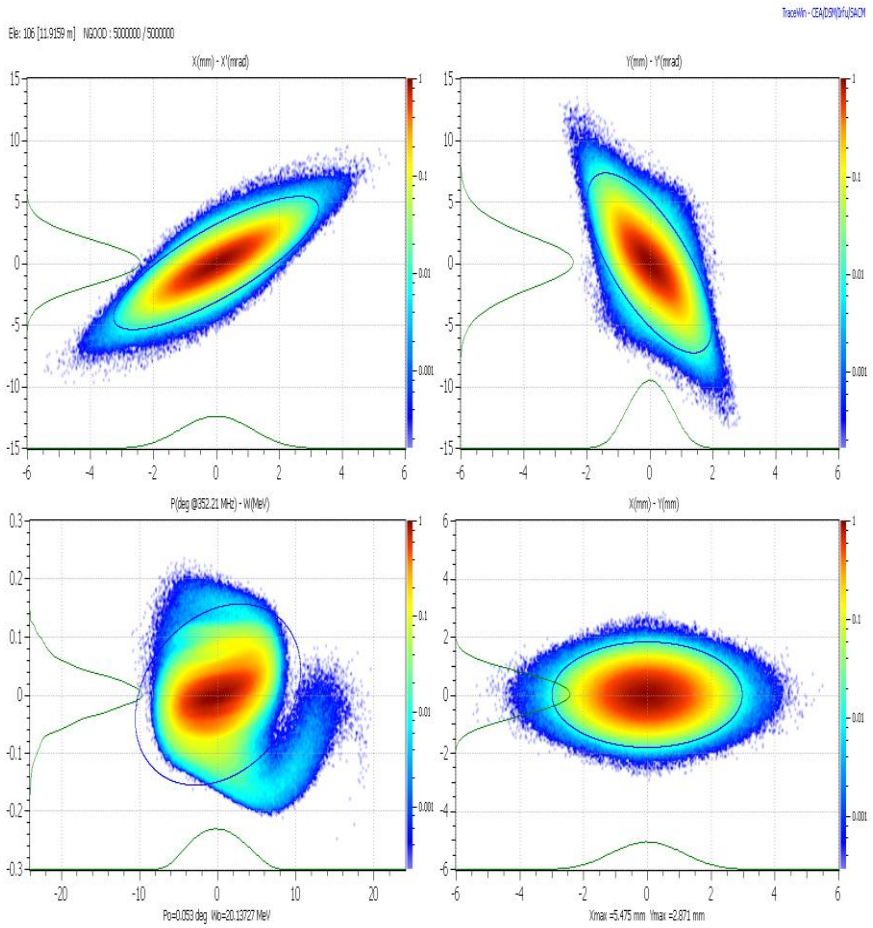

Fig.4.2. Beam at the output of the DTL with Gaussian distribution at the input to the DTL.

4.2. Initial Beam Mismatch

4.2.1. The Particle-core model

The three main forces acting on the beam are (1) the focusing quadrupoles (2) the RF gaps and the (3) internal space charge forces. The smoothed envelope equation [61] average over the oscillating beam envelope caused by these forces, provide relations for averaged envelope beam sizes. The envelope equation describing the rms quantities of all particles were first derived by Kapchinskiy and Vladimirskiy (KV) [62] for a continuous,

unbunched beam. An azimuthally symmetric continuous beam in a uniform focusing channel is described using the smooth approximation of these KV envelope equations

$$a_x'' + a_x\kappa_x(s) - \frac{\langle xF_{sc,x}(s)\rangle}{a_x} - \frac{{\varepsilon_x}^2}{a_x^3} = 0$$

$$a_y'' + a_y\kappa_y(s) - \frac{\langle y\,F_{sc,y}(s)\rangle}{a_y} - \frac{{\varepsilon_y}^2}{a_y^3} = 0$$

$$b'' + b\kappa_z(s) - \frac{\langle zF_{sc,z}(s)\rangle}{b} - \frac{{\varepsilon_z}^2}{b^3} = 0 \qquad (4.1)$$

where $a_i = \sqrt{\langle i^2\rangle}$, $b = \sqrt{\langle z^2\rangle}$, $F_{sc,x,y,z}$ are the space charge forces and $\varepsilon_{x,y,z}$ are the emittances in the x, y and z planes.

The transverse motion of beam halo particles is described by a particle-core model [63] which uses the space charge field of a continuous cylindrical oscillating beam core in a uniform linear focusing channel to provide the force that drives particle to large amplitudes. The model predicts the maximum amplitude for parametric beam resonance as a function of initial beam mismatch. In the matched case, the radius of the beam core as well as the amplitude of single particle oscillations are both constant. If the core is initially mismatched its radius starts to oscillate around its equilibrium value. The matched solution of the envelope equations oscillate with the periodicity of the focusing channels. The mismatched solution oscillates about the matched solution. The matched solutions are $\tilde{a}_{x,y}$ and $\tilde{b}$, then the mismatched solution can be represented as

$$a_{x,y}(s) = \tilde{a}_{x,y}(s) + \Delta a_{x,y}(s)$$
$$b(s) = \tilde{b}(s) + \Delta b(s) \qquad (4.2)$$

By inserting these equations into the envelope equations (4.1), one gets after some manipulations the three eigen modes for the 3D bunched beam in terms of the full current and zero current transverse and longitudinal phase advance (σ_t,σ_{t0},σ_l,σ_{l0}):

Quadrupole mode

$$\sigma_{env,Q} = 2\,\sigma_t \tag{4.3}$$

The eigen solutions are

$$\frac{\Delta a_x(s)}{\hat{a}} = A_m \cos\left(\sigma_{env,Q}.\frac{s}{L_p} + \phi\right)$$

$$\frac{\Delta a_y(s)}{\hat{a}} = -A_m \cos\left(\sigma_{env,Q}.\frac{s}{L_p} + \phi\right)$$

$$\frac{\Delta b_s}{b} = 0 \tag{4.4}$$

The quadrupolar mode consists of envelope oscillations of the transverse beam around their matched equilibrium with 180º phase difference between the planes. The longitudinal plane remains unaffected.

High Frequency mode, Breathing mode or Fast mode

$$\sigma_{env,H}{}^2 = \sigma_{t,0}^2 + \sigma_t^2 + \frac{1}{2}\sigma_{l,0}^2 + \frac{3}{2}\sigma_l^2 + \sqrt{\left(\sigma_{t,0}^2 + \sigma_t^2 - \frac{1}{2}\sigma_{l,0}^2 - \frac{3}{2}\sigma_l^2\right)^2 + 2(\sigma_{t,0}^2 - \sigma_t^2)(\sigma_{l,0}^2 - \sigma_l^2)} \tag{4.5}$$

The eigen solutions are

$$\frac{\Delta a_{x,y}(s)}{\hat{a}} = A_m \cos\left(\sigma_{env,H}.\frac{s}{L_p} + \phi\right)$$

$$\frac{\Delta b(s)}{\hat{b}} = \frac{A_m}{g_H}\cos\left(\sigma_{env,H}.\frac{s}{L_p} + \phi\right) \tag{4.6}$$

where the form factor $g_H > 0$

The fast mode "breathes" in all three planes with the same phase but with different amplitudes in transverse and longitudinal planes. The oscillation frequency is higher than the quadrupolar or slow modes.

Low frequency mode or Slow mode

$$\sigma_{env,L}{}^2 = \sigma_{t,0}^2 + \sigma_t^2 + \frac{1}{2}\sigma_{l,0}^2 + \frac{3}{2}\sigma_l^2 - \sqrt{\left(\sigma_{t,0}^2 + \sigma_t^2 - \frac{1}{2}\sigma_{l,0}^2 - \frac{3}{2}\sigma_l^2\right)^2 + 2(\sigma_{t,0}^2 - \sigma_t^2)(\sigma_{l,0}^2 - \sigma_l^2)} \quad (4.7)$$

The eigen solutions are

$$\frac{\Delta a_{x,y}(s)}{\hat{a}} = A_m \cos\left(\sigma_{env,L}.\frac{s}{L_p} + \phi\right)$$

$$\frac{\Delta b(s)}{\hat{b}} = \frac{A_m}{g_L}\cos\left(\sigma_{env,L}.\frac{s}{L_p} + \phi\right) \quad (4.8)$$

where the form factor $g_L < 0$

The slow mode has different amplitudes in the longitudinal and transverse planes. The longitudinal and transverse envelopes oscillate with a phase difference of 180º.

The form factors are defined as

$$g_{H,L} = \frac{\sigma_{t,0}^2 - \sigma_t^2}{\sigma_{env,H,L}^2 - 2(\sigma_{t,0}^2 + \sigma_t^2)} \quad (4.9)$$

A_m is the mismatch amplitude and $\hat{a}\ and\ \hat{b}$ are the matched beam envelopes in the smooth approximation.

4.2.2. Excitation of mismatch modes

Using the eigen solutions (equations 4.4, 4.6, 4.8) and the form factors (4.9), the three eigen modes were excited [64] with the following mismatches

Quadrupolar mode: $\frac{\Delta a_x}{a} = -\frac{\Delta a_y}{a}\ and\ \frac{\Delta b}{b} = 0$

Fast mode: $\frac{\Delta a_x}{a} = \frac{\Delta a_y}{a} = g_H\frac{\Delta b}{b}$

Slow mode: $$\frac{\Delta a_x}{a} = \frac{\Delta a_y}{a} = g_L \frac{\Delta b}{b}$$

The mismatched beam was then given as an input to the FFDD lattice of the LEHIPA DTL. The beam dynamics simulations were done with uniform and Gaussian beam distributions in 6D ellipse. The oscillations of the beam radius for uniform input beam distribution are shown in Fig. 4.3.

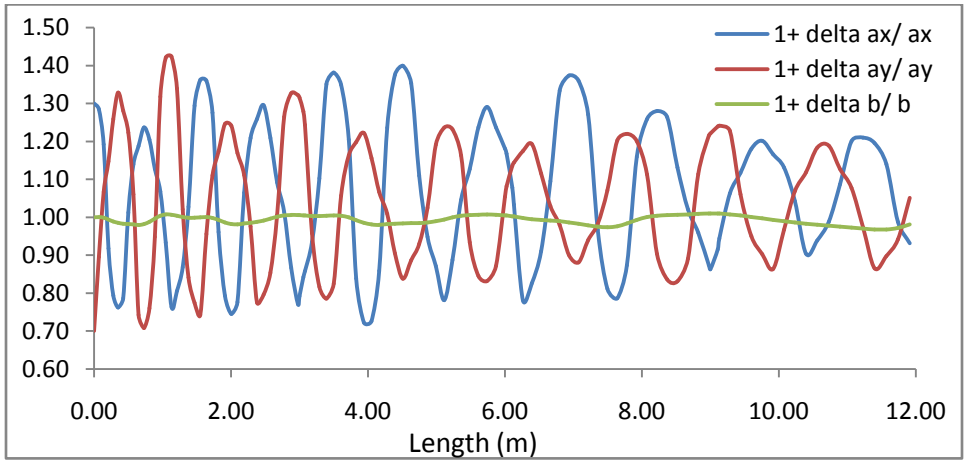

Fig. 4.3 (a). 30 % quadrupole mode excitation with uniform input beam distribution.

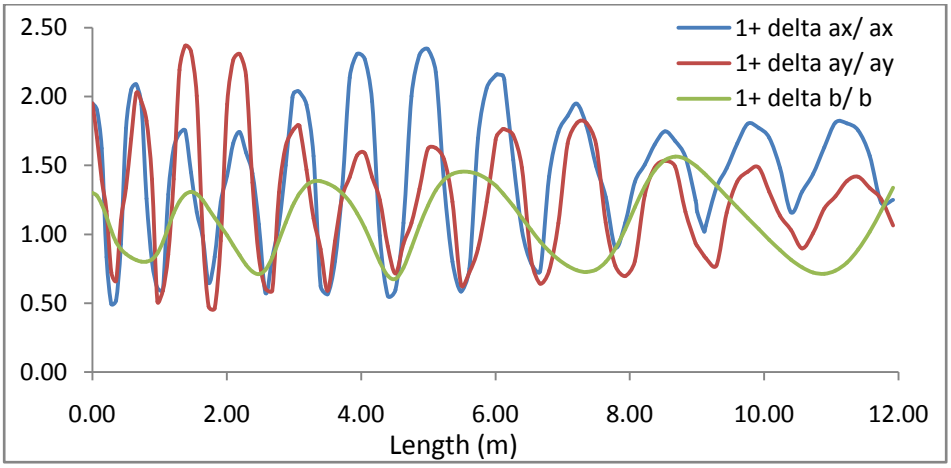

Fig. 4.3 (b). 30 % fast mode excitation with uniform input beam distribution.

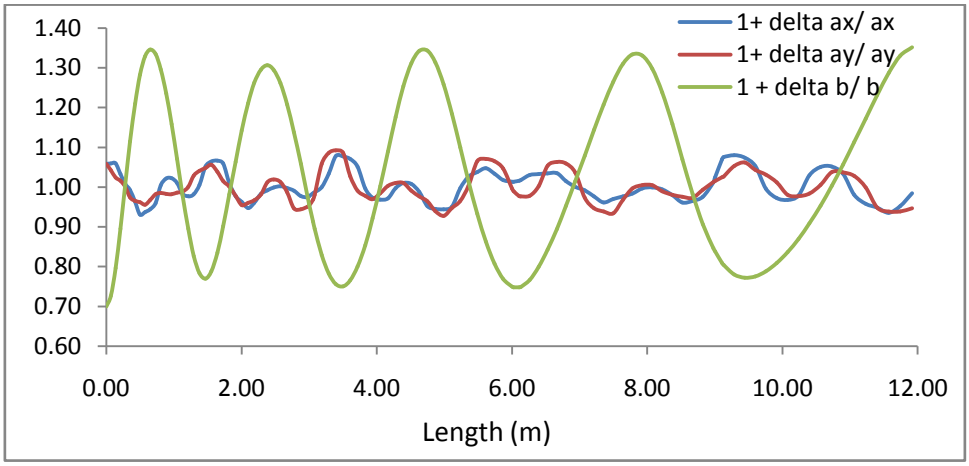

Fig. 4.3 (c). 30 % slow mode excitation with uniform input beam distribution.

It can be seen from the Fig. 4.3 (a) that for the case of quadrupolar mode the oscillations in x and y planes are opposite in phase. The longitudinal plane remains almost unchanged. The oscillations carry on almost unchanged over the entire length of the DTL. The oscillation period length increases because the phase advance per metre decreases with increasing energy along the length of the linac. In the case of fast and slow modes (Fig. 4.3 (b&c)), the x and y amplitudes and phase are both equal. The longitudinal oscillations have different amplitude for both the fast and slow modes. The longitudinal oscillations in fast mode are in the same phase as the transverse oscillation while they are in opposite phase for the slow mode. Again, despite the imperfection (varying amplitudes), the oscillation carries on without much damping over the linac. The output beam in x-x', y-y' and z-z' for the three modes are shown in Fig. 4.4 (a), (b) and (c). Fig. 4.4 (a) shows the formation of a distinct beam filamentation in x-x' and y-y' planes for quadrupole mode excitation. The x-y plane shows the formation of the low density halo. Fig. 4.4 (b) shows the output beam for the fast mode excitation. All three phase space planes show, seriously distorted beam. For the slow mode (Fig. 4.4 (b)), the

transverse phase space is not much affected. This is expected since the transverse oscillations are insignificant for this mode as plotted in Fig. 4.3(c).

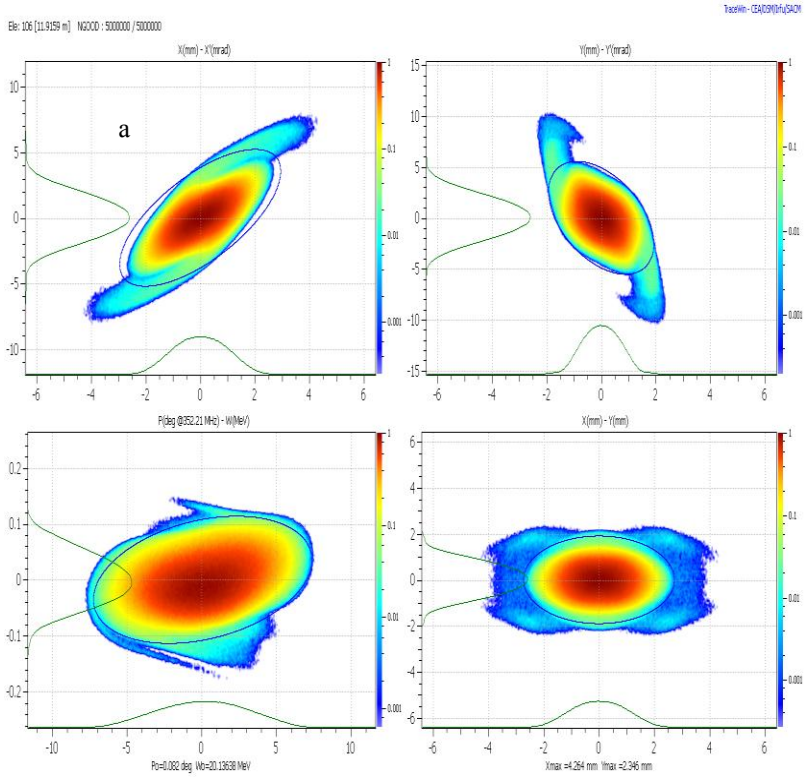

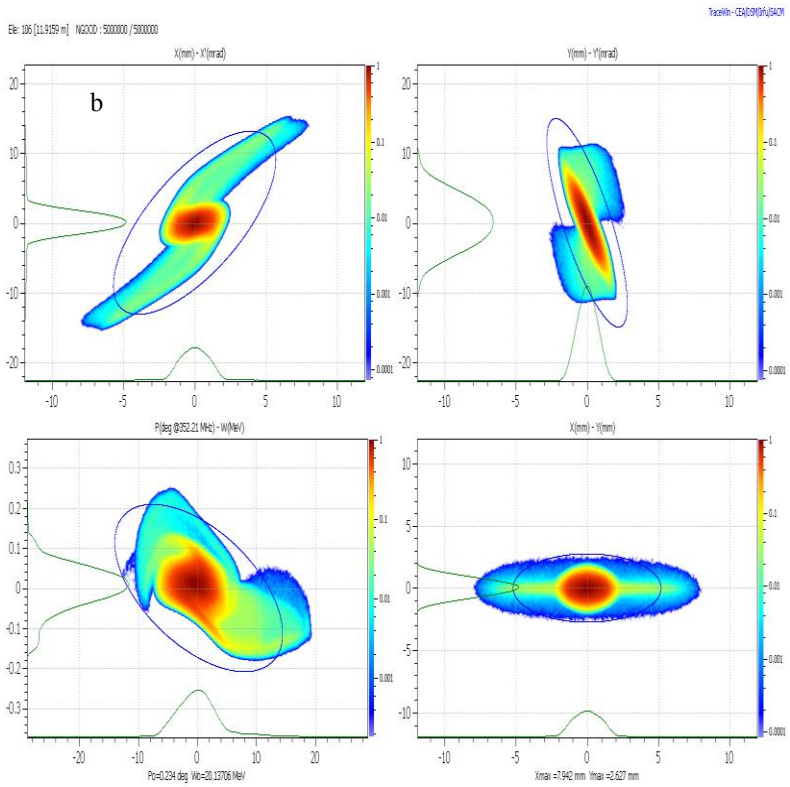

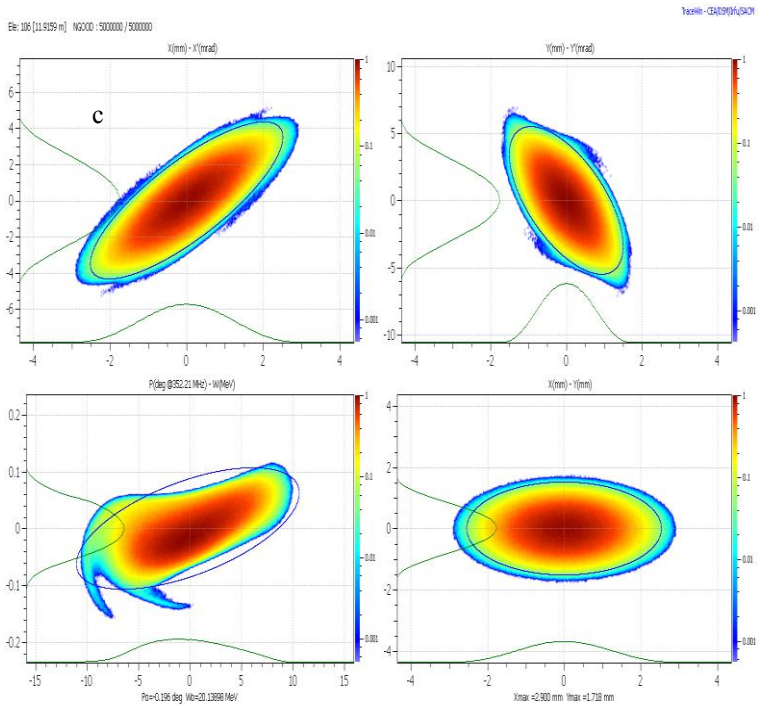

Fig. 4.4. The output beam with input uniform beam for (a) quadrupole mode(b) fast mode and (c) slow mode.

The oscillations for the three modes with Gaussian input beam distribution is plotted in Fig. 4.5. Again the amplitudes and phases of oscillations in all three planes follow the predictions of the Particle-core model. The main difference between Fig. 4.3 and Fig. 4.5 is that the oscillations are damped as the beam traverses through the 11.92 m length of the linac. The damping is very significant for the quadrupole and fast mode oscillations. The slow mode oscillations show a relatively slower damping. The damping signifies the transformation of free energy that has been introduced into the system to emittance growth. In the case of uniform beam, the damping time constant is very large and therefore over the 26 periods of the DTL lattice, the damping process does not start. The space charge non-linearity inherent to the Gaussian beam combined together with the

mismatch beam, leads to a faster damping as shown in Fig. 4.5. The output beam from the DTL is shown in Fig. 4.6.

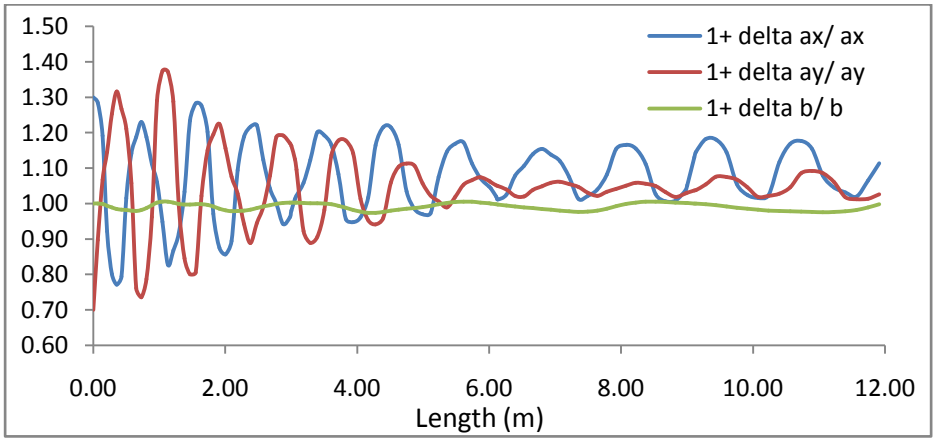

Fig. 4.5 (a). 30 % quadrupole mode excitation with Gaussian input beam distribution.

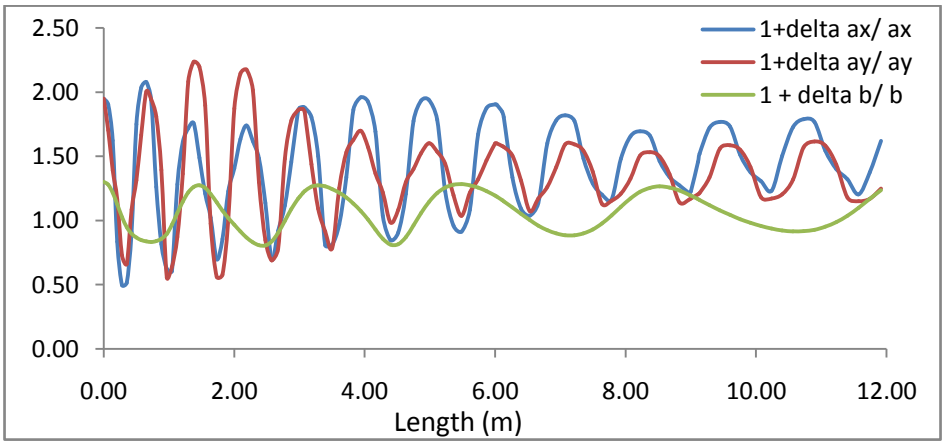

Fig. 4.5 (b). 30 % fast mode excitation with Gaussian input beam distribution.

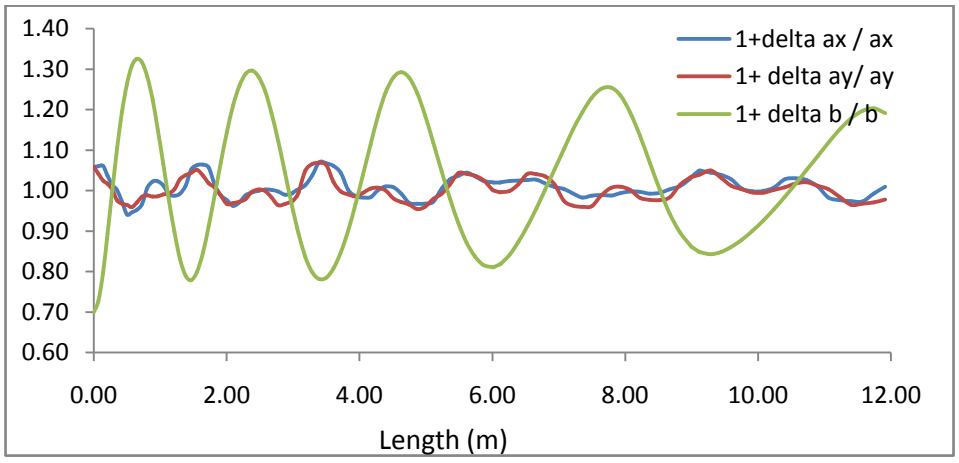

Fig. 4.5 (c). 30 % slow mode excitation with Gaussian input beam distribution.

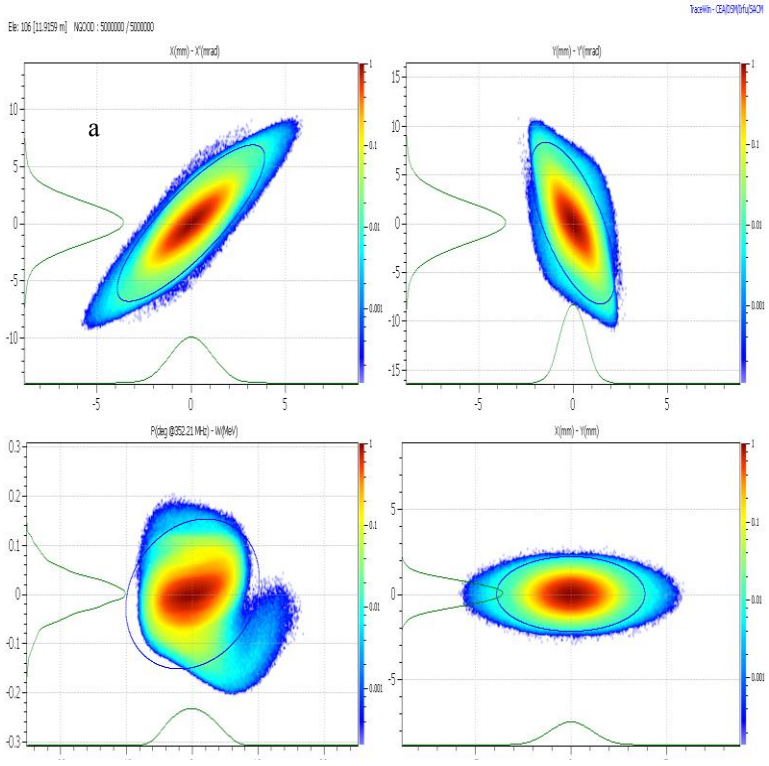
a

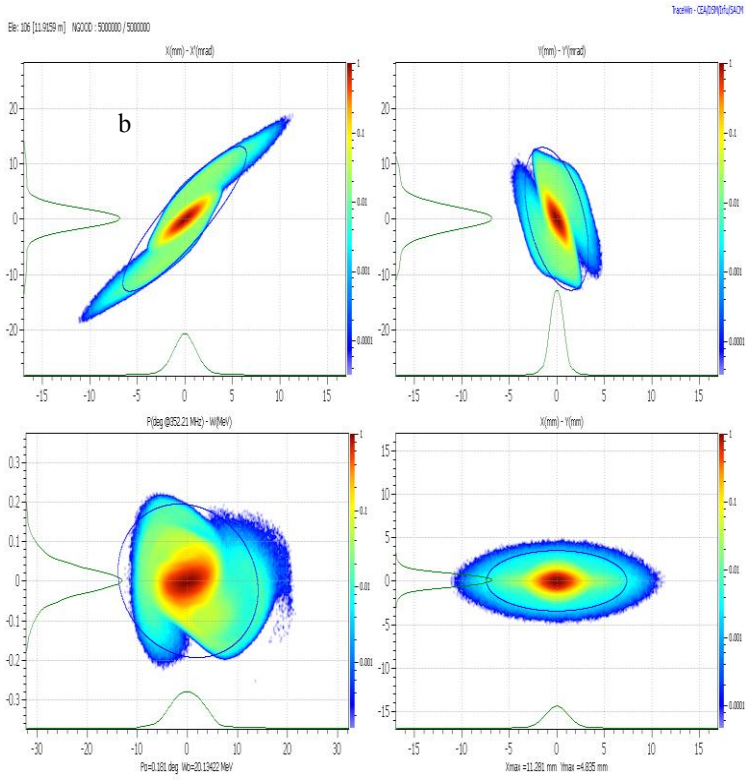
b

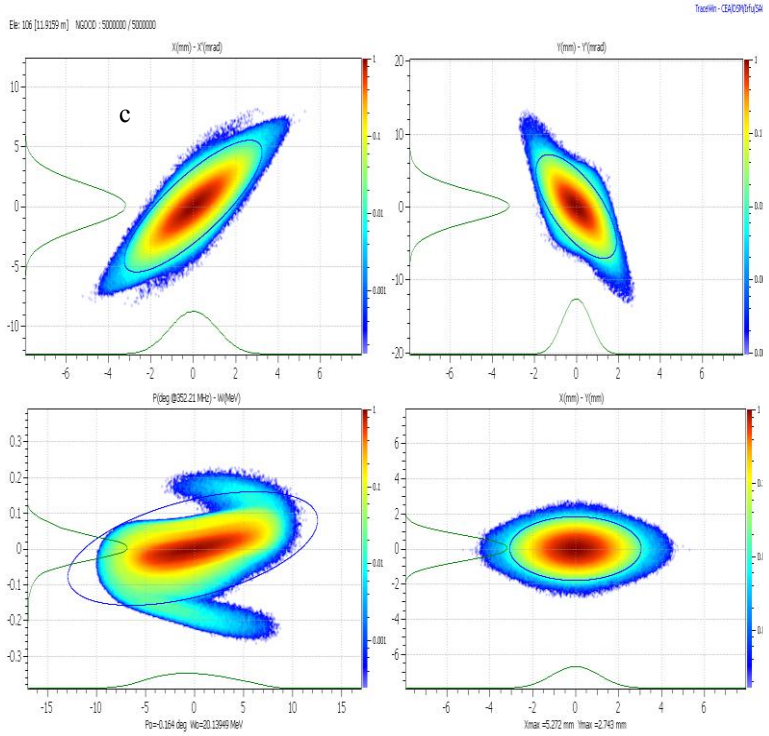

Fig. 4.6. The output beam with input Gaussian beam for (a) quadrupole mode (b) fast mode and (c) slow mode.

Table 4.1. Emittance increase due to the excitation of various modes.

Mode	Emittance increase in transverse plane		Emittance increase in z-z' plane	
	Uniform	Gaussian	Uniform	Gaussian
Quadrupole mode	13%	22%	2.2%	2.5%
Fast mode	45%	98%	58%	46%
Slow mode	0.6%	2%	5.3%	6.8%

The emittance increase for the three eigen modes for both the input distribution are given in Table 4.1. As expected, the emittance increase is more for input Gaussian beam. The fast mode shows maximum emittance since the excitation of 30 % longitudinal mismatch requires very high transverse mismatch value ~ 95 %, because of the large value of form factor for this mode. The slow mode, on the other hand requires

very small mismatch in transverse plane for 30 % longitudinal mismatch. Therefore, the beam property degradation is lesser in this case.

4.2.2.1. Maximum halo extent

The beam distribution in the transverse and longitudinal planes has been plotted in Fig. 4.7 for a uniform distribution at the DTL input. The distributions show distinct halo for all modes in both transverse planes. The matched beam does not show any halo and the halo arising for the three modes can completely be attributed to the mismatch. In x plane, the maximum halo extent is 6.6 times the rms beam size for the fast mode and 4.3 times the rms beam size for the quadrupole and slow mode mismatch. The halo in the y plane is between 3.5 to 4.2 times the rms size. In longitudinal plane there is no effect for the quadrupole mode. The slow mode shows a minimal asymmetric halo. The fast mode however shows a highly asymmetric distribution (also clear from Fig.4.4 b). The maximum extent of the longitudinal halo is 5 times the rms beam size.

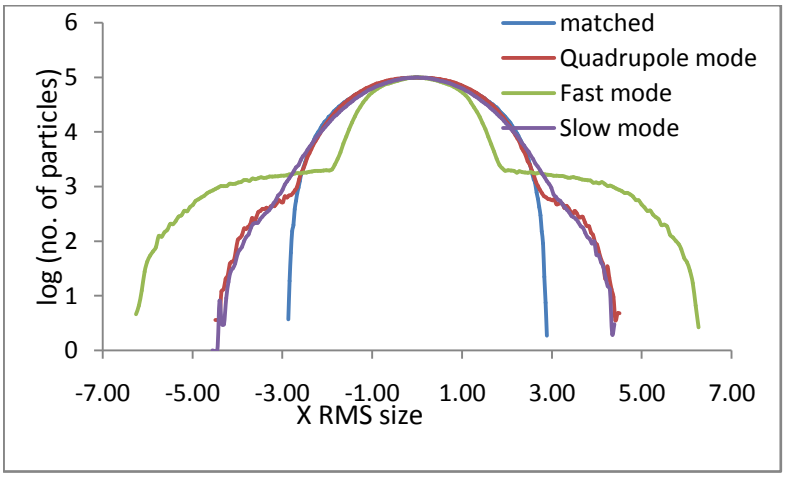

Fig. 4.7 a. Beam output distribution in x.

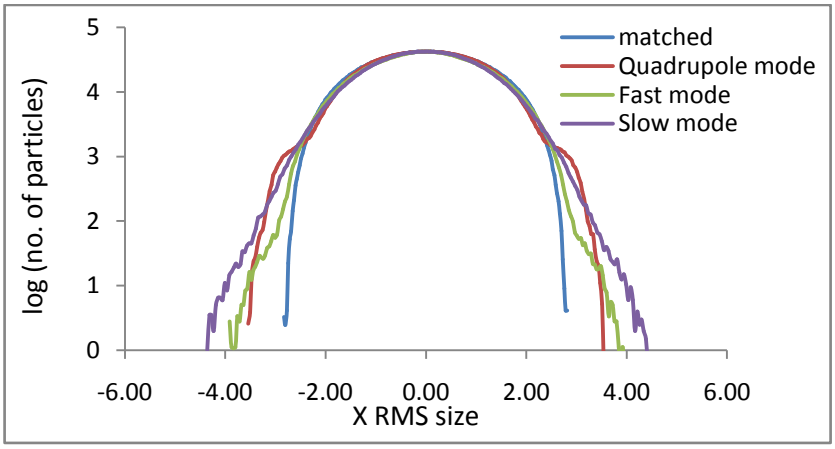

Fig. 4.7 b. Beam output distribution in y.

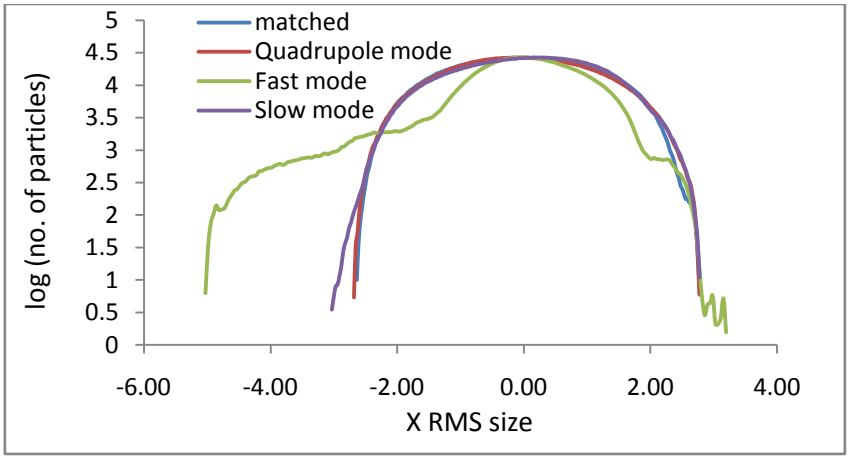

Fig. 4.7 c. Beam output distribution in z.

4.3. Some Halo Definitions

The particle-core model gives a useful insight of halo formation mechanism. It is now necessary to quantify the halo for a better understanding of the growth of halos in accelerators. There is no clearly defined separation between the halo and the main core of the beam. Therefore, there has been some difficulty identifying a suitable quantitative

measure of the halo content of a beam in a model independent way. Many attempts have been made to attribute a quantitative definition to beam halo.

Halo is a collection of particles of any origin or behaviour which lie in the low density region of the beam distribution 'far' away from the core. 'Far' is very often quantified by 'nσ', where n may be 3 to 5, depending on the distribution and halo mechanism

It is for example the ratio of beam sizes

$$\frac{mrms}{nrms}; \tag{4.10}$$

with m being generally 1 and n between 3 or 5.

Another definition considers the emittance ratio

$$\frac{Emittance\ \ (x)}{RMS\ Emittance}; \tag{4.11}$$

where x can be between 90% and 100% of the distribution. Both the definition (4.10) and (4.11) are model dependent. A step ahead was to define a halo parameter, as the ratio of nth moments of distribution

$$\frac{4th\ moment}{2nd\ moment} \tag{4.12}$$

This definition was first suggested by Wangler and Crandall [65] for a 1-D geometrical space and then extended to a 2-D phase space by Allen and Wangler [66]. The halo parameter thus defined is an invariant of motion under the presence of linear forces since the second and fourth moments are themselves kinematic invariants.

The halo intensity parameter in the i^{th} phase plane, given by Allen and Wangler is defined as

$$H_i = \frac{\sqrt{3I_4^i}}{2I_2^i} - 2 = \frac{\sqrt{3\langle q_i^4\rangle\langle p_i^4\rangle + 9\langle q_i^2 p_i^2\rangle^2 - 12\langle q_i p_i^3\rangle\langle q_i^3 p_i\rangle}}{2\langle q_i^2\rangle\langle p_i^2\rangle - 2\langle q_i p_i\rangle^2} - 2 \tag{4.13}$$

I_2^i and I_4^i are the second and fourth moments of particle distribution and are adiabatic invariants of motion. $H_i = 0$ for a KV distribution and $H_i = 1$ for a Gaussian distribution. This definition gives a dynamical point of view and provides a more reliable characterization of the halo as an intrinsic property of the beam.

Another halo definition suggested by P. A. P. Nghiem, et. al. [67] is based on the visual observation of the beam where the core part or the halo part can be clearly identified and only a clear border between the two remains to be determined. This definition is model independent and is capable to treat any definition type. They consider a "gas" of particles with non-zero and variable density gradients. The border between the core and halo is suggested at the location where the gradient variation is the steepest. Once the border between the core and halo is determined, the halo part is quantified by the percentage halo size and percentage halo particles in the following manner.

$$PHS = 100\ \frac{Halo\ Size}{Total\ Beam\ Size} \tag{4.14}$$

$$PHP = 100\ \frac{No.\ of\ particles\ \ in\ the\ Halo}{Total\ \ No.\ of\ particles} \tag{4.15}$$

These definitions of the halo can offer concrete numbers for characterizing the halo at a given position and its evolution along the acceleration structure. They also show very clearly the place of the halo within the beam.

4.3.1. Quantifying beam halo in the DTL

The code Tracewin was used to study the evolution of halo in the DTL. The halo parameter along the DTL has been shown in Fig. 4.8 for the three modes. The red, blue and green curves represent the halo parameter in x, y and z. One can see that the longitudinal halo parameter is unaffected for a quadrupole mode, while the transverse

halo shows a steady rise. The halo parameters increase more rapidly for fast mode. The transverse halo parameter grows to ~ 3 and the longitudinal halo parameter grows to 2 at the end of DTL. In the case of slow mode, there is no halo in the transverse plane. The longitudinal halo growth is also quite less and the halo parameter is 0.62 at the end of the DTL.

The percentage of halo particles and the percentage of halo size have been plotted in Figs. 4.9 and 4.10 for the three eigen modes in x, y and z plane.

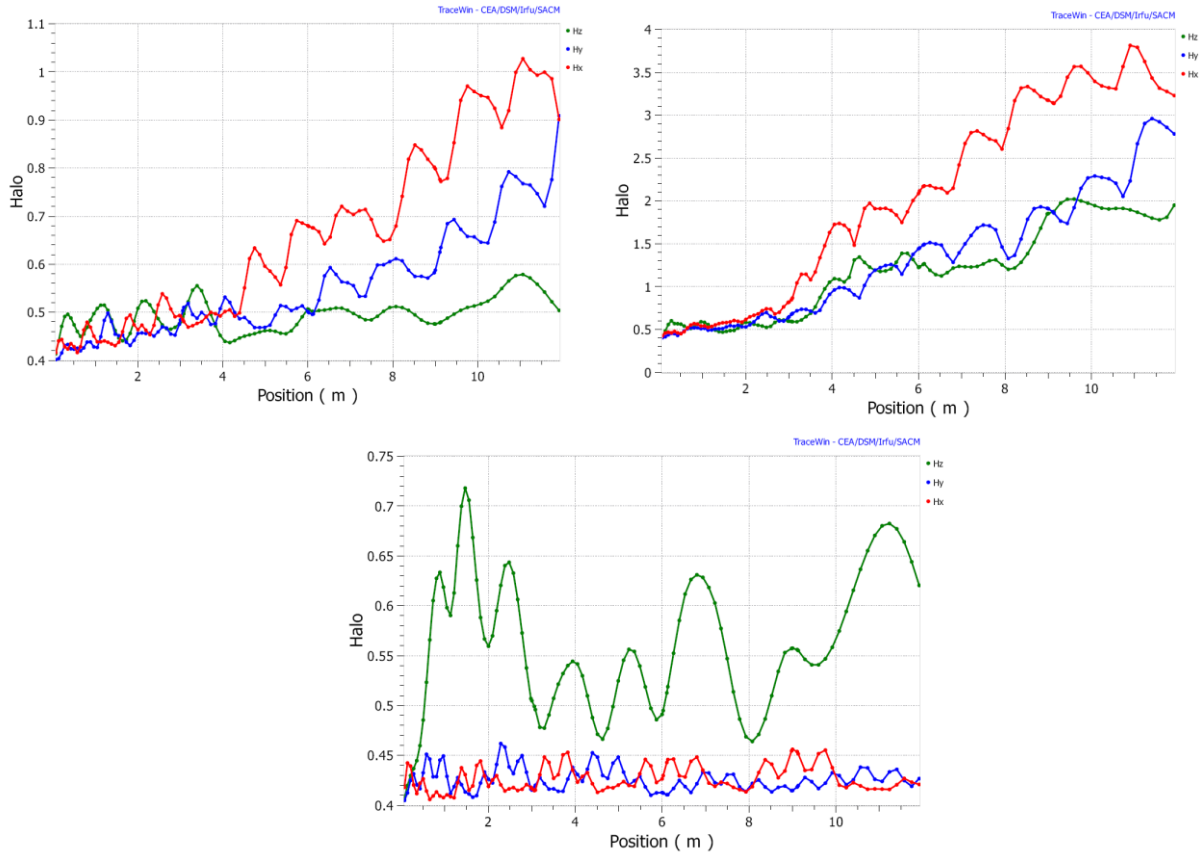

Fig. 4.8. Halo Parameter along the length of the DTL.

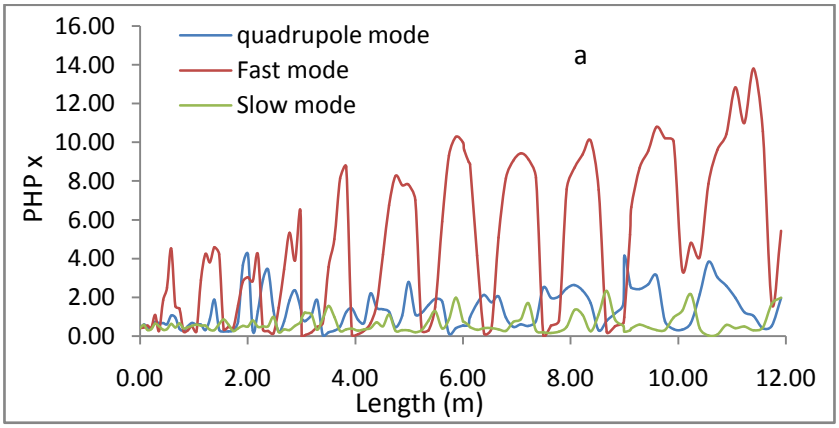

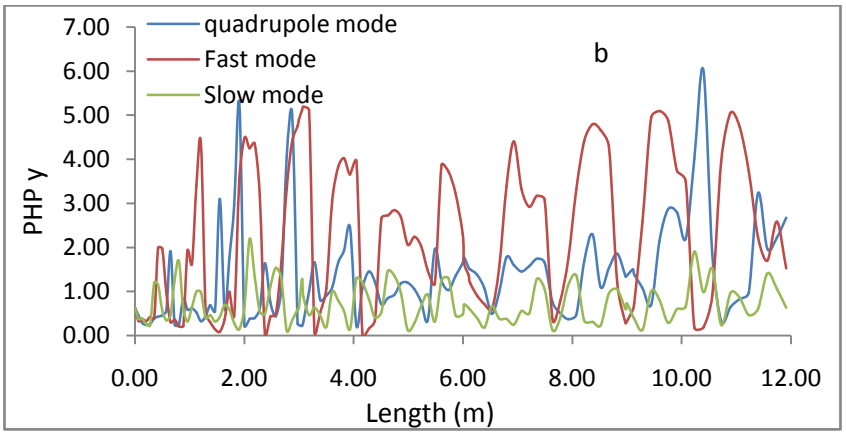

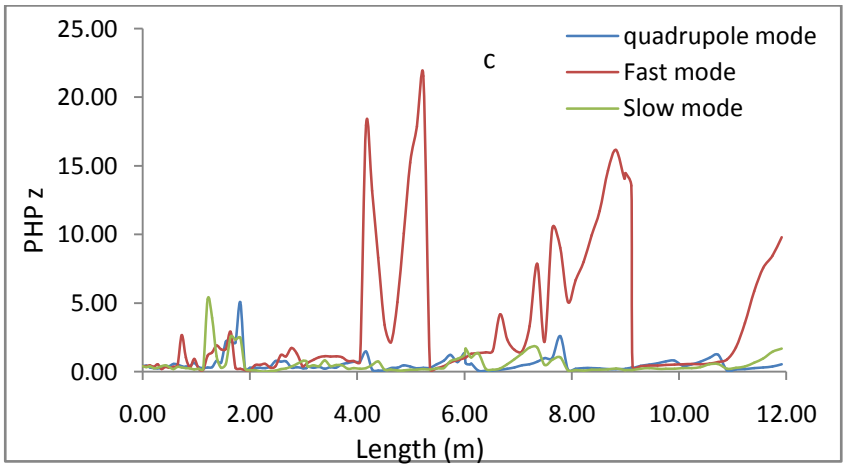

Fig. 4.9. Percentage of halo particles in (a) x (b) y (c) z.

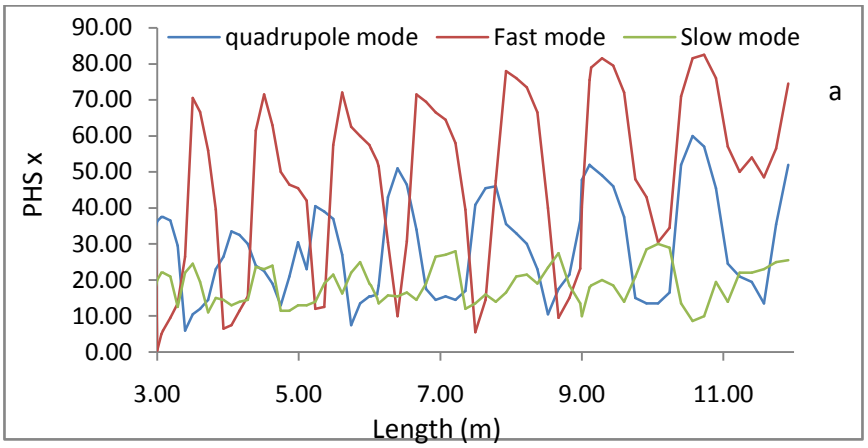

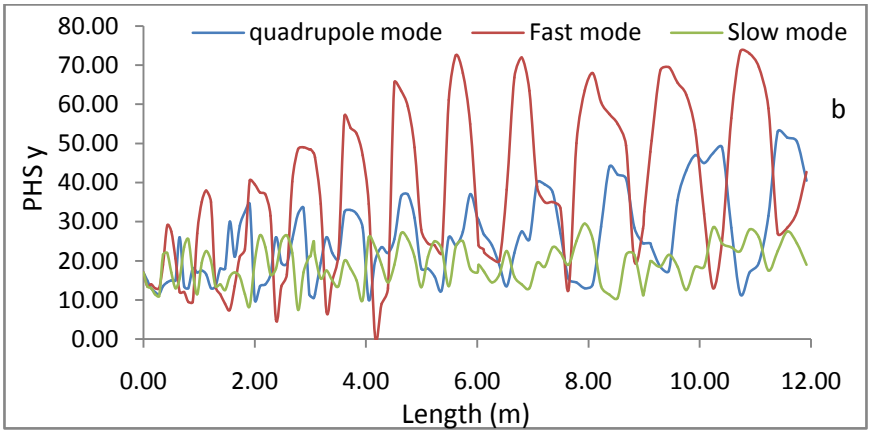

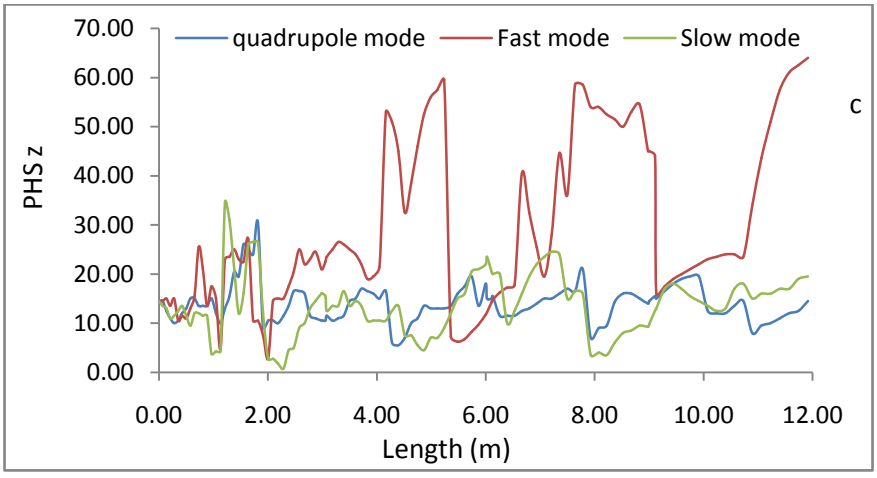

Fig.4.10. Percentage of halo size in (a) x (b) y and (c) z.

Figs. 4.9 and 4.10 show that the percentage of halo particles and the percentage of halo size is maximum for the fast mode in all the three planes. For quadrupole mode, the PHP grows to 2- 4 % and PHS grows to 10-30 % in the transverse plane. The longitudinal PHP and PHS values remain unaffected. For the slow mode, both the PHP and PHS show insignificant variation as the beam traverses through the DTL.

4.4. Excitation of general mismatch

All the studies done so far are for a mismatch excitation of a pure eigen mode. However, in a real linac it is more common to have some arbitrary mismatch which will yield a superposition of the three modes. It is therefore important to study the evolution of halos through the linac and the redistribution patterns of the beam distribution by exciting general mismatch also. As an example, one can excite a + + + or a + - + mismatch; the first case is a mismatch with same phase in all three planes and the second one is a mismatch with phase in y plane opposite of that in x and z planes. For a + + + mismatch, with arbitrary amplitudes, a mixture of slow and fast mode is excited, while a + - + mismatch excites a mixture of all three modes, with a dominant quadrupole mode. The halo evolution for these two cases is discussed here.

Same mismatch was given in x, y and z planes. The degree of mismatch was varied from 10 % to 40 %. The beam distribution with and without mismatch is plotted in Fig 4.11 and 4.12 for the two mismatch cases. It can be seen from the beam distribution that for the case of + + + mismatch, the halo is not very significant in the transverse plane even with 40 % mismatch. However, the longitudinal halo starts forming with 10 % mismatch and increases with the increasing degree of mismatch. The + + + mismatch has components of fast and slow mode only. As pointed out earlier, the excitation of fast

mode with a given mismatch in longitudinal plane, requires very high mismatches in the transverse plane. With the maximum mismatch in present studies of up to 40 %, the + + + mode seems to be more dominated by the slow mode. As seen earlier, the halo in the slow mode is the minimum. This is the reason why, the halo is very less in transverse plane, which is not affected by slow mode and slightly more in longitudinal plane. The halo parameter and PHP and PHS values are indicated in Table 4.2 for both + + + mismatch and + - + mismatch. The halo parameter increases with increasing mismatch and is higher in the longitudinal plane. The percentage of halo particles and the percentage of halo size also increase with increasing mismatch.

For a + - + mismatch, on the other hand, the halo is significant in transverse plane also. The longitudinal halo is still higher than the transverse one and the halo parameter in the longitudinal plane is similar to the + + + mismatch case. The transverse halo parameter and PHP and PHS are higher than that for + + + mismatch and these values increase significantly even for the transverse plane with increasing mismatch. In + - + mismatch, all the three modes are excited, and it is clear that the presence of quadrupole mode causes the difference in the transverse plane in this case.

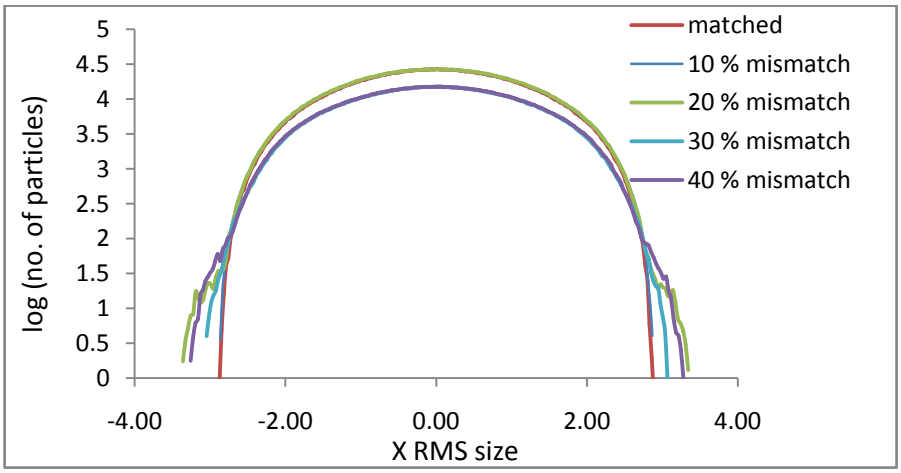

Fig. 4.11 a. Beam distribution in x for a + + + mismatch.

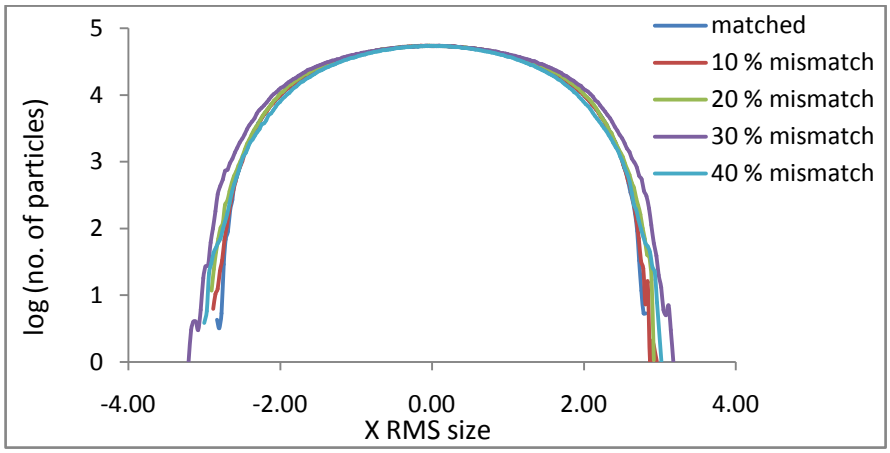

Fig. 4.11 b. Beam distribution in y for a + + + mismatch.

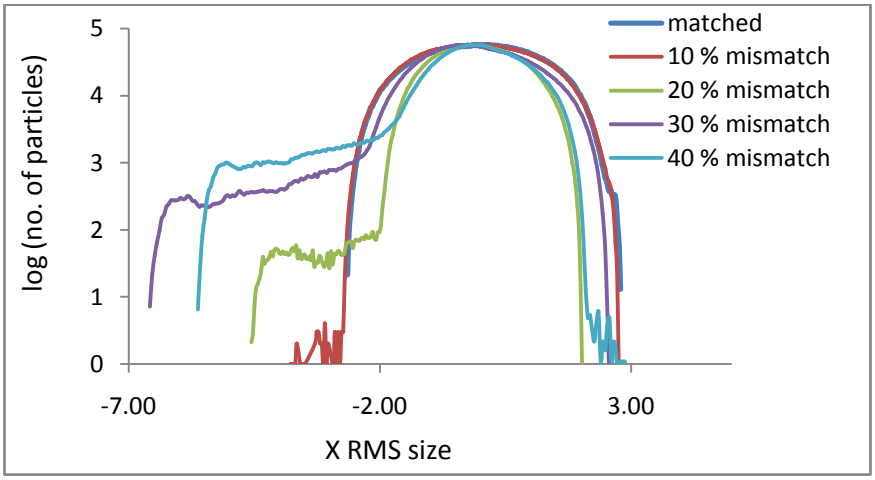

Fig. 4.11 c. Beam distribution in z for a + + + mismatch.

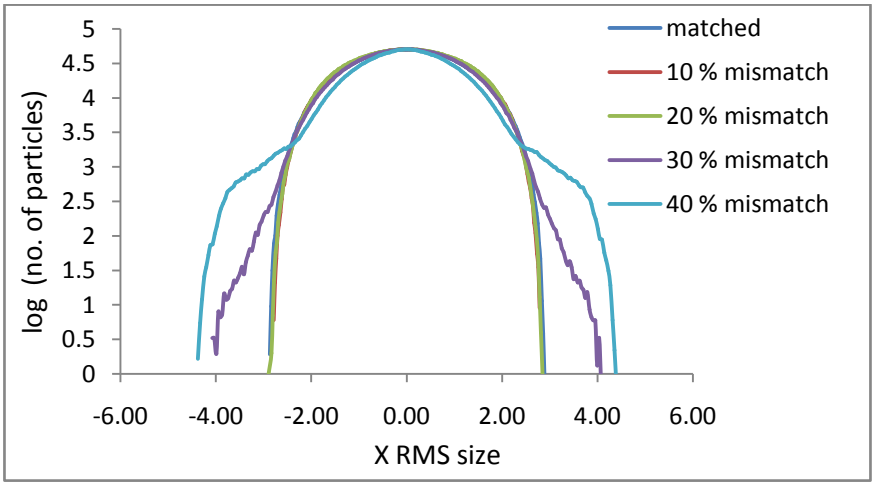

Fig.4.12 a. Beam distribution in x for a + - + mismatch.

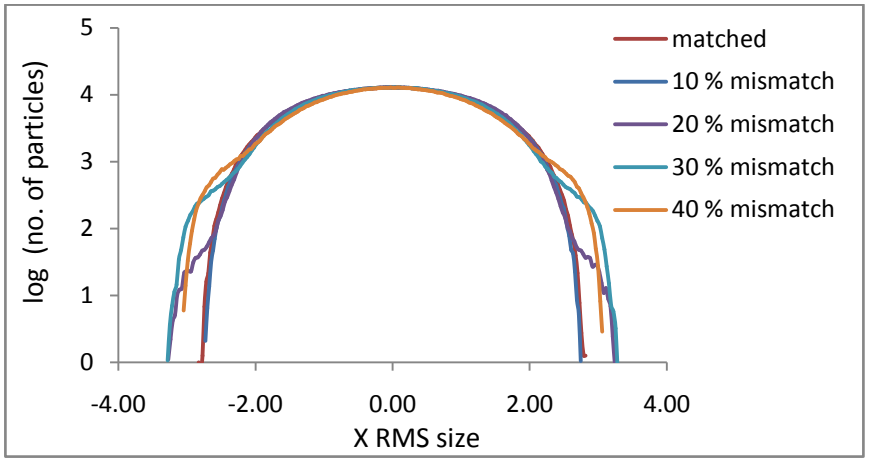

Fig.4.12 b. Beam distribution in y for a + - + mismatch.

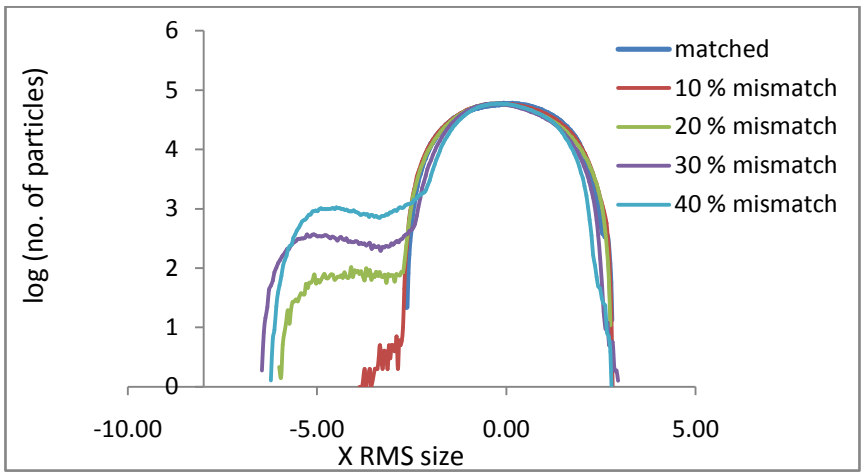

Fig.4.12 c. Beam distribution in z for a + - + mismatch.

Table 4.2. Halo parameter and PHP, PHS values for different mismatch.

	Halo Parameter			PHP (%)			PHS (%)		
	x	y	z	x	y	z	x	y	z
+ + +									
10%	0.42	0.44	0.47	0.5	0.5	0.4	14	19.5	28
20 %	0.43	0.45	1.05	0.54	0.77	0.63	28	21	48
30 %	0.43	0.45	1.9	0.62	0.84	2.14	27	25	54.8
40 %	1.0	0.5	2.2	0.92	1.34	5.73	24	28	61
+ - +									
10 %	0.43	0.43	0.49	0.7	0.61	0.54	17.5	17	29.4
20 %	0.45	0.55	0.9	0.9	0.59	0.75	21.2	30.5	47
30 %	0.8	0.85	1.5	2.3	2.58	1.58	48.5	36.5	55
40 %	1.1	1.15	2.1	5.8	4.0	2.93	57.0	33.5	56

4.5. Halo for different input currents

The evolution of beam halo through the DTL was studied for matched case and a 30%, -30%, 30 % mismatch (in x, y, z planes respectively) for 10 mA, 20 mA, 30 mA and 40 mA beam currents.

The halo parameter for a matched input beam along the length of the DTL is shown in Fig. 4.13. For a 10 mA matched beam, halo does not increase in either the transverse or longitudinal planes. However, as the current increases, the longitudinal halo grows even for a matched input beam. For a 30 mA beam, the halo parameter in z-z' plane at the DTL output is 0.54, which is a significant growth over a length of 11.92 m. The halo becomes worse with increasing current, reaching 0.57 at 40 mA. However, at all currents, the halo growth in the transverse planes is not very significant.

These results show that for a perfectly matched beam, transverse beam halo may not be a problem even at very high currents. However, for currents over 10 mA, longitudinal halo does

arise, and therefore for ADS linacs this issue needs to be studied more carefully at higher energies.

The simulations were done with 30 %, -30 %, 30 % mismatch. Results for the growth of the beam halo parameter are shown in Fig. 4.14. It can be seen that for 10 mA current, even with a mismatch of 30% there is no growth in the transverse or longitudinal beam halos. At 20 mA, there is still no appreciable transverse halo, but the longitudinal halo has now grown, from 0.45 to 0.7 at the exit of the DTL. At 30 mA too, the longitudinal halo has grown, from 0.54 to 1.5. In addition, there is now a growth in the transverse beam halo, reaching 0.6 and 0.8 (in X & Y). Again, the situation is worse with increasing current, and at 40 mA the longitudinal halo has grown to 2.8, and the transverse halos to 0.9 and 0.7 (in X & Y). Note also that there are large oscillations in the logitudinal halo, so that the halo can actually be larger than these values at points within the DTL. It can also be seen that the halo is growing with distance down the DTL, and therefore one may expect that the situation will worsen as the beam from the DTL is accelerated to higher energy. The PHP and PHS values are listed in Table 4.3 for matched and mismatched case.

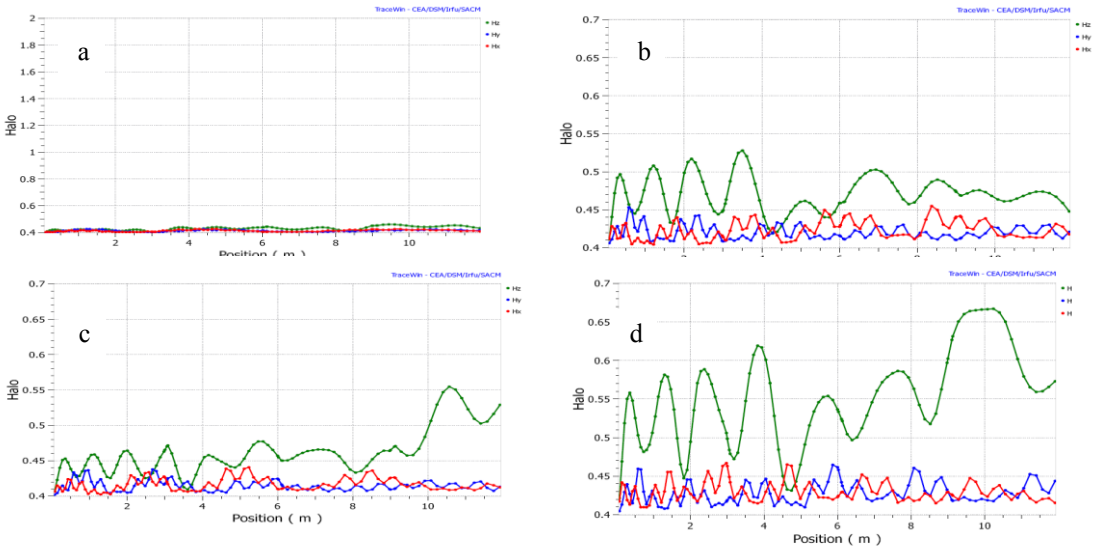

Fig 4.13.Halo Parameter along the DTL for matched input beam.

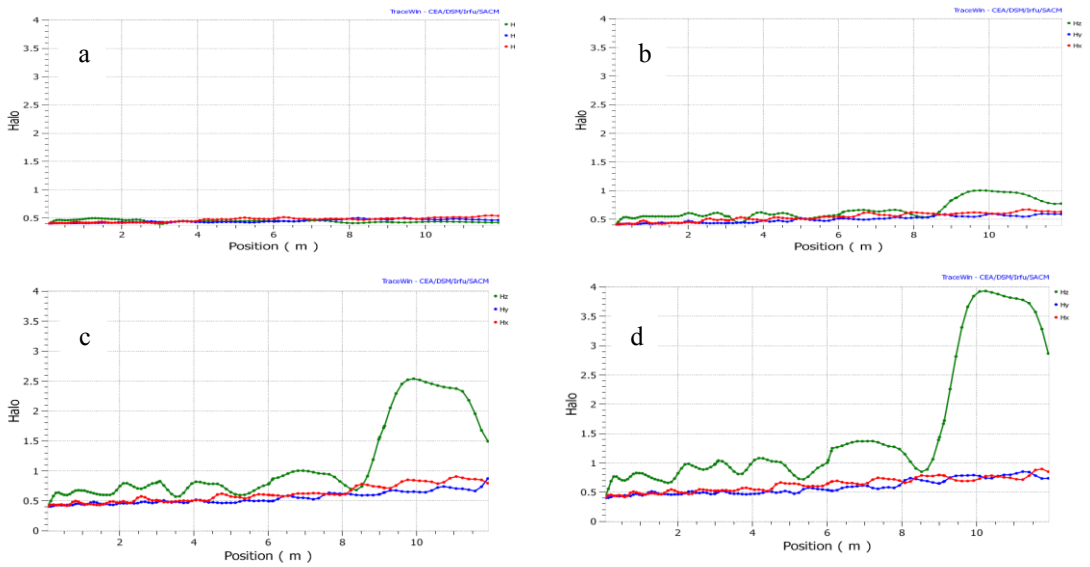

Fig 4.14. Halo Parameter along the DTL for 30 % -30 % 30 % mismatch input beam.

Table 4.3. The percentage of halo particles and the percentage of halo size for matched and mismatched input beams.

Beam Current	PHP (%)			PHS (%)		
Matched	x	y	z	x	y	z
10 mA	1.12	0.75	2.91	21.5	18	29
20 mA	1.02	0.3	0.6	36	15.5	20
30 mA	0.55	0.4	0.4	17	16.7	15
40 mA	0.8	0.6	0.15	29.5	14.5	12.5
Mismatched						
10 mA	5.8	1.7	3.8	41	30.54	27
20 mA	3	0.5	1.5	36	16	39
30 mA	2.5	2.5	1.5	48	36	54
40 mA	0.6	0.88	1.7	20.2	40.66	51.05

The beam distribution at the output in x-x', y-y', Δϕ-ΔW and x-y planes are shown in Fig. 4.15 for all the four beam currents with input mismatch. It is clear from this figure, that as the beam current increases, the beam distorts increasingly in all the three phase space planes. The situation is worst in longitudinal plane. For currents of 20 mA

and more, beam filamentation becomes quite pronounced and at 30 mA the transverse plane clearly indicates the formation of halo.

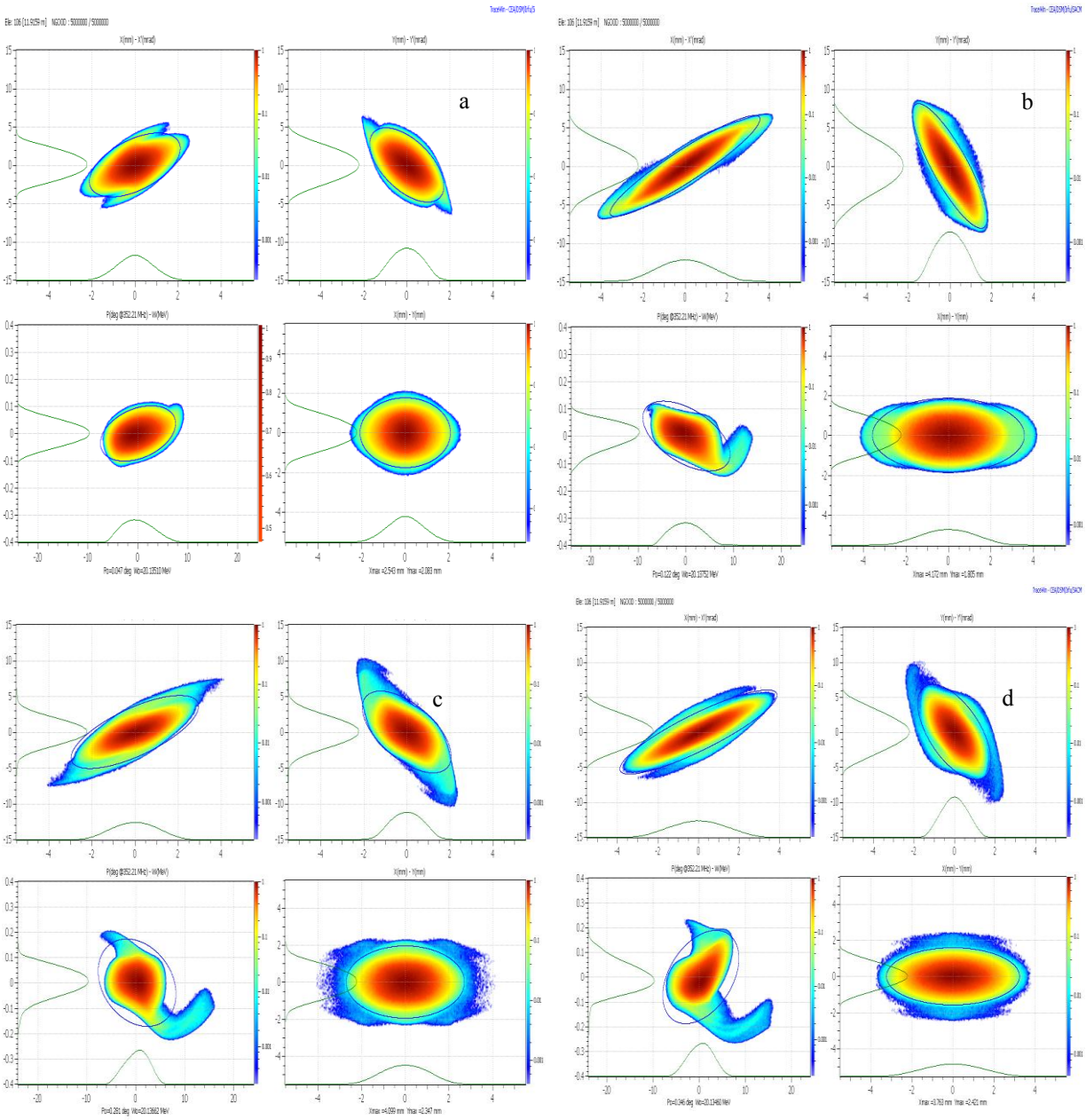

Fig. 4.15. Beam at the DTL output in x-x', y-y', Δφ-ΔW and x-y planes with a 30 %, -30 %, 30 % mismatch at the input for (a) 10 mA (b) 20 mA (c) 30 mA (d) 40 mA.

CHAPTER 5

RF Characterization of DTL Prototype

5.1 Introduction

The DTL, at 352.21, MHz has been designed to accelerate the proton beam from 3 MeV to 20 MeV. The total length of the DTL is 11.92 m and it will be built in four tanks, each of length about 3 m. The total power requirement is 1.5 MW. To validate the electromagnetic simulations [68] it was decided to fabricate a 1.2 m long prototype of the DTL containing the first 16 cells of the first DTL tank. The 1.2 m long DTL was simulated in MDTFISH (shown in Fig.5.1). The frequency was found to be 352.206 MHz for a tank diameter of 52 cm without 3D features.

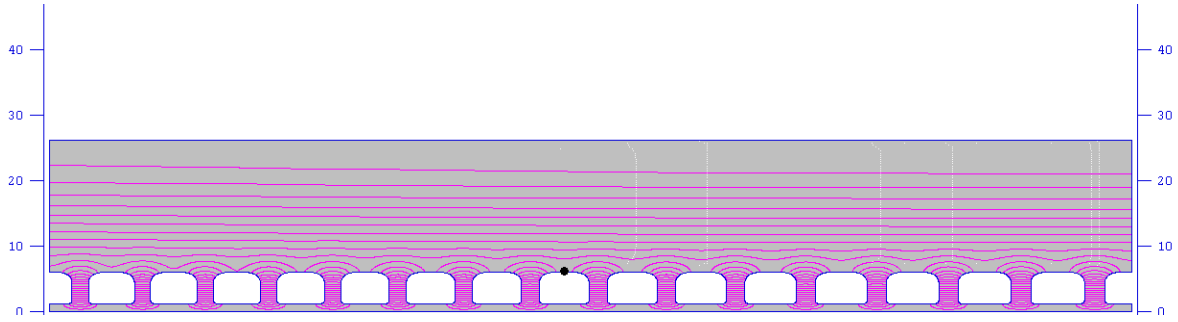

Fig 5.1. A 1.2 m long DTL simulated in MDTFISH.

It was planned to put 3 tuners of diameter 12 cm each in this 1.2 m prototype of the DTL. The tuning range of the tuners has been calculated using CST Microwave Studio and is found to be around 2.8 MHz. The nominal position of the tuners is half way inserted, i.e., inserted inside the tank wall to a depth of 5.5 cm, so that the frequency can be tuned in both the directions. The DTL cavity diameter correction for half way inserted tuners and stems is calculated to be 52.6 cm. The DTL prototype has one vacuum port

and two RF ports. The shifts in frequency due to vacuum and RF ports have been calculated to be 21 kHz and 10 kHz respectively, which is negligible. No post couplers were provided in this prototype. The prototype [69] consists of an MS tank electroplated with copper, 17 drift tubes made of aluminium, and 3 tuners also of aluminium. The drift tubes had flat faces without any face angle. The prototype is shown in Fig.5.2.

Fig. 5.2.A 1.2 m long prototype of the DTL.

5.2 RF cavity Characterization Basics

5.2.1 Quality Factor

The design of cavity resonators determines their efficiency at concentrating the field in the region of the beam, storing energy, having the correct resonant frequency and so on. The most important figure of merit is the cavity quality factor, defined as

$$Q = 2\pi \frac{Stored\ \ Energy}{Energy\ \ Consumed\ \ per\ period} = \frac{\omega U}{P} \qquad (5.1)$$

where, U is the stored energy, P is the average rate of energy loss and ω is the natural resonant frequency. If the resonator is unloaded, $Q = Q_0$, and U is the Power lost in the cavity, but if the resonator is open and loaded, then $Q = Q_L$ and P is the Power lost in the cavity and the external system [70].

5.2.1.1 Closed Cavity

In a closed cavity, the Power loss is equal to the rate of change of stored energy.

$$P = -\frac{dU}{dt} \tag{5.2}$$

Using equation (5.1) to write U in terms of P and integrating one gets,

$$P = P_0\, e^{-t/\tau_P} \tag{5.3}$$

where $$\tau_P = \frac{Q}{\omega} \tag{5.4}$$

Since, energy is proportional to the square of the field, the field decays as,

$$E(t) = E_0\, e^{-t/2\tau_P} e^{i\omega t} \tag{5.5}$$

The homogeneous differential equation for an oscillator with damping factor p is

$$\frac{d^2E}{dt^2} + p\,\frac{dE}{dt} + \omega_0^2 E = 0 \tag{5.6}$$

Substituting a trial solution $E = E_0\, e^{\lambda t}$ yields,

$$\lambda^2 + p\lambda + \omega_0^2 p = 0 \tag{5.7}$$

$$\lambda = -\frac{p}{2} \pm i\sqrt{\omega_0^2 - (p/2)^2} = -\frac{p}{2} \pm i\omega \tag{5.8}$$

If $\omega_0^2 > (p/2)^2$, then the solution for field is harmonic with an exponential slope. Thus the field decay is given by,

$$E = E_0 e^{-\left(\frac{p}{2}\right)t} e^{i\omega t} \tag{5.9}$$

Comparing with (5.5), the damping factor is obtained as,

$$p = \frac{\omega}{Q} \tag{5.10}$$

5.2.1.2 Cavity with external excitation

The differential equation for a damped oscillator with external excitation is

$$\frac{d^2E}{dt^2} + p\,\frac{dE}{dt} + \omega_0^2\,E = C\,e^{i\omega t} \tag{5.11}$$

The right hand side of the above equation represents the external driving force with frequency ω. Substituting the trial solution $E = A\,e^{i\omega t}$,

$$A = \frac{C}{(\omega_0^2 - \omega^2) + i\omega p} = \frac{C}{(\omega_0^2 - \omega^2) + i\,\frac{\omega\,\omega_0}{Q}} \tag{5.12}$$

It can be seen from equation (5.12), that as $\omega \to 0$, $A \to \frac{C}{\omega_0^2}$ $and\ as\ \omega \to \infty, A \to 0$.

When the external frequency is close to the natural frequency, then

$$A = \frac{C}{2\omega_0 \Delta\omega + i\frac{\omega_0^2}{Q}} \tag{5.13}$$

Thus A is maximum when Δω is zero, that is the cavity is tuned to the resonant frequency. In this case,

$$A = \frac{CQ}{i\omega_0^2} \quad and \quad |A|_{max} = \frac{CQ}{\omega_0^2} \tag{5.14}$$

The stored energy is proportional to the square of the field

$$U \propto |A^2| = \frac{C^2/4\omega_0^2}{\Delta\omega^2 + \left(\frac{\omega_0}{2Q}\right)^2} \tag{5.15}$$

The quality of resonator is characterised by the 'narrowness' of its resonance. If $\Delta\omega_H$ is the full width at half height of the stored energy vs excitation frequency curve (Fig. 5.3), then by (5.15)

$$\Delta\omega_H = \frac{\omega_0}{Q},\ or\ \ Q = \frac{\omega_0}{\Delta\omega_H} = \frac{f}{\Delta f_H} \tag{5.16}$$

From the above equation, it is clear that Q is the measure of the narrowness of the resonance and hence the quality of the resonator.

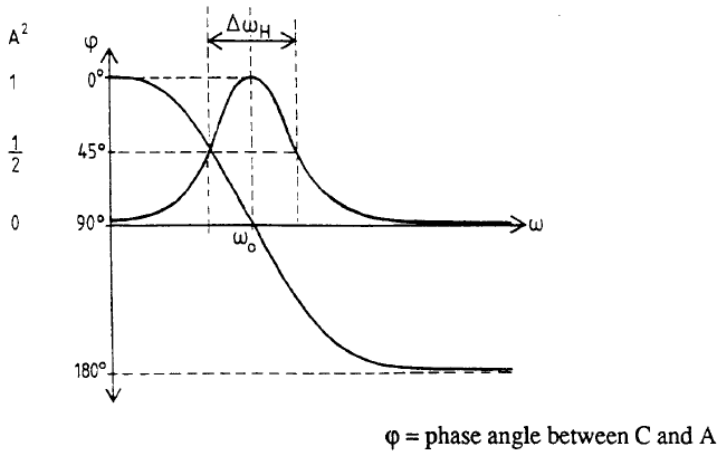

Fig. 5.3.Stored Energy and Phase Shift with respect to the excitation of the resonator.

The field amplitude is related to the excitation signal amplitude by equation (5.13). the phase between these amplitudes is given by

$$\tan\varphi = -\frac{\omega\omega_0/Q}{\omega_0^2-\omega^2} \tag{5.17}$$

When $\omega = 0, \varphi = 0$

$\omega = \infty, \varphi = -\pi$

$\omega = \omega_0, \varphi = -\pi/2$

For small angles,

$$\tan\Delta\varphi \approx \frac{2\,Q\,\Delta\omega}{\omega}\ so\ that,\ \Delta\varphi \approx \frac{2\,Q\,\Delta\omega}{\omega} \tag{5.18}$$

5.2.2 Measurement of Resonant Frequency

The resonant frequency measurement involves in measuring the transmission coefficient (S_{21}) by applying an excitation signal through one port and receiving the transmitted signal from another port. The transmission coefficient is defined as the ratio of reflected voltage at port 2 to the incident voltage at port 1, when the incident voltage wave on all ports except the first port are turned to zero. In microwave frequencies the voltage and current are usually determined from the power and phase of wave travelling in a particular direction and can be expressed in terms of decibels (dB) as [71]

$$S_{21} = 10 \log \frac{P_2^-}{P_1^+} \tag{5.19}$$

Since the power is proportional to the square of the field, the S_{21} parameter varies with frequency in a manner similar as shown in Fig. 5.3. The frequency at which S_{21} is maximum is the resonant frequency of the cavity.

5.2.3 Field Measurements

If a perturbation is introduced in a cavity such that the parameters of the oscillator vary slowly, then according to the Boltzmann- Ehrenfest theorem [73,74], the frequency is proportional to the energy of the oscillator. For a cavity in resonance, the electric and magnetic stored energies are equal. A perturbation in the cavity leads to an imbalance of the electric and magnetic energies and the resonant frequency shifts to restore the balance. Slater perturbation theorem [35] describes the shift of resonant frequency, when a small volume ΔV is removed from a cavity in terms of the stored energy of the cavity.

$$\frac{\Delta\omega_0}{\omega_0} = \frac{\int(\mu_0 H^2 - \varepsilon_0 E^2)dV}{\int(\mu_0 H^2 + \varepsilon_0 E^2)dV} \tag{5.20}$$

where E and H are the unperturbed field amplitudes.

The field measurements are based on the Slater Perturbation theorem. If a small bead is inserted into the cavity, the perturbation shifts the resonant frequency. For a spherical bead of volume ΔV the shift is given as a function of the unperturbed field amplitudes E and H, which are assumed to be constant over the bead, by

$$\frac{\Delta\omega_0}{\omega_0} = -\frac{3\,\Delta V}{4U}\left(\frac{\varepsilon_r - 1}{\varepsilon_r + 2}\varepsilon_0 E^2 + \frac{\mu_r - 1}{\mu_r + 2}\mu_0 H^2\right) \tag{5.21}$$

where ε_r and μ_r are the dielectric constant and magnetic permeability of the bead material. For a spherical dielectric bead with $\mu_r = 1$,

$$\frac{\Delta\omega_0}{\omega_0} = -\frac{3\,\Delta V}{4U}\frac{\varepsilon_r - 1}{\varepsilon_r + 2}\varepsilon_0 E^2 \tag{5.22}$$

This equation relates the frequency shift due to a bead perturbation to the unperturbed electric field in the cavity. This forms the basis for bead pull measurements for fields in the cavity. The measurement of frequency shift is sometimes difficult if the bead is small or the electric field in the cavity is small. In such cases, it is advantageous to measure the phase shift of S_{21} at the "unperturbed" resonant frequency as the bead is pulled through the cavity. The phase shift is related to frequency shift by equation (5.18) and provides a means for a more sensitive measurement of fields.

5.2.4 Calculation of RT^2/Q

The ratio of effective shunt impedance to the quality factor of a cavity, is an important figure of merit and it measures the efficiency of acceleration per unit stored energy at a given frequency. It is a function only of cavity geometry and is independent of the surface properties that determine the power losses. By mapping the longitudinal distribution of E_z and integrating, the cavity shunt impedance can be calculated as

$$RT^2 = \frac{(VT)^2}{2P} = \frac{\left[\int E_z(z) e^{j\omega\frac{z}{v}} dz\right]^2}{2P} \tag{5.23}$$

where v is the velocity of the particles, while

$$E^2 = -\frac{\Delta\omega PQ\,(\varepsilon_r+2)}{\omega^2\pi r^3\varepsilon_0(\varepsilon_r-1)} \tag{5.24}$$

If the cavity is symmetric in z and t = 0 at z = 0 in the center, the impedance can be written as

$$\frac{RT^2}{Q} = \frac{1}{2\omega\pi\, r^3\varepsilon_0}\frac{\varepsilon_r+2}{\varepsilon_r-1}\left[\int dz\sqrt{\frac{\Delta\omega}{\omega}}(z)(\cos kz)\right]^2 \tag{5.25}$$

where Q is the quality factor, r is the bead radius, ε_r is the relative dielectric constant and k is the wave number (= ω/c). From the bead pull measurements, by measuring the phase shifts as a function of z as the bead passes longitudinally along the cavity, the frequency shift, Δf/f can be calculated as a function of z. The function $\sqrt{\frac{\Delta\omega}{\omega}}(z)(\cos kz)$ can then be evaluated for various z values. The ratio, RT^2/Q can then be determined using equation (5.25).

5.3 Measurements on the Prototype

5.3.1 Resonant Frequency

Frequency measurements were done on the DTL prototype [75] using the Vector Network Analyzer (Fig.5.4). The measured frequency in air with all tuners flush was 348 MHz. The resonant frequency with all the 3 tuners inserted at 10.5 cm was found to be 350.745 MHz. The Quality factor was measured to be 2,500. The quality factor is poor because the drift tubes and tuners are made of aluminium, which has higher resistivity and hence higher power loss as compared to copper. Also the copper plating on the tank surface had a poor finish. The simulations were done for annealed copper at 20^0C and the calculated value of quality factor was 40000 for the 1.2 m prototype. The frequency was

measured as a function of varying tuner depth. The measured and simulated frequency shift as a function of tuner depth has been plotted in Fig. 5.5. The measurements agree well with the simulations and the slopes of the two plots are quite close.

Fig. 5.4.Frequency measurements on the DTL prototype.

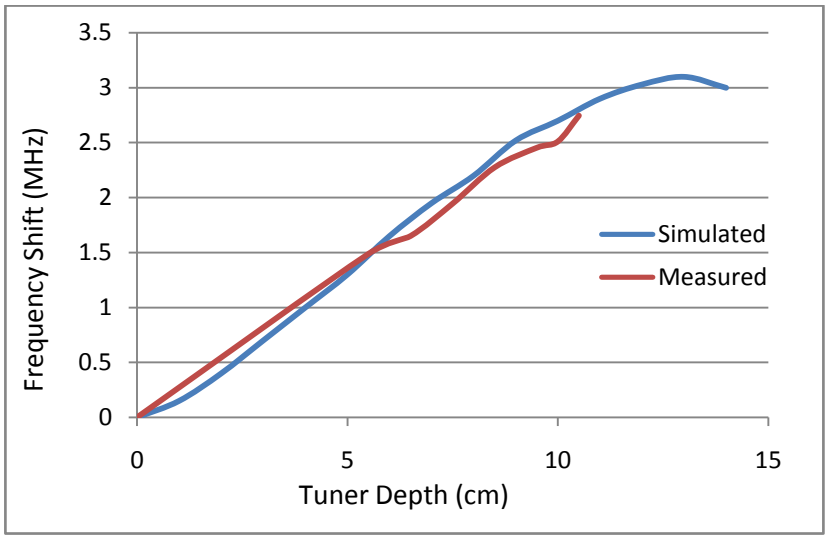

Fig. 5.5. Frequency shift vs tuner depth.

In order to analyse the difference between the designed frequency and measured frequency in the DTL prototype more simulations were done to study the effect of various DTL dimensions which could have been different in the fabricated DTL prototype. Simulations were also done to take into account the change in frequency due to the medium being air instead of vacuum which was assumed in the original simulations.

The effect of tank diameter on the resonant frequency was studied using SUPERFISH as well as CST Microwave Studio. Increasing the tank diameter causes an increase in magnetic volume and hence a decrease in resonant frequency. The frequency decreases linearly at a rate of -4.7 MHz/cm and -4.9 MHz/cm calculated with SUPERFISH and CST MWS respectively. The results are plotted in Figs. 5.6.

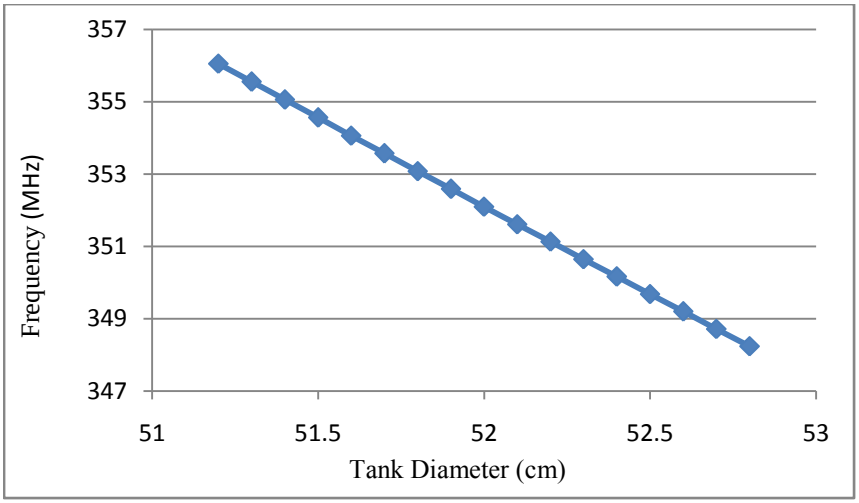

Fig.5.6. Frequency as a function of Tank diameter.

The effect of drift tube diameter on the resonant frequency was also studied using SUPERFISH as well as CST Microwave Studio. This has been plotted in Fig. 5.7. Increasing the drift tube diameter causes an increase in magnetic volume, and hence a decrease in the resonant frequency. The resonant frequency decreases linearly at a rate of

-8.6 MHz/cm, calculated using SUPERFISH and at -7.75 MHz/cm calculated using CST MWS.

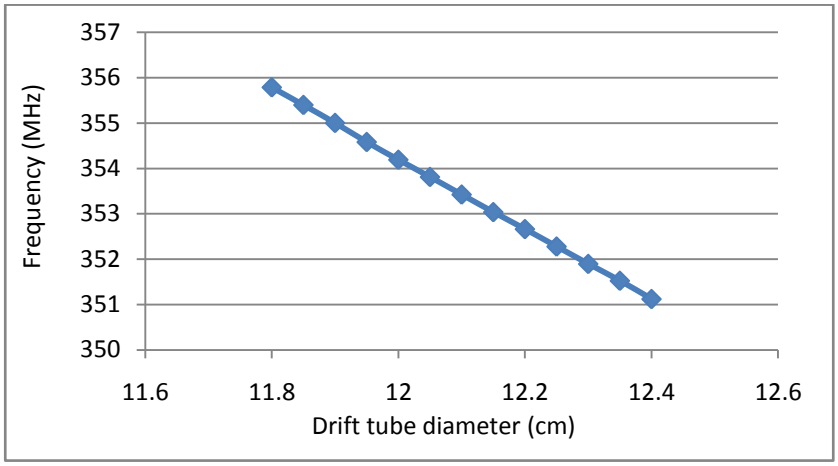

Fig. 5.7. Frequency as a function of drift tube diameter.

The effect of bore radius on the resonant frequency is plotted in Fig.5.8. By increasing the bore radius, the electric volume of the cavity is increased and hence the resonant frequency increases. The increase in frequency is linear at a rate of 2.46 MHz/cm.

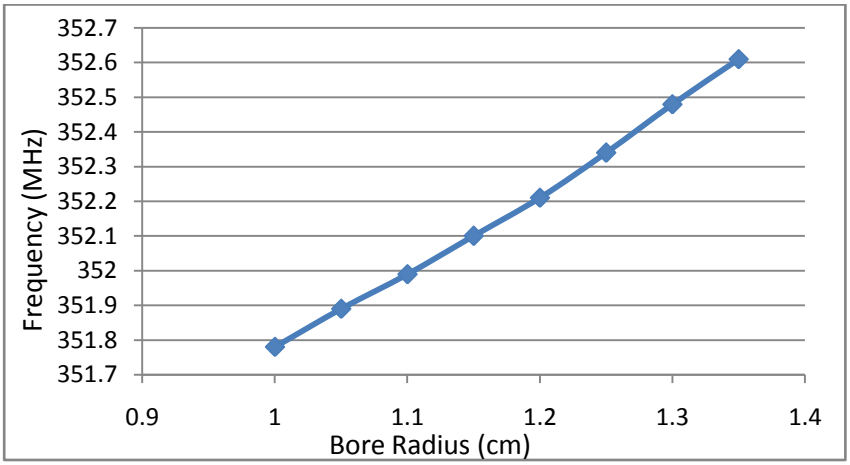

Fig.5.8. Frequency as a function of Bore Radius.

The effect of varying corner radius of the DTL on the resonant frequency was studied and is plotted in Fig. 5.9. The resonant frequency is quite sensitive to the

variation in the corner radius and it increases linearly with corner radius at a rate of 6.581 MHz/cm.

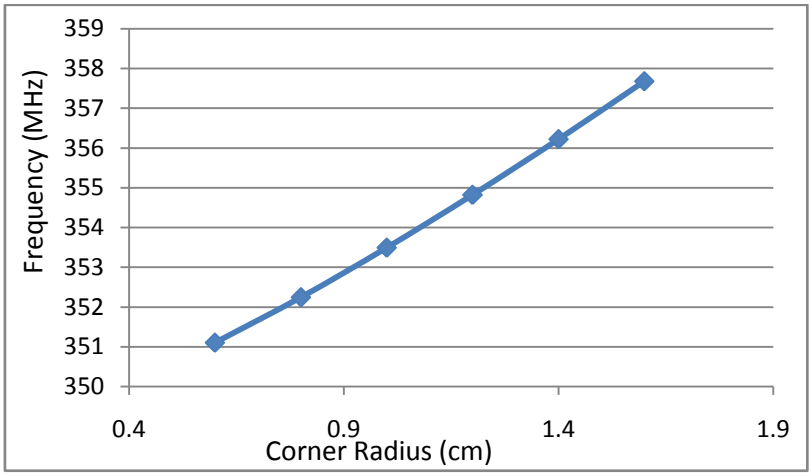

Fig.5.9. Frequency as a function of corner radius.

The effect of varying stem radius on frequency is shown in Fig. 5.10. The frequency increases linearly with stem radius at a rate of 1.71 MHz/cm.

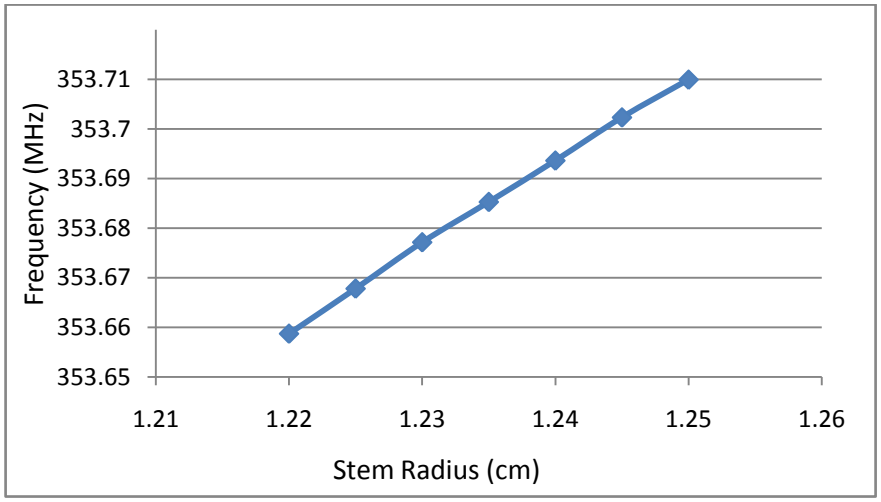

Fig.5.10. Frequency as a function of stem radius.

The effect of resonant frequency on relative permittivity of the medium has also been studied using SUPERFISH and is plotted in Fig.5.11. The shift in frequency for air (ε_r= 1.0006) is 40.4 kHz.

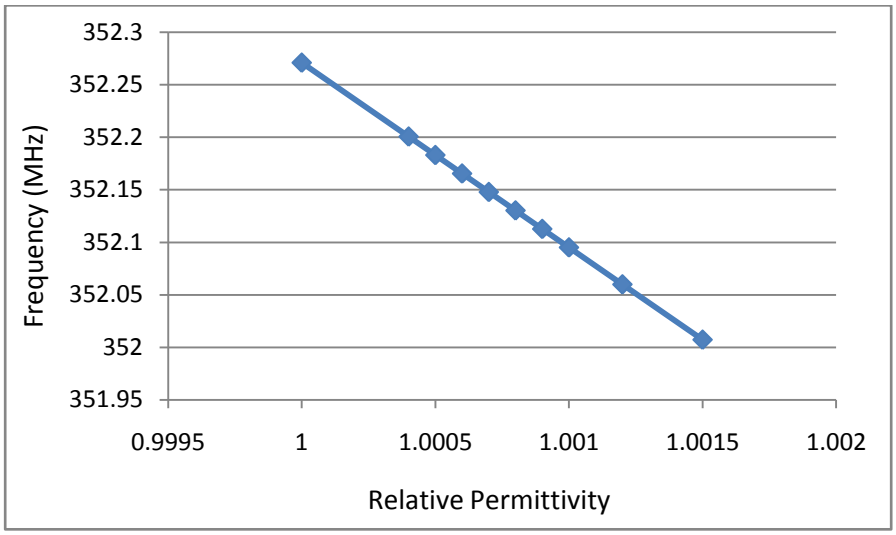

Fig. 5.11. Frequency as a function of the relative permittivity of the medium.

From the frequency sensitivity analysis, the frequency of the DTL with fabricated dimensions was calculated. The corner radius of the fabricated prototype was 4 mm more than the actual dimension. This itself leads to a frequency shift of about 2.6 MHz. The initial simulation model in CST MWS assumed symmetry in all cells and the two end drift tubes had half stems connected to them, whereas in the actual case, the end half stems are not present. This produces a frequency shift of about 59 kHz. Also, due to the medium being air during measurement, there is a frequency shift of about 100 kHz. The frequency of the 1.2 m prototype from original simulation was 352.206 MHz for half-way inserted tuners. Incorporating the above mentioned corrections for the as-fabricated prototype in air, the frequency should be 2.759 MHz lesser than the simulated value. Accounting for these corrections, the simulations suggest a frequency of 349.45 MHz. The measured frequency of the DTL prototype with tuner depth of 5.5 cm was 349.49 MHz. This agrees very well with the simulations.

5.3.2 Electric Field Measurement

The bead pull measurements were done on the DTL prototype. A dielectric bead was moved along the axis of the DTL, where the electric field is maximum and magnetic field is zero. The bead intercepts the electric volume and produces a small frequency shift which is proportional to the electric field. The phase of S_{21} was measured and the frequency shift was calculated from it. Fig. 5.12 shows the phase of S_{21} along the DTL. The beam dynamics simulations require that the field uniformity should be within ±2 %. The tuner positions were adjusted to obtain a uniform field in all the gaps. The field uniformity of ±2 % was achieved for tuner positions of 3.75 cm, 2.95 cm, 10.05 cm. Fig. 5.13 shows E/E_{avg} as a function of gap number.

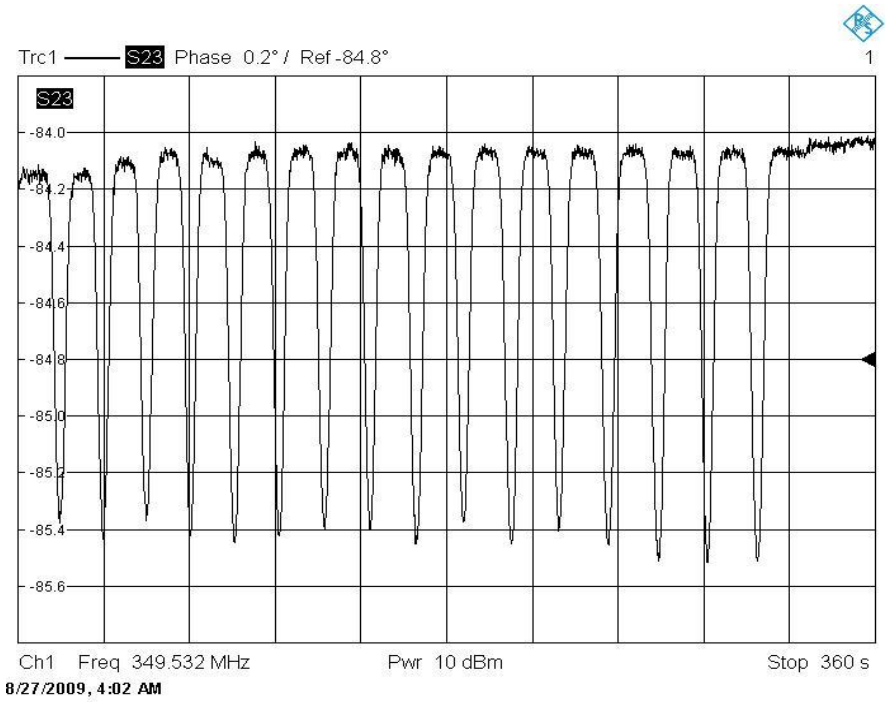

Fig. 5.12. Phase of S_{21}.

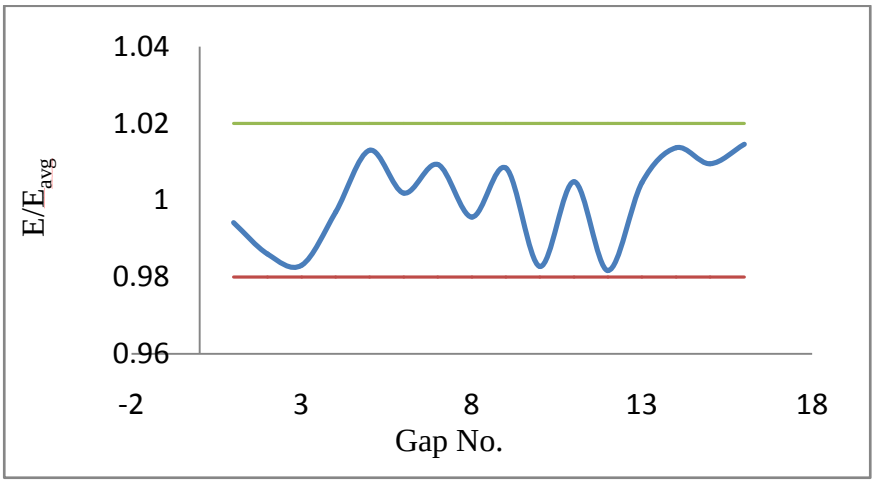

Fig. 5.13. E/Eavg vs gap no.

5.3.3 Calculation of RT^2/Q

The phase of S_{21} was measured as a function of bead position along the axis of the DTL prototype by bead pull method and the frequency shift was determined. The ratio of effective shunt impedance to the quality factor, RT^2/Q was then evaluated from the equation (5.25). The value of RT^2/Q is estimated to be 36.45 Ω. The simulated value from SUPERFISH is 37.2 Ω. The measured value agrees well with the simulations. The ratio RT^2/Q is independent of the surface properties and depends only on the cavity geometry. Therefore, though the quality factor is poor, signifying poor surface properties, specially because of aluminium components in the prototype and poor finish of copper plating on the tank surface, the ratio RT^2/Q, representing the cavity geometry is in close agreement with the simulations.

5.4 Conclusions

A 1.2 m long prototype was fabricated and RF characterization was done on it. The frequency of the prototype was measured to be 349.49 MHz. The corner radius of the

prototype was ~ 4 mm more than the designed value. This was the main reason for the departure of the measured frequency from the simulated value. The simulations with the correct dimensions and air medium gave a resonant frequency very close to the measured one. Bead pull was done to measure the axial electric field in the prototype cavity. A field uniformity of ± 2 % was obtained with the help of tuners. A measurement of RT^2/Q was done and the measured result agreed well with the simulations. Based on these measurements, the fabrication of the 20 MeV DTL has been initiated.

CHAPTER 6

Summary and scope of future work

6.1 Summary

The work in this thesis is based on the design of a high intensity proton drift tube linac for LEHIPA at BARC and the RF characterization of a prototype.

Detailed design of a drift tube linac has been done. The cavity geometry has been optimized with an aim to maximize the effective shunt impedance while keeping enough space inside the drift tubes for focusing quadrupoles and cooling water channel. The beam dynamics design aim is to have 100 % transmission and minimum emittance growth. Detailed beam dynamics through the DTL has been done. Three focusing schemes have been studied and based on these studies; the FFDD focusing lattice has been chosen. The effect of space charge on the beam dynamics has also been studied. From these studies, it is concluded that the space charge effects are not significant at around 10 mA. If the tune depression is close to or goes below 0.4 even for a few periods, there is significant distortion in phase space and a consequent increase in emittance. For the designed DTL at 30 mA, space charge effects are observable and lead to emittance growth. The presence of errors in the real linac may exacerbate the situation and one may expect higher emittance growth and even beam loss. The Hofmann instabilities have been avoided in the design. The effect of beam alignment errors, quadrupole alignment and gradient errors and RF errors has been studied, based on which the tolerances on these parameters have been obtained.

The formation and evolution of beam halos in the DTL has also been studied. It is seen that a perfectly matched beam shows a halo in the longitudinal plane. The particle-core model is used to find the mismatch required to excite the three fundamental modes of the beam; the quadrupole mode, the fast mode and the slow mode. These studies have been done with uniform and Gaussian input distributions. With uniform distribution, the beam oscillations persist with unchanged amplitudes throughout the DTL. On the other hand, for a Gaussian distribution, the amplitudes get damped as the beam travels through the DTL. This is because the free energy available with the Gaussian distribution, leads to faster emittance growth. The particle redistribution at the end of the DTL has been obtained. These distributions show the formation of beam halos. Based on definition of Allen and Wangler, the halo parameter has been calculated for the three eigen modes. The halo definition proposed by Nghiem has been used to determine the percentage of halo size and the percentage of halo particles. Two cases of general mismatch have also been studied. The effect of varying beam currents on halo has also been studied and it is clear that halo grows with beam current. Longitudinal halos are formed even for a perfectly matched beam at currents of 20 mA and above. Transverse halos arise in the presence of mismatch and increase with increasing degrees of mismatch.

In order to validate the electromagnetic design of the DTL, a 1.2 m long prototype consisting of the first 17 cells of the first tank of the DTL, was fabricated. RF measurements were performed on the prototype. The results agree well with the simulations.

6.2 Scope of future work

The LEHIPA DTL design has been completed and measurement on a prototype has been done. Based on the design studies and measurements, the fabrication of the DTL has been initiated. The total length of the DTL is 11.92 m and it will be fabricated in four tanks. It will be useful to have some diagnostics and beam steering elements in the inter-tank space. The possibility of having some such elements in the limited available space is being worked out.

For the tuning of DTL during the cold test, in order to find the correct tuner and post coupler depth, it is useful to develop a tuning algorithm [76]. The tuning aim is to achieve the desired resonant frequency and to achieve a field uniformity and a field tilt sensitivity of $< \pm 2$ %. By writing a program for tuning, one can save several iterations of bead pull measurements to determine the correct tuner and post coupler depths. Such a program may be based on least squares method by determining the field profile at a particular tuner position and at a perturbed position for each tuner.

In the design of high intensity linacs, it is important to minimize the beam loss. Typically, the beam loss should be less than 1 W/m to allow hands on maintainance of accelerator and beam line components. Beam halos are one of the important mechanisms of beam loss. The formation of halos take place at low energies. This thesis discusses the halo formation due to 2:1 parametric resonance resulting from the interaction of mismatched beam core with the single particles. These studies have been done for a mismatch in the input beam. Another contribution to the beam halo stems from statistical gradient error which can be regarded as a multitude of individual mismatch sources. The

particle-core model can be extended to statistical gradient error [77] to excite the beam core which can then transfer energy to single particles by 2:1 parametric resonances.

The core-core resonance [78] is another mechanism for halo formation. This mechanism also needs a careful study. Unlike the particle-core model, the core-core resonance model requires to incorporate non-elliptical and changing bunch shapes as well as changing emittances. Therefore, the analytical treatment is based on an integration of the Vlasov equation and is limited to the evaluation of a KV distribution in two dimensions. There exists no three-dimensional treatment. This analysis [59] provides a set of 2D eigen modes. The modes are classified as even and odd modes; each of which has first, second, third and fourth order modes. The even modes are symmetric with respect to the horizontal axis, while the odd modes have no such symmetry. Such modes can not be found with analysis in r-z plane. First order modes are a trivial case of displacement from the beam axis, and the oscillation frequencies are just the betatron frequencies without space charge in each direction. The second order modes are similar to the fast and the breathing modes derived from Particle-core model. The third and fourth order modes are a result of non-elliptical bunch shapes and are novel to the Vlasov analysis. By studying the core-core resonance one needs to answer the question if these resonances can contribute to halo formation.

REFERENCES

1. Helmut Wiedemann, Particle Accelerator Physics I, Basic Principles and Linear Beam Dynamics (1998), Page 5.
2. M.S. Livingston, The Development of High Energy Accelerators Dover, New York, 1966.
3. J.D. Cockroft and ETS Walton, Nature 129 (1932) 242.
4. R J Van de Graaff, K T Compton and L C Van Atta , Phys. Rev. 43 (1933) 149.
5. R J Van de Graaff, Nucl. Instrum. Method, 8 (1960) 195.
6. L.W. Alvarez, Phys. Rev. 70 (1946) 799.
7. L.W. Alvarez et. al., Rev. Sci. Instrum. 26 (1955) 111.
8. T. P. Wangler, Principles of RF Linear Accelerators, John Wiley & Sons, INC, 1998, Page 95-102.
9. P. Lapostolle, A. Septier, Linear Accelerators, Amsterdam, North Holland (1970), Page 588-590.
10. Robert W. Garnett, Status of the Los Alamos Accelerator Code Group, LANL, ICAP (2002).
11. F. Carminati, R. Klapisch, J.P. Revol, J.A. Rubio and C. Rubbia CERN/AT/93-47 (ET); C. Rubbia et al; CERN/AT/95-44 (ET); CERN/LHC/96-01 (EET); CERN/AT/95-53 (ET); CERN/LHC/97-01 (EET).
12. S.S. Kapoor, "Roadmap for development of Accelerator Driven Sub-Critical Reactor Systems", BARC/2001/R/004.
13. Rajni Pande, Shweta Roy, S.V.L.S. Rao, P Singh and S Kailas Physics design of a CW high-power proton LINAC for ADS, Pramana – J. Phys. 78, 247 (2012).

14. P. Singh, S.V.L.S. Rao, Rajni Pande, T. Basak, Shweta Roy, M. Aslam, P. Jain, S.C.L. Srivastava, Rajesh Kumar, P.K. Nema, S. Kailas and V.C. Sahni, Accelerator Development in India for ADS Programme, Pramana – J. Phys. 68, 33 (2007).
15. John W. Staples, "RFQs- An Introduction". AIP Conf Proc. 249, 1483 (1992).
16. S.V.L.S. Rao and P Singh, Design studies of a high-current radiofrequency quadrupole for accelerator-driven systems programme, Pramana – J. Phys. 74, 247 (2010).
17. S. Roy, S.V.L.S. Rao, R. Pande, S. Krishnagopal and P.Singh, Electromagnetic and Beam Dynamics studies of a high current linac for LEHIPA, Journal of Instrumentation 9, 06007 (2014).
18. E. Tanke, S. Assadi, G. Dodson, J. Galambos, M. Giannella, N. Holtkamp, D. Jeon, M. White, Kravchuk, M. Plum, R.Shafer, J. Stovall, Commissioning plans for the SNS DTL and CCL, Proceedings of LINAC 2002, Gyeongju, Korea.
19. Y. Kondo, M. Ikegami, T. Kobayashi, T. Ohkawa, and A. Ueno, Beam Dynamics and Commissioning of the J-PARC Linac, 33rd ICFA Advanced Beam Dynamics Workshop on High Intensity and High Brightness Hadron Beams. AIP Conference Proceedings, 773, 79-83 (2005).
20. C.E. Hill, A.M. Lombardi, W. Pirkl, E. Tanke, M. Vretenar, Performance of the CERN Linac 2 with a high Intensity Proton RFQ, 17th International Linac Conference, Tsukuba, Japan, 1994.
21. S. Ramberger, N. Alharbi, P. Bourquin, Y. Cuvet, F. Gerigk, A.M. Lombardi, E. Sargsyan, M. Vretenar, A. Pisent, Drift Tube Linac Design and Prototyping for the CERN LINAC4, Proceedings of LINAC 2008, Victoria, BC, Canada.

22. A. Pisent, M. Comunian, A. Palmieri, Enrico Fagotti , P. A. Posocco, F. Grespan Design of the High Current Linac of SPES, Proceedings of EPAC 2008, Genoa, Italy.
23. J.H. Jang, Y.S. Cho, H.J. Kwon, K.Y. Kim, Y.H. Kim, PEFP / KAERI, Daejeon, Korea, Beam Dynamics Design of the PEFP 100 MeV Linac, Proceedings of HB2006, Tsukuba, Japan.
24. M. Lindroos , S. Molloy, D. McGinnis, C. Darve, H. Danared, ESS AB, Lund, Sweden and the ESS Accelerator Collaboration, The ESS Linac Design , Proceedings of LINAC2012, Tel-Aviv, Israel.
25. Zhirui Sun, Xuejun Yin, Keyun Gong, Jun Peng, Shinian Fu , DTL Tank Development of 132 MeV Linac for CSNS, Proceedings of LINAC 2008, Victoria, BC, Canada.
26. D. J. Liska, H. Mignardot, J . H. Billen, L. B. Dauelsberg, and G. W. Zimmerman, A High-Intensity Drift-Tube Linac with ramped accelerating gradient, Proceedings of the 1988 Linear Accelerator Conference, Williamsburg, Virginia, USA.
27. P.-E. Bernaudin, et. al., Results of the IPHI Drift Tube Linac's hot model CW Tests, Proc. PAC (2003).
28. Nita S. Kulkarni, Design of a 10 MeV, 352.2 MHz drift tube linac, Pramana – J. Phys., 79, 263, (2012).
29. E.V. Kozyrev, Standing Wave Structures, Budker Institute of Nuclear Physics 630090 Novosibirsk, Russia.
30. CST microwave studio, simulation tool for electromagnetic analysis and design, CST, Germany.
31. J. H . Billen and L M Young, Poisson Superfish, LA-UR-96-1834, LANL.

32. J. H. Billen, H. Takeda, and T. S. Bhatia, Linac RF Structures for the Spallation Neutron Source, PAC (1999).

33. J. Stovall, RF Breakdown in Drift Tube Linacs, sLHC Project Note 0007.

34. Shweta Roy, Rajni Pande, S.V.L.S. Rao, P. Singh, Electromagnetic Design of DTL cavity for LEHIPA, Proceedings of DAE-BRNS-PSI Symposium on Ion Beam Technology and Applications.

35. J C Slater, Microwave electronics, D.Van Nostrand, New York, 1950, Page 80-81.

36. S. Shen, Design and Analysis of Vacuum Pumping Systems for Spallation Neutron Source Drift-Tube Linac and Coupled-Cavity Linac, Proceedings of the 2001 Particle Accelerator Conference, Chicago

37. F. Grespan, Equivalent circuit for post coupler stabilization in a drift tube linac , Phys. Rev. Special Topics - Accelerators and beams 15, 010101 (2012).

38. Fujio Naito, Takao Kato, Yoshishige Yamazaki and Eiichi Takasaki, A tuning method of post couplers for a low β Drift Tube Linac, Particle Accelerators, Vol. 32 (1990) 27

39. N. Alharbi, F. Gerigk, M. Vretenar, Field Stabilization with Post Couplers for DTL tank1 of Linac4, CARE-Note-2006-012-HIPPI.

40. S.Y. Lee, Accelerator Physics(World Scientific, 2004), Page 17.

41. J.H.Billen, *PARMILA* Code, LA-UR-98-4478, Revised July 26, 2005.

42. D. Uriot, Tracewin, DSM/Irfu/SACM/LEDA, CEA Saclay

43. T. P. Wangler, Principles of RF Linear Accelerators, John Wiley & Sons, INC, 1998, Page 279-281.

44. Y.S. Cho, B.H. Choi, Design of the 20 MeV DTL for KOMAC Test Facility, PAC (2001), Chicago.

45. Y. S. Cho, B. H. Choi, J. H. Jang, H. J. Kwon, M.Y. Park, Design of the 20 MeV DTL for PEFP, Proc. PAC (2003).

46. J. H. Billen, L. M. Young, S. Kurennoy, K. R. Crandall, Room temperature linac structures for the spallation neutron source, PAC (2001), Chicago.

47. R S Mills, K R Crandall and J A Farrell, Designing Self-Matching Linacs, Proc. 1984 Linac Conference.

48. Vikas Teotia, Sanjay Malhotra, Kumud Singh, U.Mahapatra, S.Bhattacharya, G.P.Srivastava, Shweta Roy, Piyush Jain, P. Singh and S. Kailas, Focussing Magnets for Drift Tube Linacs, Ind. Particle Accelerator Conf. (InPAC-2011), 15-18 February, 2011, IUAC, New Delhi.

49. Jose V. Mathew, S.V.L.S. Rao, S. Krishnagopal and P.Singh, An improved permanent magnet quadrupole design with larger good field region for high intensity proton linacs, 727, 12 (2013).

50. Steven M. Lund, John J. Barnard, Boris Bukh, Sugreev R. Chawla, Sven H. Chilton, A core-particle model for periodically focused ion beams with intense space-charge, Nuclear Instruments and Methods in Physics Research 577 (2007) 173.

51. Martin Reiser, Theory and Design of Charged Particle Beams, Wiley Series in Beam Physics and Accelerator Technology, Page 380.

52. Steven M. Lund, David P. Grote, Ronald C. Davidson, Simulations of beam emittance growth from the collective relaxation of space-charge nonuniformities, Nuclear Instruments and Methods in Physics Research A 544 (2005) 472.

53. L. R. Prost, P. A. Seidl, F. M. Bieniosek, C. M. Celata, A. Faltens, D. Baca, E. Henestroza, J. W. Kwan, M. Leitner, W. L. Waldron, R. Cohen, A. Friedman, D. Grote, S. M. Lund, A. W. Molvik, and E. Morse, High current transport experiment for heavy ion inertial fusion, Phys. Rev. ST Accel. Beams 8, 020101 (2005).

54. I. Hofmann and O. Boine-Frankenheim, Resonant Emittance Transfer Driven by Space Charge, Physical Review Letters, 87, 034802-1, (2001).

55. L. Groening, et al., Experimental Evidence of Space Charge Driven Emittance Coupling in High Intensity Linear Accelerators, Phys. Rev. Lett. 103, 224801(2009).

56. T. P. Wangler, Principles of RF Linear Accelerators, John Wiley & Sons, INC, 1998, Page 285-289.

57. Robert A. Hardekopf, Beam loss and activation at LANSCE and SNS, 7th ICFA Mini-Workshop on High Intensity, High brightness Beams, Sept 1999.

58. A.V. Fedotov and R.L. Gluckstern, Coulomb scattering within a spherical beam bunch in high current linear accelerator, Proc. Particle Accelerator Conf., New York, USA, (1999).

59. I. Hofmann, Stability of anisotropic beams with space charge, Phys. Rev. E **57** (1998) 4713.

60. T.P. Wangler, R.W. Garnet, E.R. Gray, R.D. Ryne, and T.S. Wang, Dynamics of beam halos in mismatched beams, Linac Conf. (1996).

61. F.J. Sacherer, R.m.s. envelope equations with space charge, CERN/SI/Int. DL/70-12, IEEE Trans. Nucl. Sci. NS-**18**, (1971), 1105.

62. I. Kapchinskyi and V. Vladimirskiy, Limitations of proton beam current in a strong focusing linear accelerator associated with beam space charge, Proc. 2nd Conf. High Energy Accel., CERN, Geneva, (1959).

63. T. P. Wangler, K. R. Crandall, R. Ryne, and T. S. Wang, Particle-core model for transverse dynamics of beam halo, Phys. Rev. Special Topics – Accelerators and Beams, 1 (1998) 084201.

64. Frank Gerigk, Space Charge and Beam Halos in Proton Linacs, Joint US - CERN - JAPAN – RUSSIA Particle Accelerator School Longbeach, California, November 6 - 14, 2002.

65. T.P. Wangler and K.R. Crandall, Beam halo in Proton Linac Beams, XX International Linac Conference, Monterey, California

66. C.K. Allen and T.P. Wangler, Beam halo definitions based upon moments of the particle distribution, Phys. Rev. Special Topics-Accelerators and Beams, 5 (2002) 124202.

67. P. A. P. Nghiem, N. Chauvin, W. Simeoni Jr. , D. Uriot, Beam halo definitions and its consequences, Proceedings of HB2012, Beijing, China.

68. Frequency analysis and field-stabilization for the LEHIPA DTL prototype, Shweta Roy, S.C.L. Srivastava, Rajni Pande, V.L.S. Rao Sista, S. Krishnagopal and P. Singh, Ind. Particle Accelerator Conf. (InPAC-2009), 10-14 February, 2009, RRCAT, Indore.

69. Fabrication of a Physics prototype DTL and Laser welding trials for Copper Drift tubes, Piyush Jain, Shweta Roy, S. Krishnagopal, N.K. Prasad, P.K. Nema, P.Singh, Ind. Particle Accelerator Conf. (InPAC-2011), 15-18 February, 2011, IUAC, New Delhi.

70. Klein H., CERN Accelerator School on RF Engineering of Particle Accelerators, CERN 92-03, Vol. 1, 1992, p. 112-118.

72. David M Pozar, Microwave Engineering, 2nd Edition, John Wiley and Sons.

73. L. Boltzmann, Vorlesungen uber Mechanik II, J.A. Barth, Leipzig (1903) p. 48.

74. P. Ehrenfest, Ann. Phys. 36 (1911) 91.

75. RF Characterization of DTL Prototype, Shweta Roy, S V L S Rao, Rajni Pande, Piyush Jain, Sumit Garg, Gireesh Singh, S. Krishnagopal and P. Singh, Ind. Particle Accelerator Conf. (InPAC-2011), 15-18 February, 2011, IUAC, New Delhi.

76. M. Y. Park, Y. S. Cho, H. S. Kim, H. J. Kwon, K. T. Seol, Y. G. Song, Tuning of 20 MeV PEFP DTL, Proc. PAC, 2005, Knoxville, Tennessee.

77. Frank Gerigk, Beam halo in high-intensity hadron accelerators caused by statistical gradient errors, Phys. Rev. ST Accel. Beams 7, (2004) 064202.

78. F. Gerigk, High Current Linac design with examples of resonances and halo, Proc. Linac 2002, Gyeongju, Korea.